Multidimensional modeling of the thermal and flow regime in the western part of the Molasse Basin, Southern Germany

Von der Fakultät für Georessourcen und Materialtechnik
der Rheinisch-Westfälischen Technischen Hochschule Aachen

zur Erlangung des akademischen Grades eines
Doktors der Naturwissenschaften

genehmigte Dissertation

vorgelegt von **Dipl.-Geol.**

Wolfram Rühaak

aus Berleburg

Berichter: Univ.-Prof. Dr.rer.nat. Christoph Clauser
Professor Dr. Hans-Joachim Kümpel

Tag der mündlichen Prüfung: 23. Januar 2009

I have identified three phases of development in modeling – the illusion, the chaos, and the relief – through which models seem to evolve before their results can be said to approach the truth with some confidence.

Corinne le Quéré, University of East Anglia and the British Antarctic Survey, Norwich, U.K.

The Unknown and the Uncertain in Earth System Modeling, in Eos, Vol. 87, No. 45, 7 November 2006

Abstract

The aim of this thesis is to obtain information on the groundwater flow regime at great depth within the Molasse Basin (SW Germany).

For this purpose different numerical codes are applied. For an optimal geometrical representation of the basin geometry it was necessary to develop a coordinate transformation method. This work is presented in the first part of the thesis. Many popular groundwater modeling codes are based on the finite differences or finite volume method for orthogonal grids. In cases of complex subsurface geometries this type of grid either leads to coarse geometric representations or to extremely fine meshes. Therefore, a coordinate transformation method has been developed to circumvent this shortcoming. In computational fluid dynamics (CFD), this method has been applied successfully to the general Navier-Stokes equation. The method is based on tensor analysis and performs a transformation of a curvilinear into a rectangular unit grid, on which a modified formulation of the differential equations is applied. Due to this it is not necessary to reformulate existing simulation code in total. The coordinate transformation method was applied to the three-dimensional code SHEMAT, a simulator for flow and heat transport in porous media. The finite volume discretization scheme for the non-orthogonal, structured, hexahedral grid yields a 19-point stencil and a correspondingly banded system matrix. The implementation is straightforward and it is possible to use many existing routines without modification. The accuracy of the modified code is demonstrated for single-phase flow on a two-dimensional analytical solution for flow and heat transport and further on a thermal free-convection benchmark. Additionally, a simple two-dimensional case of potential flow is shown for a grid which is increasingly deformed. The result reveals that the error increases only slightly.

In the second part the actual basin analysis is shown and discussed. Data relevant for a flow model at depth between 600 m to 1600 m below the surface are generally sparse in the western part of the Molasse Basin. However, a relatively large set of temperature measurements is available covering a large part of the area at a wide range of depths. Therefore, a thermal 3-D quasi steady-state model was set up with the aim of comparing modeled with measured subsurface temperatures. Additional to the temperature data, some values of rock thermal conductivity and heat production rate are available. Other data are too sparsely distributed to be useful. The purely conductive model reveals some strong thermal anomalies, especially along fault zones, and within stratigraphic layers with high hydraulic conductivity. While temperature in the upper crust is dominated by conductive heat transport, heat advection associated with groundwater flow may significantly alter the purely con-

ductive regime. The thermal anomalies can be explained by various advective heat transport mechanisms - yet most of them can be eliminated: The only constellation explaining the major positive thermal anomalies of 10 K and more is a fault zone intersected by an aquifer with flow parallel to the fault zone. This was validated by using a simplified type model. In spite of some shortcomings, the method presented here can be used to identify temperature anomalies, and in a second step, to identify possible explanations.

Parts of this work have been published in the following two papers:

1. W. Rühaak (2006): A Java application for quality weighted 3-d interpolation, Computers & Geosciences 32,1: 43-51 (doi: 10.1016/j.cageo.2005.04.005).
2. W. Rühaak, V. Rath, A. Wolf & C. Clauser (2008): 3D finite volume groundwater and heat transport modeling with non-orthogonal grids using a coordinate transformation method, Advances in Water Resources 31,3: 513-524 (doi: 10.1016/j.advwatres.2007.11.002).

Zusammenfassung

Ziel dieser Arbeit ist die Gewinnung von Informationen über das Grundwasserregime in großen Tiefen innerhalb des südwestdeutschen Molassebeckens.

Hierzu wurden verschiedene numerische Programme eingesetzt. Da eine optimale geometrische Darstellung der Beckengeometrie von großer Bedeutung sein kann, wurde ein Koordinaten-Transformations-Verfahren entwickelt. Diese Arbeit wird in dem ersten Teil dieses Textes präsentiert.

Viele gängige Grundwassermodellierungs-Programme basieren auf der Finite-Differenzen- bzw. Finite-Volumen-Methode. Diese numerischen Verfahren setzen im Allgemeinen orthogonale Gitter voraus. Im Fall von komplexen Geometrien des Untergrundes führen diese Gitter entweder zu einer groben Repräsentation oder zu einer extrem großen Anzahl von Gitterknoten. Die Koordinatentransformations-Methode wurde entwickelt, um diese Einschränkung zu überwinden. Im Bereich der Strömungsmechanik (Computational Fluid Dynamics - CFD) wird diese Methode bereits seit langem erfolgreich für freie (Navier-Stokes) Strömung eingesetzt. Sie basiert auf der Tensor-Analysis, zur Transformation des schiefen Gitters auf ein rechtwinkliges Einheitsgitter. Auf diesem transformierten Gitter können dann mit Hilfe von Transformationstermen die üblichen Differentialgleichungen berechnet werden. Dadurch ist es nicht nötig, bestehenden Programmcode vollständig neu zu schreiben. Das Koordinatentransformations-Verfahren wurde in das 3D-Programm SHEMAT zur Berechnung von Strömung und Wärmetransport in porösen Medien integriert. Das Finite-Volumen-Diskretisierungsschema für ein nicht-orthogonales strukturiertes Hexaeder-Gitter ergibt einen 19-Punkt-Differenzenstern und ein entsprechendes Matrix-Vektor-Produkt. Die Implementierung ist verhältnismäßig einfach, eine Vielzahl von Programmroutinen können ohne Modifikation weiterverwendet werden. Die Genauigkeit des modifizierten Programms wird für Einphasen-Strömung bei verschiedenen 2D-Verifikationsrechnungen und 2D- bzw. 3D-Benchmarks demonstriert. Unter anderem wird eine 2D-Lösung für erzwungenen Wärmetransport auf einem schiefen Gitter gezeigt. Weiterhin wird ein Problem mit freier thermischer Konvektion zu Vergleichszwecken einmal auf einem schiefwinkligen und einmal auf einem orthogonalen Gitter berechnet. Zusätzlich wird für ein einfaches 2D-Potentialfeldproblem gezeigt, dass der Fehler bei zunehmender Gitterschiefe nur geringfügig zunimmt.

Im zweiten Teil der Arbeit wird das Strömungsregime im westlichen Molassebecken analysiert, wobei der Schwerpunkt auf dem mit der Strömung assoziierten Wärmetransport liegt. Daten für ein Strömungsmodell in Tiefen von 600 m bis 1600 m unterhalb

der Oberfläche sind hier, ebenso wie in anderen Bereichen Deutschlands, kaum vorhanden. Es existiert jedoch eine Vielzahl von Temperaturmessungen, die weite Bereiche abdecken und auch für größere Tiefen vorliegen. Daher wurde ein quasi-stationäres konduktives 3D-Modell aufgebaut, mit dem Ziel, modellierte Temperaturen mit gemessenen zu vergleichen. Zusätzlich zu den Temperaturmessungen liegen einige Messwerte der Wärmeleitfähigkeit und der Wärmeproduktion der anstehenden Gesteine vor. Andere Daten sind in zu geringem Umfang vorhanden, um sinnvoll einbezogen werden zu können. Das rein konduktive Modell zeigt einige Bereiche mit starken thermischen Anomalien, insbesondere in der Nähe von Störungszonen und innerhalb von Schichten mit großer Permeabilität.

Die Temperaturverteilung in der oberen Erdkruste wird dominiert durch konduktiven Wärmetransport. Advektiver Wärmetransport kann dieses konduktive Temperaturfeld jedoch stark verändern. Die festgestellten thermischen Anomalien können über verschiedene advektive Prozesse erklärt werden, wobei die meisten Erklärungen aber nach näherer Untersuchung ausgeschlossen werden können. Die einzige Erklärung für die nachgewiesenen Temperaturanomalien von 10 K und mehr basiert auf der Anordnung der Störungszonen zum Strömungsfeld: die Störungen werden von verschiedenen Grundwasserleitern parallel durchströmt. Dass diese Anordnung die Temperaturanomalien erklären kann, wird mit einem Prinzipmodell nachgewiesen.

Trotz der eingeschränkten Aussagekraft der vorgestellten Analysen ist die hier vorgestellte Methode ein geeigneter Weg, um Temperaturanomalien nachzuweisen und um in einem zweiten Schritt mögliche Gründe zu identifizieren.

Contents

1 Introduction

The aim of this thesis is to discriminate between areas with high flow rates and low flow rates of groundwater at depths of 600 m to 1600 m below the surface. The study area is the Molasse Basin in southern Germany: a sedimentary basin located north of the Alps (Fig. 1). In order to obtain the desired results, methods were applied and developed for the numerical modeling of flow and heat transport.

The first part of this thesis presents the modification of an existing code (*Rühaak et al.*, 2008). Many codes are available for the modeling of fluid flow and heat transport. A recent overview is given by *Anderson* (2005). The program SHEMAT (*Clauser*, 2003) is a well known code, often used for the modeling of deep groundwater and heat transport in sedimentary rocks. This program uses a finite volume method (FVM) on an orthogonal grid. Geometrically complex three-dimensional flow domains often cannot be represented well by a rectangular spatial discretization because the geometry is approximated by steps. Therefore, a more flexible, non-orthogonal discretization was implemented into this well-tested program, preserving as much of the original code's structure as possible. Only that part of the code which deals directly with the set-up of the system of equations had to be modified.

Typically, arbitrary grids are used in codes based on the finite element method (FEM). Here, the aim is to improve an existing finite volume code. The resulting code (called 'sno') is programmed in Fortran, uses structured, hexahedral grids and is designed in a modular way optimized for parallel computing (OpenMP). A graphical user interface is also available to assist in setting up input files. The computed numerical results can be stored in different formats for visualization (among others for *Tecplot*® and *VTK*®).

In the second part of this thesis the modeling of the thermal regime in the Molasse Basin is presented and discussed. Generally, data covering the specified depth range over a large area are sparse. The only relevant data set with good spatial coverage are borehole temperatures (see Fig. 1). They derive mainly from oil exploration and some geothermal studies.

Advective heat transport by groundwater flow may modify significantly the temperature field in the upper crust (e.g. *Vasseur et al.*, 1995). This fact is exploited in this investigation and has been used before in several other studies. The Alberta Basin and plains (Canada) was studied by *Tóth* (1962), who promoted the importance of topographically driven groundwater flow in this case study. Later, *Majorowicz and Jessop* (1981), *Majorowicz et al.* (1999), and *Bachu* (1999) focused their studies on the interaction between temperature and groundwater flow, whereas *Bekele et al.* (2000) emphasized the significance of anomalous pressures on the transport of hydrocarbons and heat. The north-American Great Plains were studied, for instance, by *Bethke* (1986) and *Garven et al.* (1993) with an emphasis on the formation of hydrothermal deposits, whereas *Gosnold* (1999) gives a general review of anomalous specific heat flow, due to advective heat transport. The northeastern German Basin was studied by *Bayer et al.* (1997), *Ondrak et al.* (1998), *Bayer et al.* (1999), and *Vosteen et al.* (2004) who calculated different numerical foreward and inverse conductive models and compared the results with measured temperatures. *Schmidt Mumm and Wolfgramm* (2004) studied the same basin with respect to hydrothermal deposits. The Great Artesian Basin (Australia) was studied by, for instance, *Polak and Horsfall* (1979), *Cull and Conley* (1983), and *Pitt* (1986) regarding the specific heat flow distribution. Later, *Bethke et al.* (1999) studied the groundwater flow based on Helium isotopes, whereas *Pestov* (2000) emphasized the role of natural convection. In addition to these basins, the flow and temperature distribution in graben structures has also been investigated. For instance, the Rhine Graben was studied by *Clauser and Villinger* (1990); *Person and Garven* (1992); *Clauser* (1999); *Pribnow and Schellschmidt* (2000); *Bächler et al.* (2003). General reviews of the heat distribution within the crust are given by *Beardsmore and Cull* (2001); *Allen and Allen* (1990); *Förster and Merriam* (1999b). While this list is by no means complete it provides examples for the different types of basin analyses.

1.1 Outline of this thesis

This thesis is organized as follows: Chapter 2 presents the basic equations for flow in porous media and the resulting system of partial differential equations describing flow and heat transport in porous media. In order to solve this system of equations a numerical method has been developed based on a coordinate transformed finite volume method and the accuracy of this method is discussed. In the Chapter 3, the thermal and flow regime in the western part of the Molasse Basin is studied. To this end the setup of a conductive thermal model is presented and the resulting temperatures are compared with measured temperature data. The identified strong thermal anomalies are examined, whereas the discussion of the flow regime is based on a strata-bound two-dimensional Péclet and Rayleigh number analysis. The study comes to the conclusion that flow within the vertical fault systems in the study area is of great importance. This motivates setting up a simplified type model to study the possible influence of the fault system on the distribution of heat.

Chapter 4 summarizes the results in a final discussion.

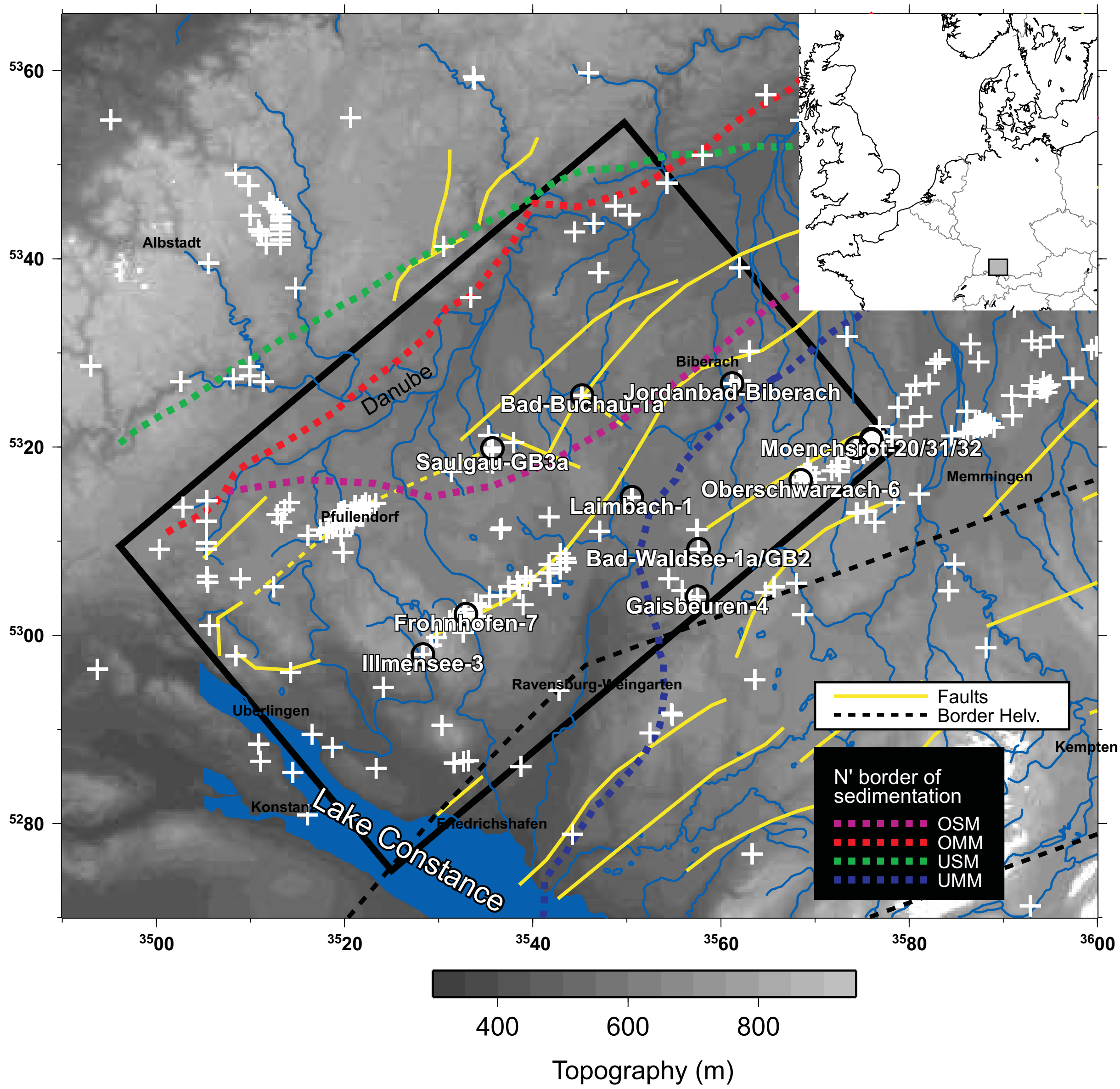

Figure 1: The study area in the Molasse Basin in southern Germany (see inset). White crosses show locations with subsurface temperature measurements. Locations with continuous logs are marked by a circle and large location names. The black rectangle shows the position of the conductive model. Coordinates are given in the Gauss-Krüger system. Rivers and Lake Constance are marked in blue. Yellow lines show presumed locations of faults. The dashed black line shows the northern border of the Helvetic facies. The other colored dashed lines mark the northern sedimentation borders of the major Tertiary units (see text for explanation of the abbreviations).

2 3D finite volume groundwater and heat transport modeling with non-orthogonal grids, using a coordinate transformation method

Different approaches are available for computing fluid flow with the finite volume method (FVM) or finite differences method (FDM) on non-orthogonal grids (see e.g. *Vinokur*, 1989; *Anderson*, 1995; *Frolkovic*, 1996; *Lee and Soni*, 1998; *Edwards*, 2000; *Fletcher*, 2000b). The Integrated Finite Differences Method (IFDM) approach by *Narasimhan and Witherspoon* (1976) may possibly be the earliest approach to use a FVM on non-orthogonal grids in groundwater modeling. It is easy to apply but has the disadvantage of requiring that the cell-faces be perpendicular to the connections between the cell-midpoints. Further, the cell-faces should be located approximately in the middle between the adjacent cells. These are significant restrictions for the structure of the grid, in particular with respect to the mapping of complex geologic structures onto a grid.

In general, two types of curvilinear grids are distinguished in CFD: those based on curvilinear orthogonal coordinates and those based on general curvilinear coordinates. The first type assumes that the grid lines intersect at right angles. *Demirdžić* (1982) and *Perić* (1985) developed a code for the general curvilinear approach, using a tensorial coordinate transformation. *Jin* (2001) used this approach to modify an existing finite differences code for modeling of (Navier-Stokes) flow within a nuclear reactor. Until now, this method has not been used for the calculation of flow and heat transport in porous media. But is most appropriate for this purpose. This will be demonstrated in the following.

Lately, *Loudyi et al.* (2007) have presented a code which uses also a FVM on non-orthogonal grids. In contrast to the approach presented here, they use an improved least squares gradient technique to account for the non-orthogonality. Their approach is implemented for groundwater flow in porous media on structured 2D-grids only.

2.1 Governing equations

2.1.1 Ground water flow and heat transport

Derived from mass conservation, groundwater head $h\,(m)$ in a confined aquifer can be expressed as (see e.g. *Clauser*, 2003):

$$S_s \frac{\partial h_0}{\partial t} = \sum_{k=1}^{3} \frac{\partial}{\partial y_k} \left[\mathbf{K} \left(\frac{\partial h_0}{\partial y_k} + \psi \right) \right] + W, \tag{1}$$

where $y_k\,(m)$ are the three cartesian directions (y_3 is the vertical), $t\,(s)$ denotes time, and $W\,(m^3\,s^{-1})$ is a source term. The hydraulic conductivity tensor $\mathbf{K}\,(ms^{-1})$ is :

$$\mathbf{K} = \frac{\mathbf{k}\rho_f g}{\mu_f}. \tag{2}$$

Here, $\mu_f\,(Pa\,s)$ denotes the dynamic fluid viscosity, $\rho_f\,(kg\,m^{-3})$ fluid density, $\mathbf{k}\,(m^2)$ the permeability tensor, and $g\,(m\,s^{-2})$ gravity.

The specific storage coefficient $S_s\,(m^{-1})$ is computed from fluid density ρ_f, fluid compressibility $\gamma\,(Pa^{-1})$, porosity $\phi\,(-)$, and from rock compressibility $\alpha\,(Pa^{-1})$:

$$S_s = \rho_f g(\alpha + \phi\gamma(T, P)) \tag{3}$$

Buoyancy is accounted for by

$$\psi = \rho_r \nabla y_3, \tag{4}$$

the relative density ρ_r is defined as:

$$\rho_r = \frac{\rho_f - \rho_0}{\rho_0}, \tag{5}$$

where ρ_0 is the density at reference conditions, and ρ_f the fluid density resulting from the actual pressure, temperature, and salinity.

The hydraulic constant density potential (head) $h_0\,(m)$ at reference conditions is given by

$$h_0 = y_3 + \frac{P}{\rho_0 g}, \tag{6}$$

where $P\,(MPa)$ is pressure.

The heat transport equation in Cartesian coordinates follows from energy conservation (see e.g. *Clauser*, 2003):

$$\rho_g c_g \frac{\partial T}{\partial t} = \sum_{k=1}^{3} \left[\frac{\partial}{\partial y_k} \left(\lambda_{\mathbf{g}} \frac{\partial T}{\partial y_k} - \rho_f c_f T \mathbf{v} \right) \right] + H. \tag{7}$$

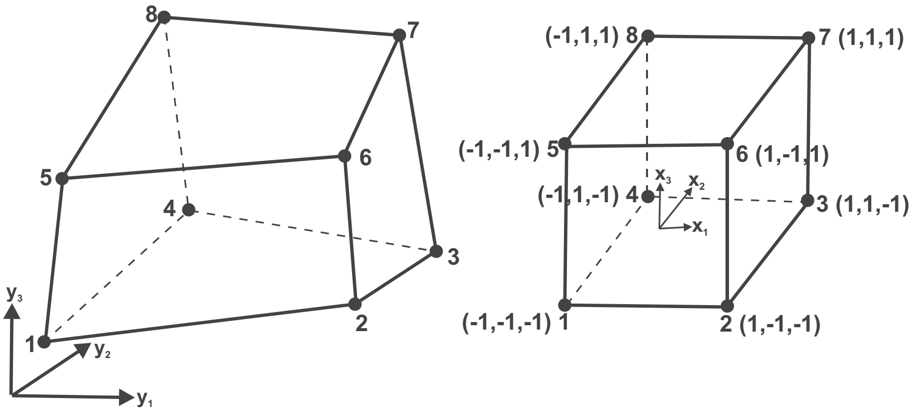

Figure 2: Principle of the coordinate transformation approach. An arbitrarily shaped hexahedron is transformed into a unit cube. Modified from *Yeh* (1999).

$T\,(^\circ C)$ denotes temperature, $\lambda_{\mathbf{g}}\,(W\,m^{-1}\,K^{-1})$ the bulk thermal conductivity tensor and $c\,(J\,kg^{-1}\,K^{-1})$ specific heat capacity. $H\,(W\,m^{-3})$ summarizes the heat sources such as constant basal heat flow at the lower boundary, rock heat production rate, and global fluid heat production rate. Bulk rock (subscript g) and fluid contributions (subscript f) are weighted linearly with porosity ϕ to the volumetric thermal capacity $\rho_g c_g$.

Porosity as well as the other material properties are treated as constant in time.

Specific discharge $\mathbf{v}\,(m\,s^{-1})$ (per unit area of cross section), also referred to as Darcy velocity, is defined by the Darcy equation:

$$\mathbf{v} = -\mathbf{K}(\nabla h + \psi), \tag{8}$$

2.1.2 The coordinate transformation approach

The coordinate transformation approach is based on tensor analysis and performs a transformation of a curvilinear into a rectangular unit grid (Fig. 2).

Introducing a new set of structure-aligned curvilinear coordinates, say x_i, the transformation $x_i = f(y)$ transforms the Cartesian coordinates to the new system. It is characterized by the Jacobian $\mathbf{J}$ of partial derivatives:

$$\mathbf{J} = \begin{bmatrix} \frac{\partial x_1}{\partial y_1} & \frac{\partial x_1}{\partial y_2} & \frac{\partial x_1}{\partial y_3} \\ \frac{\partial x_2}{\partial y_1} & \frac{\partial x_2}{\partial y_2} & \frac{\partial x_2}{\partial y_3} \\ \frac{\partial x_3}{\partial y_1} & \frac{\partial x_3}{\partial y_2} & \frac{\partial x_3}{\partial y_3} \end{bmatrix}, \tag{9}$$

and its determinant

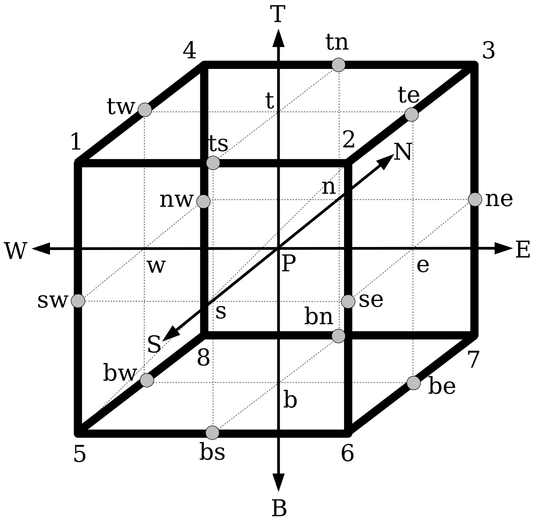

Figure 3: Control volume P, definition of the direction names and numbering.

$$J = \begin{vmatrix} \frac{\partial x_1}{\partial y_1} & \frac{\partial x_1}{\partial y_2} & \frac{\partial x_1}{\partial y_3} \\ \frac{\partial x_2}{\partial y_1} & \frac{\partial x_2}{\partial y_2} & \frac{\partial x_2}{\partial y_3} \\ \frac{\partial x_3}{\partial y_1} & \frac{\partial x_3}{\partial y_2} & \frac{\partial x_3}{\partial y_3} \end{vmatrix} . \tag{10}$$

With this, the transformed second derivative of a variable θ is (*Perić*, 1985):

$$\frac{\partial}{\partial y_i}\left(\frac{\partial \theta}{\partial y_i}\right) = \frac{1}{J}\sum_{j=1}^{3}\left\{\frac{\partial}{\partial x_j}\left[\frac{1}{J}\sum_{k=1}^{3}\left(\frac{\partial \theta}{\partial x_k}\beta_i^k\right)\right]\beta_i^j\right\}, \tag{11}$$

with

$$\frac{\partial x_j}{\partial y_i} = \frac{1}{J}\beta_i^j \text{ , and } \beta_1^1 = \frac{\partial \mathrm{y}_2}{\partial \mathrm{x}_2}\frac{\partial \mathrm{y}_3}{\partial \mathrm{x}_3} - \frac{\partial \mathrm{y}_2}{\partial \mathrm{x}_3}\frac{\partial \mathrm{y}_3}{\partial \mathrm{x}_2} \text{ , etc.} \tag{12}$$

For a more complete definition please see Appendix A.1.

2.2 Numerical procedure

2.2.1 Transformation of the basic equations

According to Eq. 11, the transformed equation for the groundwater head (Eq. 1) can be written as:

$$JS_s \frac{\partial h}{\partial t} = \sum_{j=1}^{3} \left\{ \frac{\partial}{\partial x_j} \left[\mathbf{K} \frac{1}{J} \sum_{k=1}^{3} \left(\frac{\partial h}{\partial x_k} B_j^k \right) \right] + \mathbf{K} \psi \beta_i^j \right\} + JW \tag{13}$$

With:

$$B_j^k = \beta_i^j \beta_i^k \text{ for } i = 1,2,3; j = 1,2,3; k = 1,2,3. \tag{14}$$

From integrating Eq. 13 over the control volume V$_P$ (see Fig. 3)

$$\int\limits_{V_P} JS_s \frac{\partial h}{\partial t} dV = \int\limits_{V_P} \sum_{j=1}^{3} \left\{ \frac{\partial}{\partial x_j} \left[\mathbf{K} \frac{1}{J} \sum_{k=1}^{3} \left(\frac{\partial h}{\partial x_k} B_j^k \right) \right] + \mathbf{K} \psi \beta_i^j \right\} dV + \int\limits_{V_P} JW dV \tag{15}$$

and applying the Gauss divergence theorem results in a typical finite volume formulation where A is the control volume's surface:

$$
\begin{aligned}
&\int\limits_{V_P} S_s \frac{\partial h}{\partial t} dV = \\
&\int\limits_{A_e} \left[\frac{\mathbf{K_e}}{J} \sum_{k=1}^{3} \left(\frac{\partial h}{\partial x_k} B_1^k \right) \right] dx_2 dx_3 - \\
&\int\limits_{A_w} \left[\frac{\mathbf{K_w}}{J} \sum_{k=1}^{3} \left(\frac{\partial h}{\partial x_k} B_1^k \right) \right] dx_2 dx_3 + \\
&\int\limits_{A_n} \left[\frac{\mathbf{K_n}}{J} \sum_{k=1}^{3} \left(\frac{\partial h}{\partial x_k} B_2^k \right) \right] dx_1 dx_3 - \\
&\int\limits_{A_s} \left[\frac{\mathbf{K_s}}{J} \sum_{k=1}^{3} \left(\frac{\partial h}{\partial x_k} B_2^k \right) \right] dx_1 dx_3 + \\
&\int\limits_{A_t} \left[\frac{\mathbf{K_t}}{J} \sum_{k=1}^{3} \left(\frac{\partial h}{\partial x_k} B_3^k + \psi \beta_3^k \right) \right] dx_1 dx_2 - \\
&\int\limits_{A_b} \left[\frac{\mathbf{K_b}}{J} \sum_{k=1}^{3} \left(\frac{\partial h}{\partial x_k} B_3^k + \psi \beta_3^k \right) \right] dx_1 dx_2 + \\
&\int\limits_{V_P} JW dV
\end{aligned}
\tag{16}
$$

Here the subscripts w,e,n,s are related to the geographical directions, b means bottom and t means top (see Fig. 3 and Fig. 4).

As buoyancy, after transformation onto the unity grid, is only relevant in the direction of gravity, it is only added to the top and bottom terms.

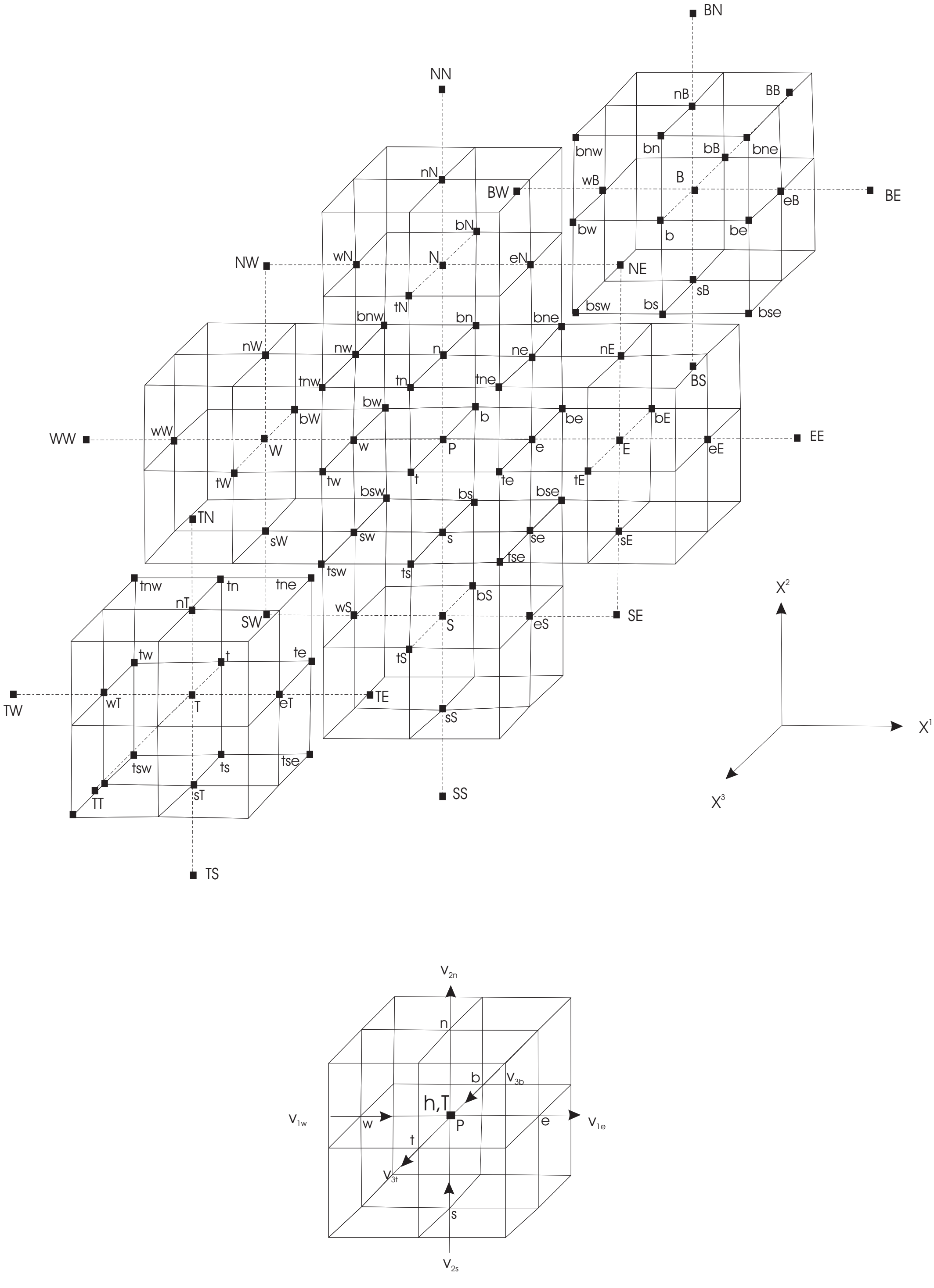

Figure 4: Mesh assignment (top) and arrangement of variables (bottom) within the transformed space (modified from *Jin*, 2001).

A differential volume in physical space is defined as:

$$dV = J dx_1 dx_2 dx_3. \tag{17}$$

Therefore the volume of a central mesh can be approximated by:

$$V_P \approx J \Delta x_1^P \Delta x_2^P \Delta x_3^P, \tag{18}$$

here Δx denotes the transformed mesh spacing, which is usually set to unity. P designates the center of the primary volume.

Thus the discretised equation for the surface area e can be written as:

$$\int\limits_{A_e} \left[\frac{\mathbf{K}}{J} \left(\frac{\partial h}{\partial x_k} B_1^1 + \frac{\partial h}{\partial x_k} B_1^2 + \frac{\partial h}{\partial x_k} B_1^3 \right) dx_2 dx_3 \right]_e = \\ \left(\frac{\mathbf{K}}{V} \right)_e D_{1e}^1 (h_E - h_P) + \left(\frac{\mathbf{K}}{V} \right)_e \left[(D_2^1 (h_n - h_s) + D_3^1 (h_t - h_b) \right]_e, \tag{19}$$

where the first term represents the normal- and the second one the cross-derivative contribution respectively.

The uppercase E indicates the cell-center of the neighboring volume to the east and the lowercase e denotes the center of the cell face area, and accordingly for all other directions. The term $\left(\frac{\mathbf{K}}{V}\right)_e$ denotes values for a shifted volume between the center P and E. It is given by the volume around point e, which is defined by the points bs, ts, tn, bn of control volumes P and E, respectively (compare Fig. 3).

D_j^i are geometric coefficients determined (in analogy to Eq. 14) as:

$$\begin{aligned} D_1^1 &= b_1^1 b_1^1 + b_2^1 b_2^1 + b_3^1 b_3^1 \\ D_1^2 &= b_1^2 b_1^1 + b_2^2 b_2^1 + b_3^2 b_3^1 \\ D_1^3 &= b_1^3 b_1^1 + b_2^3 b_2^1 + b_3^3 b_3^1 \\ &etc., \end{aligned}$$

with:

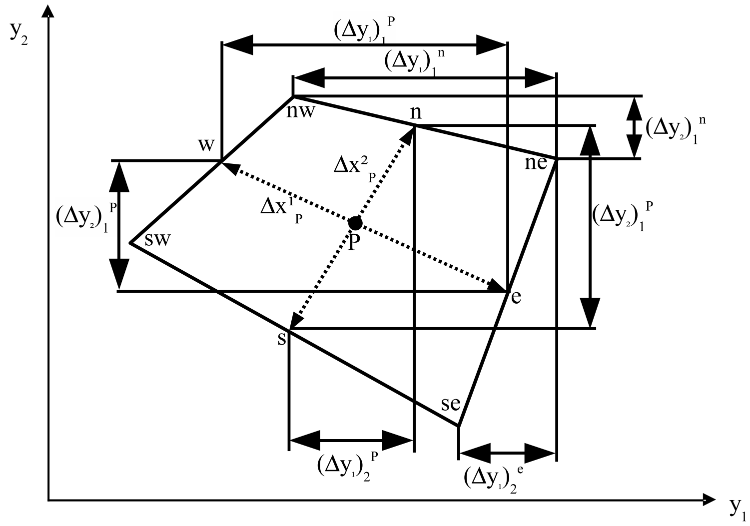

Figure 5: Two-dimensional representation of some basic geometrical quantities modified after *Perić* (1985) and *Schönung* (1990)
.

$$\begin{aligned} b_1^1 &\approx (\Delta y_2)_2(\Delta y_3)_3 - (\Delta y_2)_3(\Delta y_3)_2 \\ b_1^2 &\approx (\Delta y_1)_3(\Delta y_3)_2 - (\Delta y_1)_2(\Delta y_3)_3 \\ b_1^3 &\approx (\Delta y_1)_2(\Delta y_2)_3 - (\Delta y_1)_3(\Delta y_2)_2 \\ etc., & \end{aligned} \tag{20}$$

and

$$\beta_i^j = \frac{1}{\Delta x_i \Delta x_j} b_i^j. \tag{21}$$

The b_i^j represent the cofactor of $\partial y_i/\partial x_j$ in the Jacobian of the coordinate transformation $y_i = y_i(x_j)$ (*Perić*, 1985).

$(\Delta \mathrm{y}_i)_j^m$ are the increments in cartesian coordinates y_i along arbitrary coordinates x_j at one of the surfaces, here denoted with m.

These variables are shown for the simpler two-dimensional case in Fig. 5.

Thus the following terms occur, for instance, on the eastern face of a control volume (*Jin*, 2001):

$$
\begin{aligned}
(\Delta y_1)_1 &= y_1^E - y_1^P \\
(\Delta y_1)_2 &= y_1^{ne} - y_1^{se} \\
(\Delta y_1)_3 &= y_1^{te} - y_1^{be} \\
(\Delta y_2)_1 &= y_2^E - y_2^P \\
(\Delta y_2)_2 &= y_2^{ne} - y_2^{se} \\
(\Delta y_2)_3 &= y_2^{te} - y_2^{be} \\
(\Delta y_3)_1 &= y_3^E - y_3^P \\
(\Delta y_3)_2 &= y_3^{ne} - y_3^{se} \\
(\Delta y_3)_3 &= y_3^{te} - y_3^{be}
\end{aligned}
$$

The meaning of indices like ne is illustrated in Fig. 3 and Fig. 4.

To calculate the volume and center of the control-volume hexahedra, a method suggested by *Vinokur* (1989) is used: First, an artificial center of the hexahedra is defined. Around this center 12 tetrahedra are constructed by connecting the center with the vertices. Now for each of these tetrahedra a volume and a center of gravity can be calculated, which represents the hexahedra (for details see *Bowyer and Woodwark*, 1983).

With an adequate differencing scheme the full equation can be translated into a system of linear equations with one equation for each control volume. This yields:

$$
\begin{aligned}
&V_P S_s \frac{h_P^{t+1} - h_P^t}{\delta t} = \\
&\left\{ \left(\frac{\mathbf{K}}{V}\right)_e \left(D_{1e}^1 (h_E - h_P) - \left[D_{1e}^2 (h_{ne} - h_{se}) + D_{1e}^3 (h_{te} - h_{be})\right]\right) \right\} - \\
&\left\{ \left(\frac{\mathbf{K}}{V}\right)_w \left(D_{1w}^1 (h_W - h_P) - \left[D_{1w}^2 (h_{nw} - h_{sw}) + D_{1w}^3 (h_{tw} - h_{bw})\right]\right) \right\} + \\
&\left\{ \left(\frac{\mathbf{K}}{V}\right)_n \left(D_{2n}^2 (h_N - h_P) - \left[D_{2n}^1 (h_{ne} - h_{nw}) + D_{2n}^3 (h_{tn} - h_{bn})\right]\right) \right\} - \\
&\left\{ \left(\frac{\mathbf{K}}{V}\right)_s \left(D_{2s}^2 (h_S - h_P) - \left[D_{2s}^1 (h_{se} - h_{sw}) + D_{2s}^3 (h_{ts} - h_{bs})\right]\right) \right\} + \\
&\left\{ \left(\frac{\mathbf{K}}{V}\right)_t \left(D_{3t}^3 (h_T - h_P) - \left[D_{3t}^1 (h_{te} - h_{tw}) + D_{3t}^2 (h_{tn} - h_{ts})\right] + \psi_t\right) \right\} - \\
&\left\{ \left(\frac{\mathbf{K}}{V}\right)_b \left(D_{3b}^3 (h_B - h_P) - \left[D_{3b}^1 (h_{be} - h_{bw}) + D_{3b}^2 (h_{bn} - h_{bs})\right] + \psi_b\right) \right\} + \\
&V_P W
\end{aligned}
\tag{22}
$$

The buoyancy term ψ is transformed similarly. Additional cross-derivatives are calculated similar to Eq. 22 to compensate the skewness of the control volume. The terms are additionally weighted by a volume-ratio, which is given by the ratio of a shifted volume divided by the central volume. The shifted volume is given, for instance, by the volume around point t (defined by the points sw, se, ne, nw of control volumes P and T, respectively, compare Fig. 3) Due to the coordinate transformation, buoyancy has only to be taken into account on the top and bottom faces of each control volume.

$$
\begin{aligned}
\psi_t &= \tfrac{V_t}{V_P} \quad \left(\beta_{3t}^1 \rho_{r\,t} + \beta_{3t}^2 \rho_{r\,t} + \beta_{3t}^3 \rho_{r\,t} + \beta_{3t}^1 (\rho_{r\,te} - \rho_{r\,tw}) + \beta_{3t}^2 (\rho_{r\,tn} - \rho_{r\,ts})\right) \\
\psi_b &= \tfrac{V_b}{V_P} \quad \left(\beta_{3b}^1 \rho_{r\,b} + \beta_{3b}^2 \rho_{r\,b} + \beta_{3b}^3 \rho_{r\,b} + \beta_{3b}^1 (\rho_{r\,be} - \rho_{r\,bw}) + \beta_{3b}^2 (\rho_{r\,bn} - \rho_{r\,bs})\right)
\end{aligned}
\tag{23}
$$

For instance $\rho_{r\,t}$ and $\rho_{r\,b}$ denote the relative fluid density at the top and bottom face-center respectively.

As a consequence of the approach which is used to compute buoyancy (see Eq. 4), the result can become wrong if the grid lines in the vertical direction are not parallel to the vector of gravity. This is further discussed in the section 2.3.3. The main problem is that the transformation terms are meant to be used for (Finite-Volume) balancing, like in Eq. 22. However, the Darcy equation (Eq. 8) is not used in a balancing manner here, i.e. is not integrated for the volume, instead it is simply an additional term. To overcome this shortcoming in the future, a least-squares method could be applied: based on an over-determined set of buoyancy equations for each direction it would be possible to interpolate correct values for the vertical direction. However, a more general approach would be desirable, i.e. a different ('integral') inclusion of the Darcy equation, as this would allow the application of the coordinate transformation terms.

The corresponding transformation of the heat transport equation (Eq. 7) is:

$$J\rho_g c_g \frac{\partial T}{\partial t} = \sum_{j=1}^{3} \frac{\partial}{\partial x_j} \left[\frac{1}{J} \sum_{k=1}^{3} \left(\left(\lambda_{\mathbf{g}} \frac{\partial T}{\partial x_k} - \rho_f c_f T \mathbf{v} \right) B_j^k \right) \right] + JH. \tag{24}$$

The subsequent differencing scheme is analogous to the one for the groundwater flow-equation.

For the staggered variables – defined on the cell-faces – interpolated values are needed which are calculated depending on the physical meaning either as harmonic means (as proposed by *Patankar*, 1980) or as volume averages.

For instance, the harmonic mean of the hydraulic conductivity at the top face of the control-volume is calculated as:

$$K_t = \overline{|PT|} \frac{2K_P K_T}{(\overline{|t_P b_P|} K_T) + (\overline{|t_T b_T|} K_P)} \tag{25}$$

Again subscript t (for 'top') denotes the center of the face between the current control volume (subscript P) and the control volume located above (subscript T). $\overline{|PT|}$ is the Euclidian distance from P to T (see Fig. 3, Fig. 4 and Fig. 5).

The fluid density at the same location is calculated as volumetric mean with:

$$\rho_t = \frac{\rho_P V_P + \rho_T V_T}{V_T + V_P} \tag{26}$$

V_P denotes the volume of the central control volume and V_T the volume of the control volume on top of it.

The tensor of anisotropy is assumed to be diagonal and is taken into account by a linear interpolation. For instance, the anisotropy a_e, between the central control volume (CV_P) and its eastern neighbor (CV_E) is calculated as:

$$a_e = \frac{a_1\overline{|PE|}_1 + a_2\overline{|PE|}_2 + a_3\overline{|PE|}_3}{\overline{|PE|}_1 + \overline{|PE|}_2 + \overline{|PE|}_3} \tag{27}$$

Here a_1, a_2 and a_3 are the cartesian values of the diagonal entries of the anisotropy tensor. For instance $\overline{|PE|}_1$ is the absolute value of the x-component of the vector between the center of CV_P to CV_E.

Darcy velocities are calculated staggered for the east, north and top faces of the control volume. As a structured hexahedral grid is used, it is not necessary to calculate the velocities on the opposite sides. Transformed velocities can be calculated with the introduced transformation coefficients, scaled by the corresponding volume:

$$\begin{aligned}
v_e = &\quad \frac{K_e(h_P - h_E)\beta^1_{1e} + K_n(h_P - h_N)\beta^2_{1e} + K_t(h_P - h_T)\beta^3_{1e})}{V_e} \\
v_n = &\quad \frac{K_e(h_P - h_E)\beta^1_{2e} + K_n(h_P - h_N)\beta^2_{2e} + K_t(h_P - h_T)\beta^3_{2e}}{V_n} \\
v_t = &\quad \frac{K_e(h_P - h_E)\beta^1_{3e} + K_n(h_P - h_N)\beta^2_{3e} + K_t(h_P - h_T)\beta^3_{3e}}{V_t}
\end{aligned} \tag{28}$$

A consistent velocity approximation (*Voss and Souza*, 1987) is not applied, like in the original SHEMAT.

Currently, the system is computed with a solver for a 7-point stencil. Hence the cross-derivative part of the differencing scheme (see Eq. 19) has to be solved in an explicit manner, i.e. they are evaluated at the previous iteration level, and integrated into the source-term as known quantities. If the grid is orthogonal, all the cross-derivative terms vanish. In the case of grids with a larger skewness, the explicit part of the equation requires small time steps. In rare cases, it may also reduce the stability of the solution. A steady-state solution is obtained when the differences of variables between two iterations become small and remain below an acceptable limit.

2.2.2 Determination of cross-derivatives and boundary values

The values required for the cross-differences, such as h_{ne}, are calculated with a linear interpolation method described by *Perić* (1985). If a cell face value like h_e is evaluated by means of linear interpolation between nodes P and E, one obtains:

$$h_e = h_E f_1^P + h_P(1 - f_1^P) \tag{29}$$

Here, f_1^P is a linear interpolation factor, associated with a particular node P and x_1 coordinate direction, and defined as:

$$f_1^P = \frac{\overline{Pe}}{\overline{Pe} + \overline{eE}} = \frac{\Delta x_1^P}{\Delta x_1^P + \Delta x_1^E} \tag{30}$$

where $\overline{Pe}$ and $\overline{eE}$ are the distances of cell face location "e" (cell face center) from nodes P and E, respectively. These are equal to the half cell arc lengths along the x_1 coordinate for P and E cells, Δx_1^P and Δx_1^E, respectively. Similar, the linear interpolation coefficients are defined for the other two coordinate directions, f_2^P and f_3^P.

The head differences in Eq. 19 can now be expressed as:

$$\begin{aligned}(h_n - h_s)_e &= (h_n - h_s)_P(1 - f_1^P) + (h_n - h_s)_E f_1^P \\ (h_t - h_b)_e &= (h_t - h_b)_P(1 - f_1^P) + (h_t - h_b)_E f_1^P\end{aligned} \tag{31}$$

Expressions similar to Eq. 31 follow for the other cell faces. Using interpolation coefficients f_1, f_2 and f_3, the values at cell face centers around node P can be calculated as:

$$\begin{aligned}h_n &= h_N f_2^P + h_P(1 - f_2^P) \\ h_s &= h_S f_2^S + h_S(1 - f_2^S) \\ h_t &= h_P f_3^P + h_P(1 - f_3^P) \\ h_b &= h_B f_3^B + h_B(1 - f_3^B) \\ h_e &= h_E f_1^P + h_P(1 - f_1^P) \\ h_w &= h_P f_1^W + h_W(1 - f_1^W)\end{aligned} \tag{32}$$

The extrapolation of the cross-differences on impermeable borders is also performed according to a procedure described by *Perić* (1985): an additional row of ghost-nodes with zero-thickness is added to the outside nodes. Due to this additional row, no other modifications are necessary, because these ghost-nodes allow the general interpolation scheme to be applied also at the borders.

In case of a head boundary-condition (Dirichlet boundary condition), no special treatment is necessary.

2.2.3 Temperature and pressure dependence of physical properties

In coupled simulations the fluid properties density, viscosity, compressibility, specific heat capacity, and thermal conductivity, are updated simultaneously during the numerical simulation according to varying pressure and temperature conditions. To this end, the program uses a special code described in *Wagner and Overhoff* (2006) and *Wagner and Pruß* (2002).

Temperature and pressure dependence of rock thermal conductivity and rock specific heat capacity is accounted for by polynomial interpolation as described in *Clauser* (2003).

2.2.4 Grid quality

When using curvilinear non-orthogonal grids, the quality of the grid has a significant impact on the solution (e.g. *George*, 1996; *Jacquotte*, 1998). For awkward grid-geometries, numerical calculations on non-orthogonal grids may yield wrong results or diverging solutions. For the method presented here, problems may arise when the cross-derivatives dominate the normal-derivatives (*Ferziger and Perić*, 2002). Therefore, the code includes some routines to analyze grid quality.

George (1996) suggested a criterion for the quality of a 2D-grid: the ratio of an outer and inner circle around a cell, which should be ideally equal to $\sqrt{2}$. However, this method is only adequate for 2D-triangles. 3D-hexahedral grids are far more difficult to evaluate. For the program presented here the problem is solved using an analogy: grid quality is calculated as ratio of the mean of all distances from the cell center to the eight corners (which is somewhat similar to the outer sphere) to the mean of all distances from the cell center to the center of the six cell-faces (similar to the inner sphere). Thus the result for an ideal cubic hexahedron would be $\sqrt{3}$.

Other grid quality properties which are checked by the program are the maximum skewness within the mesh.

In the method presented here, the line connecting neighboring control-volume centers ideally should be perpendicular to the cell-face normal (*Ferziger and Perić*, 2002). Another grid property which is checked is the volume ratio of adjacent volumes. Based on Taylor series expansion, the grid growth ratio should ideally be in the range of 0.8 – 1.2 (*Fletcher*, 2000a).

Discretization errors are always reduced when a grid is refined. Reliable estimation of these errors requires a grid refinement study for each new application (*Ferziger and Perić*, 2002).

Grid generation is a large subject by itself (*Wesseling*, 2001). For a general introduction into the topic of grid generation and grid quality see e.g. *Thompson and Weatherill* (1998), and *Thompson et al.* (1985).

2.3 Verification and benchmarking

An important part in developing numerical programs is to verify against results of known analytical solutions. For this purpose, two different tests are presented in the following.

As no analytical solution exists for thermally driven free convection, the results of the new code have been compared (*benchmarked*) with the results of two other well tested and established codes: SHEMAT (*Clauser*, 2003) and $FEFLOW^{®}$ (*Diersch*, 2005). While the first code yields solutions for orthogonal grids, the second one is based on the finite element method (FEM) and can be applied to arbitrary grids.

2.3.1 Testing the influence of a higher skewness of the mesh

The following verification calculation demonstrates the robustness of the coordinate transformation approach against strong skewness. In contrast to *Loudyi et al.* (2007) grids which are randomly disturbed to obtain non-orthogonality have not been applied, because numerical errors are more easy to detect when a regular deformed grid is applied. However, the following test is very similar to the Kershaw test which the above mentioned authors have applied also. Solutions were computed on a regular grid which is sheared increasingly from 0° to 85°. The region has a thermal conductivity of 2 $Wm^{-1}K^{-1}$, there is no flow across the upper and lower boundaries, and fixed temperature is set along the right and left boundaries, according to a linear temperature distribution corresponding to a value of $60\,^{\circ}C$ at $x = 0\,m$ and $50\,^{\circ}C$ at $x = 10\,m$. Obviously the correct solution is a linear temperature distribution with parallel and vertical decreasing isotherms from left to right. Tab. 1 lists the root mean square error, calculated according to *Simpson and Clement* (2003), for increasing shear angles. Fig. 6 shows the difference of the steady state to the analytical solution. As can be seen the difference is negligible. Due to the similarity of the equations,

Table 1: Root mean square error (rmse) of a steady state conductive heat transport problem with increasing shear angle of the grid.

Angle	rmse ($10^{-12}\,K$)	Max. Error ($10^{-12}\,K$)
0	3.3	7.9
10	2.8	6.4
20	2.6	5.4
30	2.6	5.6
40	2.5	5.8
45	2.7	5.5
50	2.4	5.0
55	2.4	5.4
60	13.0	22.6
65	11.4	21.1
70	6.7	13.5
75	3.9	12.0
80	3.5	10.2
85	5.1	16.5

the result for the groundwater head would be similar. However the heat-transport equation can not be evaluated with this approach, due to its non-linearity.

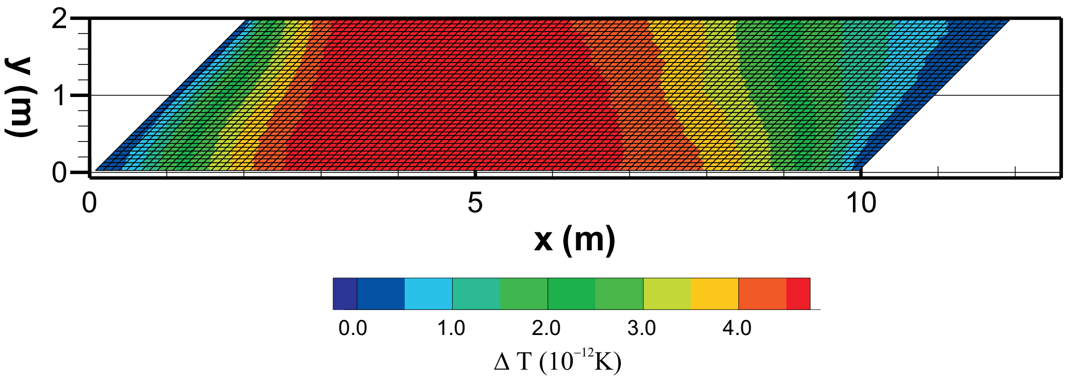

Figure 6: Absolute error of temperature calculated on a grid sheared by 45°.

2.3.2 Verification with an analytical solution for two-dimensional heat transport

An important part in developing numerical programs is to verify the code in order to ensure agreement of the results with known analytical solutions. In the following, the well known analytical solution of *Domenico and Palciauskas* (1973) is used for this purpose. This steady-state 2D problem is defined on a rectangular domain where the flow is driven by a spatially variable head at the top boundary according to a cosine function. This yields a non-symmetric distribution of temperature. Buoyancy is neglected.

The solutions for hydraulic head and temperature are:

$$h(x,z) = A - \left(\frac{B\cosh(\pi z/L)}{\cosh(\pi z_0/L)}\right)\cos(\pi x/L) \tag{33}$$

$$\begin{aligned} T(x,z) &= T_0 + q_b/\lambda(z_0 - z) + \left(\frac{\rho c q_b/\lambda K B}{2\lambda}\right)\left(\frac{cos(\pi x/L)}{cosh(\pi z_0/L)}\right) \\ &\quad \left\{(z_0 - z)cosh(\pi z/L) + L/\pi\left(\frac{sinh(\pi(z-z_0)/L)}{cosh(\pi z_0/L)}\right)\right\} \end{aligned} \tag{34}$$

Constants A and B are defined as $A = L/2 + B$, $B = cosh(\pi z_0/L)$. Where $L = 200\,m$ is the width and $z_0 = 100\,m$ is the depth extent of the model domain. $\rho = 998\,kg\,m^{-3}$ is density, $c = 4218\,J\,kg^{-1}\,K^{-1}$ is specific heat capacity, $\lambda = 3\,W\,m^{-1}\,K^{-1}$ is thermal conductivity, $q_b = 0.03\,W\,m^{-2}$ is specific heat flow at the base of the model and $T_0 = 10^\circ\,C$ is the temperature at the upper boundary. A $MATLAB^{®}$ code of this calculation is freely available[1].

In order to demonstrate the accuracy of the coordinate transformation approach, the numerical calculation was solved on a non-orthogonal grid. The grid is based on a simple sine transformation, it is not curvilinearly orthogonal and has the same number of grid-nodes as the orthogonal one (see Fig. 7). The maximum deviation from orthogonality is nearly 22°. The fixed values for the upper boundary condition are calculated with Eqs. 33 and 34 for the new top boundary nodes of the curvilinear grid.

The top panel of Fig. 7 shows the analytical results for the head. The relative deviations of the analytical and numerical values on a curvilinear grid are given in the bottom panel. Where the relative deviation, e.g. for the head, is calculated as:

$$\Delta h_{relative} = \frac{h_{analytic} - h_{model}}{h_{analytic}} \tag{35}$$

The root mean square error is $9.2\,mm$. The 'noise' visible in the latter figure is due to numerical roundoff and grid discretization errors.

[1] http://geomath.onlinehome.de/dp/dp.m

The top panel of Fig. 8 shows the analytical result for the convective temperature distribution. The relative deviation between this and the numerical result is shown in the bottom panel. The root mean square error is $9.2\,mK$.

An additional comparison (not shown here) with numerical results obtained on an orthogonal grid with the original SHEMAT code yields comparable accuracy.

The obtained result shows that the new code with the coordinate-transformation can compute heat transport problems with a very good accuracy.

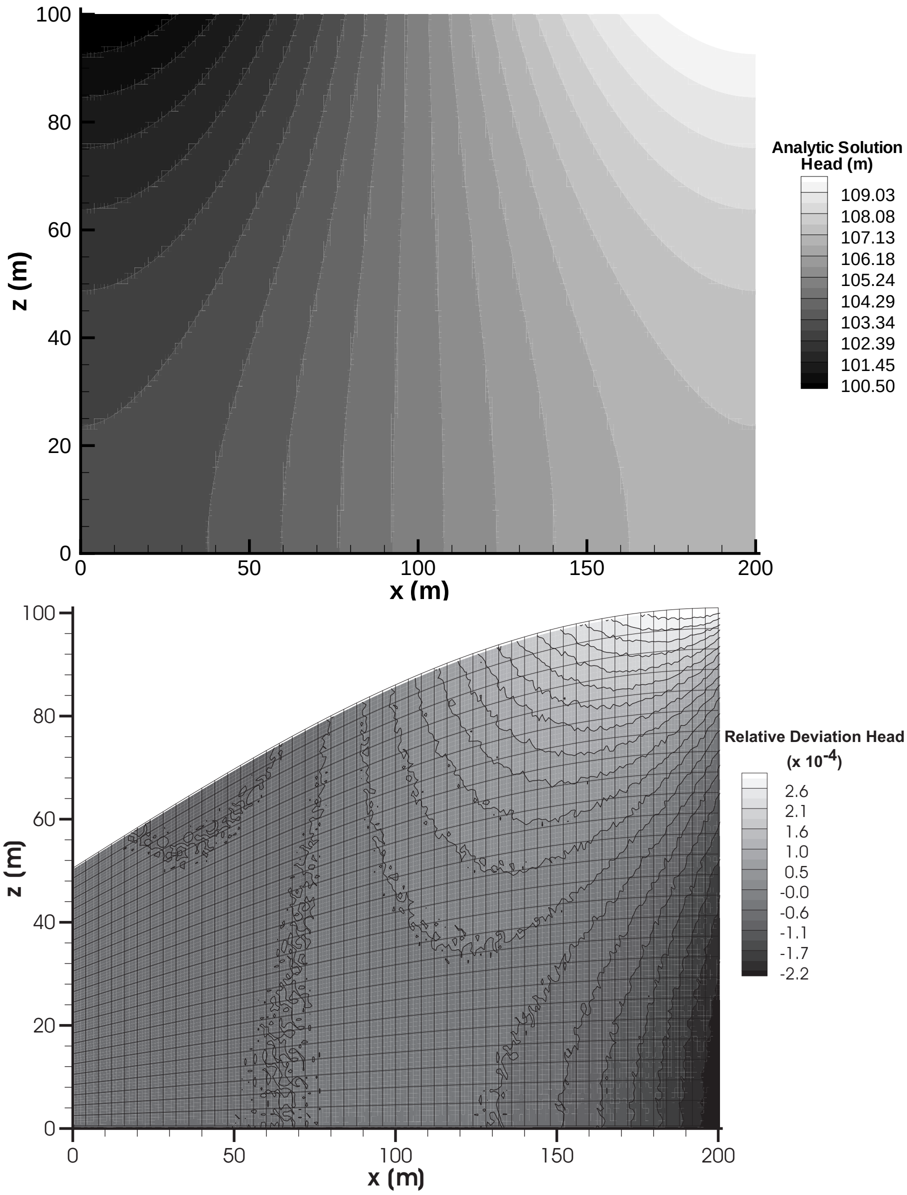

Figure 7: Top: the analytical solution for the head based on *Domenico and Palciauskas* (1973). Bottom: Relative deviation between the analytical and the numerical solution for the head in case of a non-orthogonal grid.

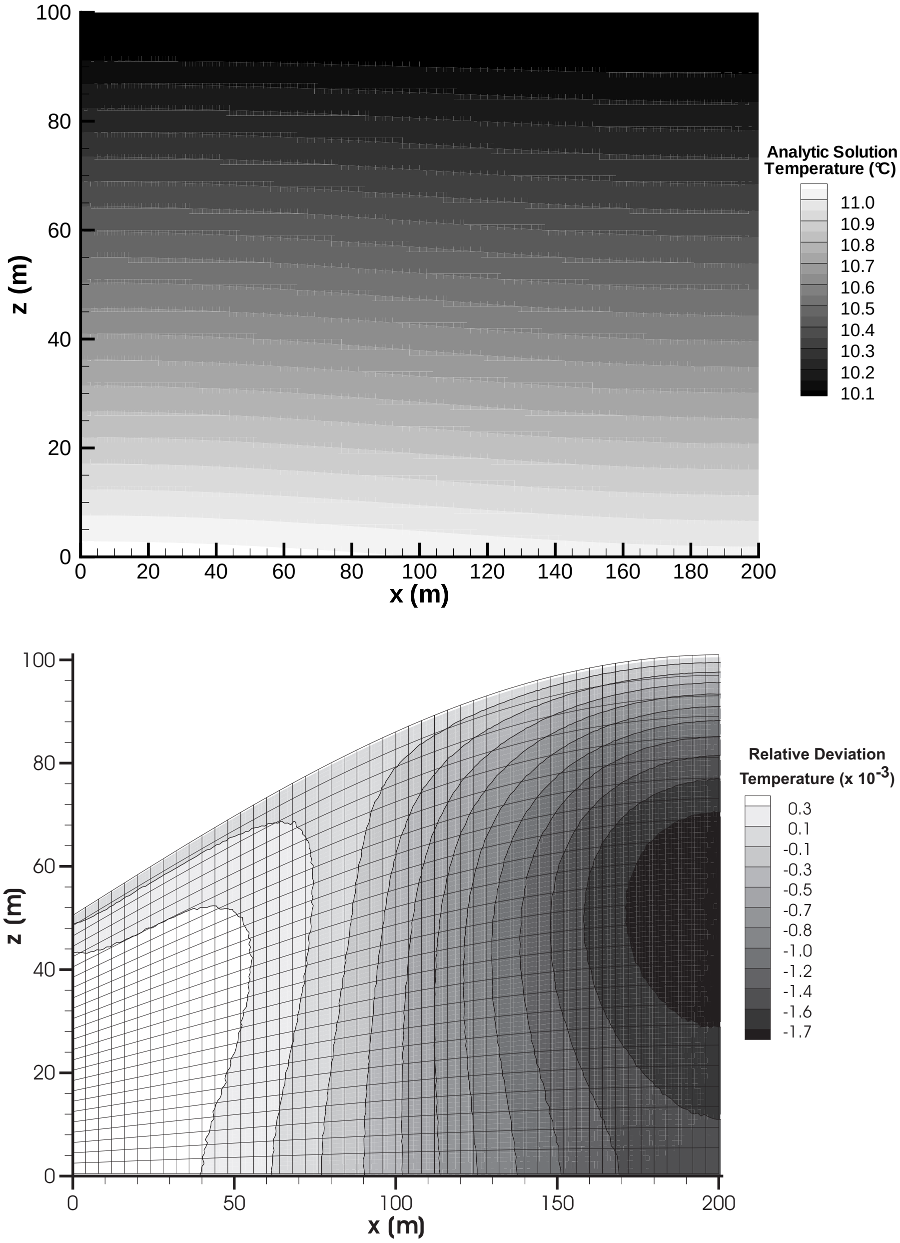

Figure 8: Top: The analytical solution for the temperature based on *Domenico and Palciauskas* (1973). Bottom: Relative deviation between the analytical and the numerical solution for the temperature in case of a non-orthogonal grid.

2.3.3 2D benchmark free convection

In addition to the verification, a benchmark is calculated to test results for a more complex case with flow driven by thermal buoyancy. Results of three different codes are compared: $FEFLOW^{®}$ (*Diersch*, 1994; *Diersch and Kolditz*, 2002), SHEMAT (*Clauser*, 2003) and the code presented here named 'sno'. Analytical solutions are not available for such a model.

Fig. 9 (left panel) shows the model grid with two different property zones. It extends $50\,m$ in the x- and $5\,m$ in z-direction. Table 2 lists the different physical properties for these zones, all of them isotropic. These values are arbitrary too, but they are approximately in the order of a typical basin (see for instance *Nunn et al.*, 1999). The size of the domain is approximately a thousand times smaller than a typical basin to speed up the computation time.

All model boundaries are no-flow boundaries. Due to this the model is particularly sensitive to changes in parameters or the numerical approximations. The initial head value is $100\,m$. With respect to temperature, the top and bottom boundaries are constant temperature (flow) boundaries at $10\,°C$ and $160\,°\,C$, respectively. All other boundaries are impervious. The initial values correspond to a linear temperature distribution with depth.

$FEFLOW^{®}$ and sno use an identical grid symmetry. For the SHEMAT model, the inclined boundary between the property zones is realized by steps on an orthogonal $0.125\,m \times 0.05\,m$ grid (right panel of Fig. 9).

The model is transient with a logarithmic output interval at 10^1, 10^2, 10^3, ..., 10^{12} seconds. The time step size has been adapted to give stable results and increases similarly. For practical reasons, only the result at time-step 10^8 s is discussed, which is the first output showing a convection cell.

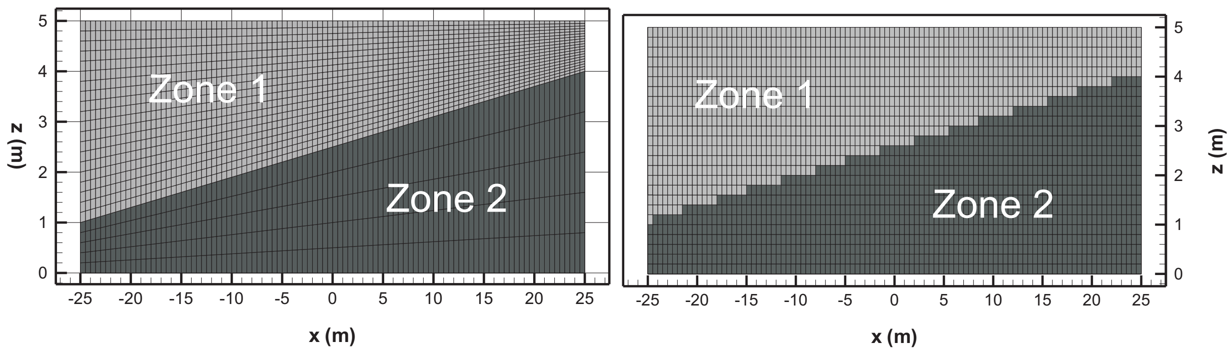

Figure 9: The benchmark grid with the different property zones. Only every fourth grid-line is shown. Left and right panels show the non-orthogonal and orthogonal grids, respectively.

Table 2: The physical properties applied for the benchmark model.

	k (m^2)	ϕ (/)	λ ($Wm^{-1}K^{-1}$)	$\rho_g c_g$ ($MJm^{-3}K^{-1}$)
Zone 1	$1 \cdot 10^{-16}$	0.3	2.0	2.52
Zone 2	$1 \cdot 10^{-21}$	0.3	3.5	2.52

This benchmark is in general highly sensitive against even small parameter changes or changes of the numerical routines. However, as Figs. 10, and 12 show, all three codes yield the same qualitative result regarding the velocity, showing a conspicuously counter clock-wise convection cell.

The z-component of velocity deviates for the orthogonal grid from the non-orthogonal grid, yielding high values near the steps of the boundary between the high and low hydraulic conductivity domains of the model (Fig. 11). Due to these high-velocity regions the solution in general is (although fully implicit) more unstable than the one calculated on the non-orthogonal grid (with its partly explicit numerics due to the cross derivatives).

As discussed earlier, tests of this benchmark with a randomly distorted grid showed that no valid solution can be obtained with the code presented here, if the grid is not parallel to gravity. This is due, on the one hand, to the problem of transformation of the buoyancy term, on the other hand it is due to the general no-flow boundary conditions. In case of flow boundary conditions, for instance, at the right and left side, the result would be influenced less. However, it is common practice to use grids for modeling subsurface flow which are parallel to gravity into their vertical direction. Rare cases where more complex grids are necessary may be the modeling of flow along salt-diapirs and comparable problems.

The result with the non-orthogonal grid shows high velocities at the border between the upper and lower zone at the right boundary. This is due to the right no-flow boundary condition. There, the flow is forced downward. Relatively large potential differences occur at this location (see top of Fig. 10) corresponding to velocities two to three times larger than in the neighborhood. As the benchmark is very sensitive to small changes, the result obtained with the orthogonal grid does not show this feature, due to the small distortions within the flow-field resulting from the steps along the two different property zones.

The solution by $FEFLOW^{®}$ yields similar flow fields, although the head values are different from the SHEMAT/sno solution. This may be due to $FEFLOW^{®}$'s use of the Oberbeck-Boussinesq approximation (*Kolditz et al.*, 1998) which is not applied in SHEMAT and sno. Another explanation may be the different numerical approach. However, $FEFLOW^{®}$ does also show the high velocity area at the right border.

The temperature distribution is shown in Fig. 13. It shows a good agreement between SHEMAT and sno. The non-linear temperature distribution is primarily due to the lower thermal heat conductivity in zone 1 compared with zone 2.

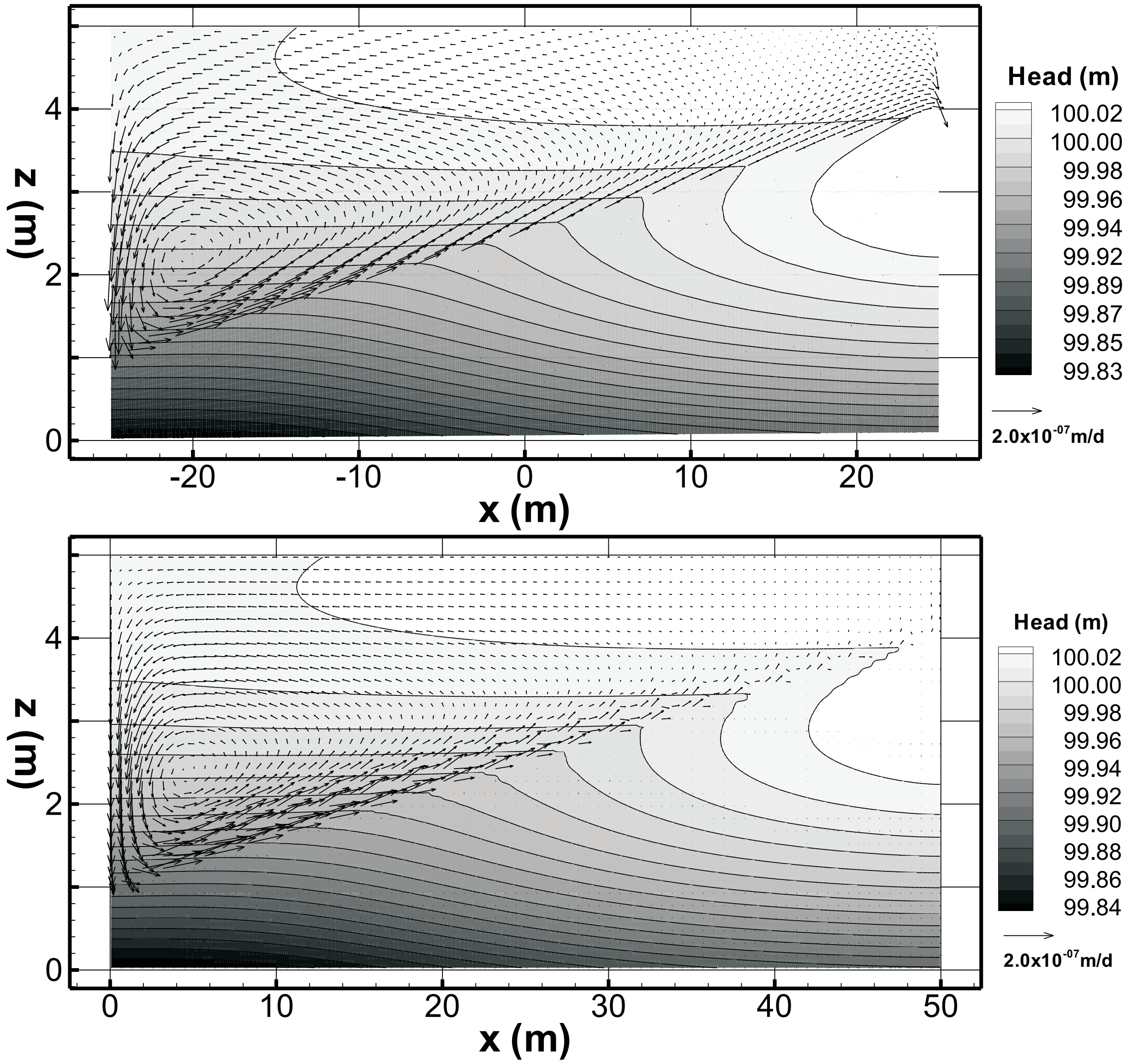

Figure 10: Head distribution for the model in Fig. 9 after $10^8\,s$. Top and bottom panels show the solution computed with sno on a non-orthogonal grid, and computed with SHEMAT on an orthogonal grid. Additionally, the flow fields are shown by arrows.

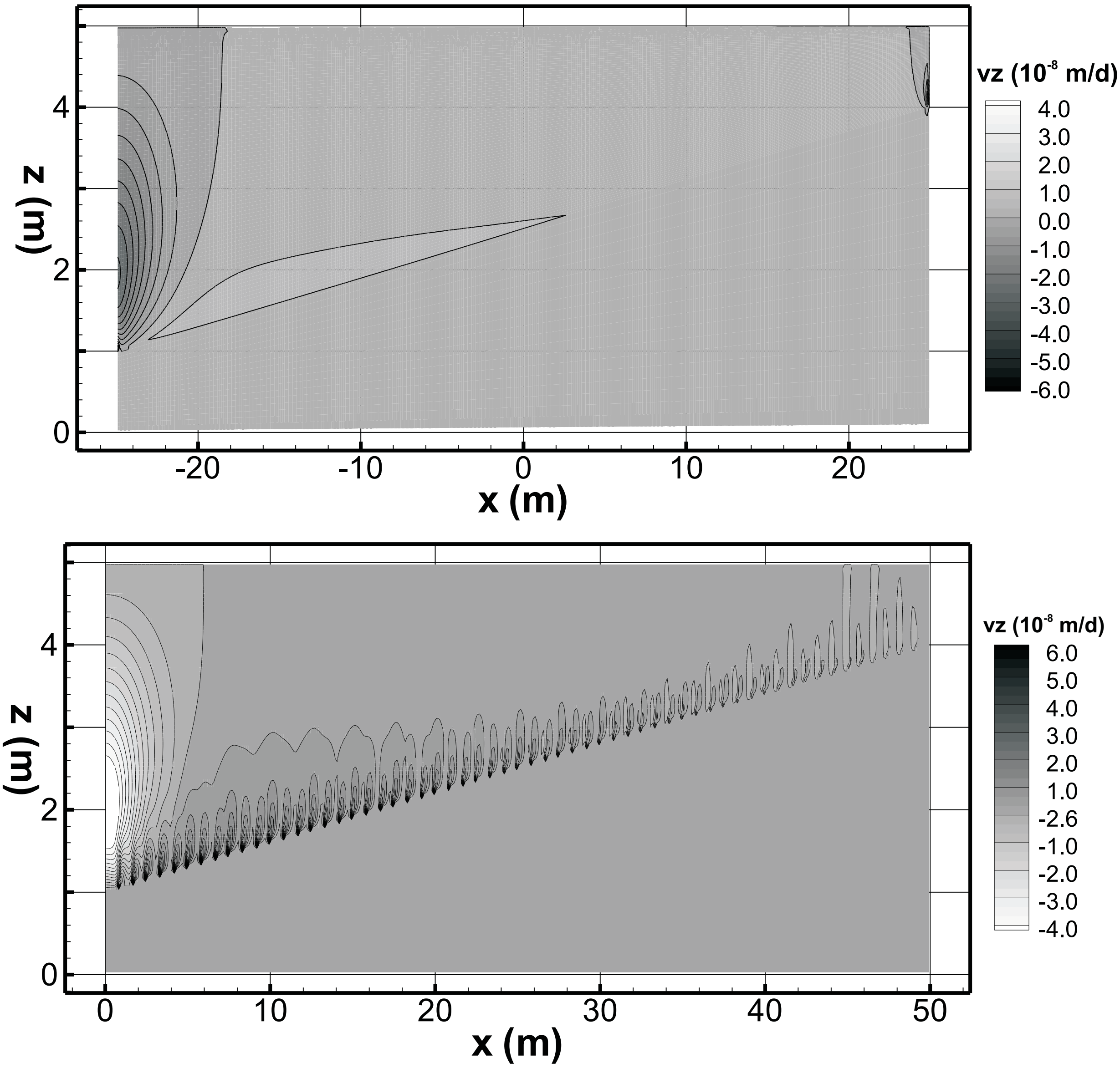

Figure 11: Velocity distribution of the z-component for the model in Fig. 9 after $10^8\,s$. Top and bottom panels show the solution computed with sno and SHEMAT on a non-orthogonal grid, and on an orthogonal grid, respectively.

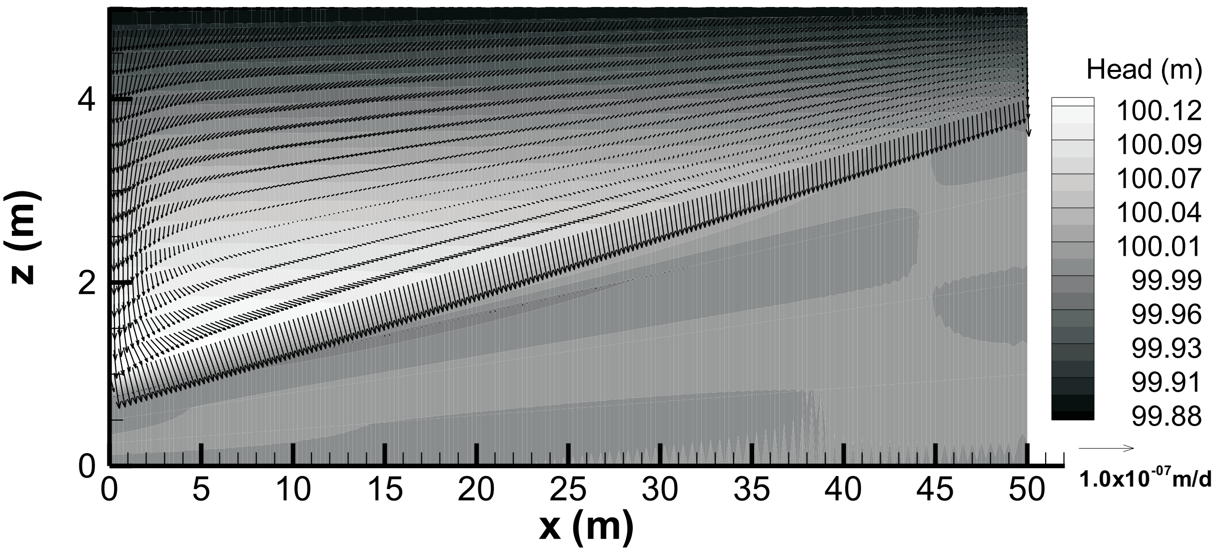

Figure 12: Simulation result obtained with $FEFLOW^{®}$ on a non-orthogonal grid for 10^8 s; head (contours) and groundwater velocity (arrows).

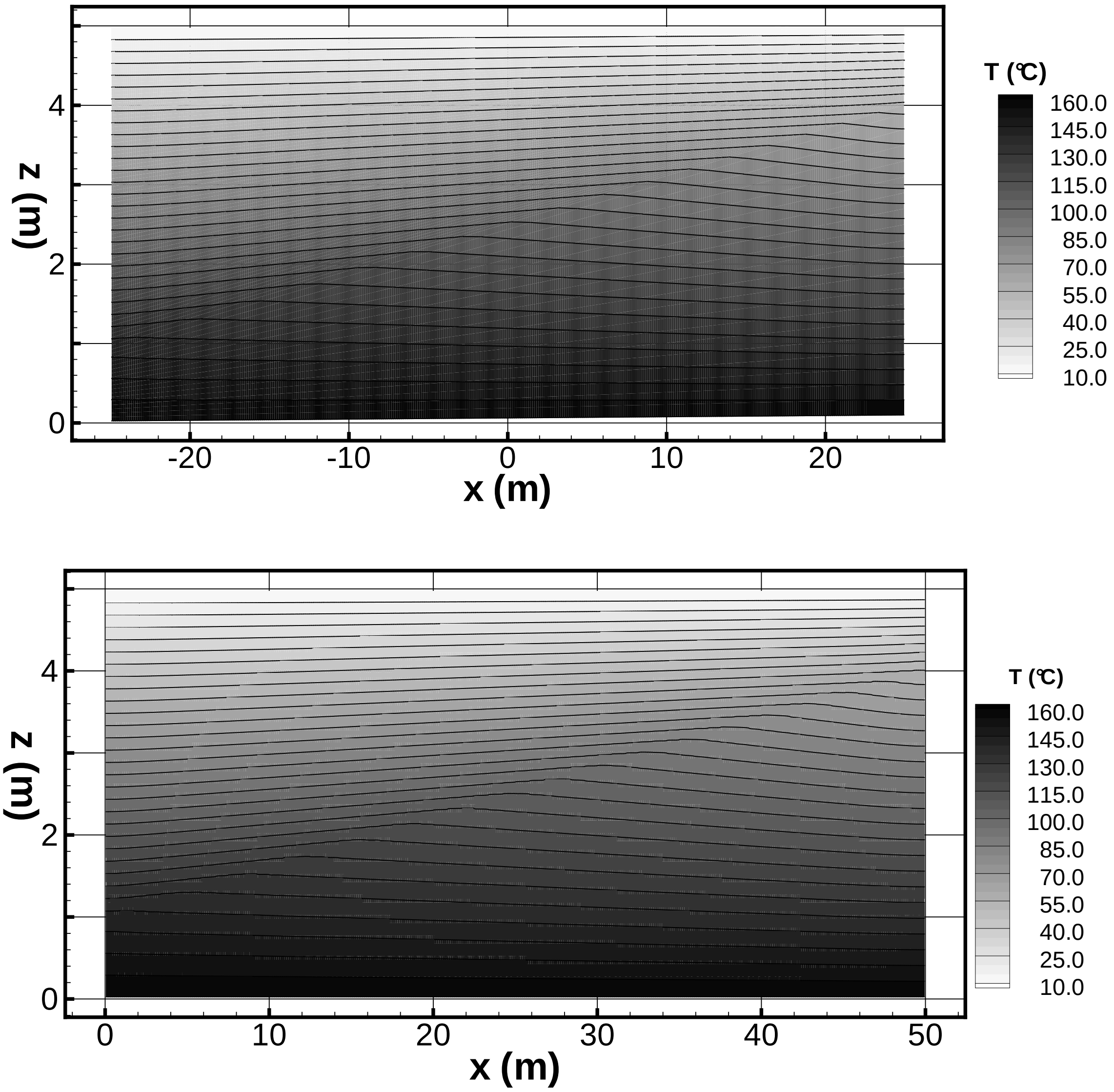

Figure 13: Temperature distribution for the model in Fig. 9 after $10^8\,s$. Top and bottom panels show the solution computed with sno and SHEMAT on a non-orthogonal grid and on an orthogonal grid, respectively.

2.3.4 3D benchmark free convection

To demonstrate the 3D capabilities of the sno-code, the 2D benchmark discussed above was translated into to a 3D problem. The height of the basal unit varies in the y-direction (see Fig. 14).

For comparison, this problem was again simulated with the original SHEMAT on an orthogonal grid (similar to the right one in Fig. 9). Fig. 15 and Fig. 16 show that the results are very similar.

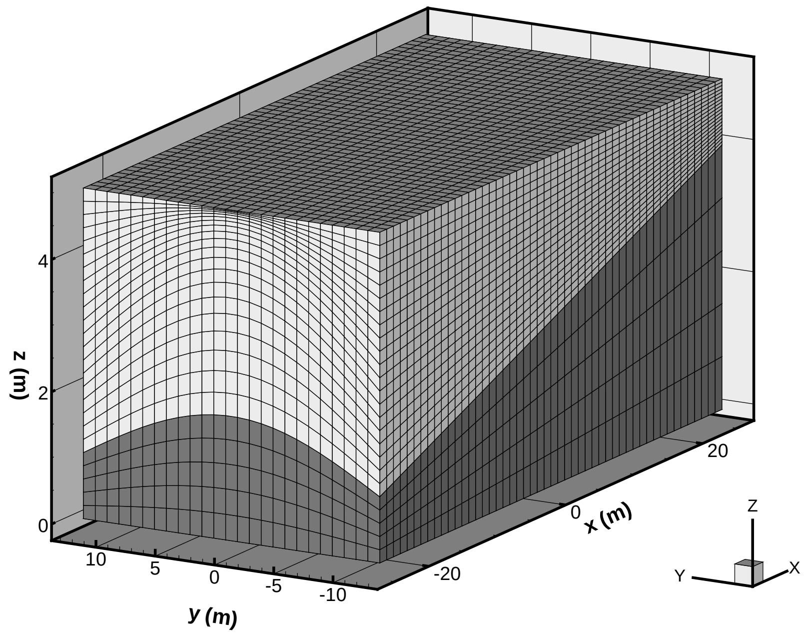

Figure 14: The 3D benchmark grid with the different property zones. Only every fourth grid-line is shown.

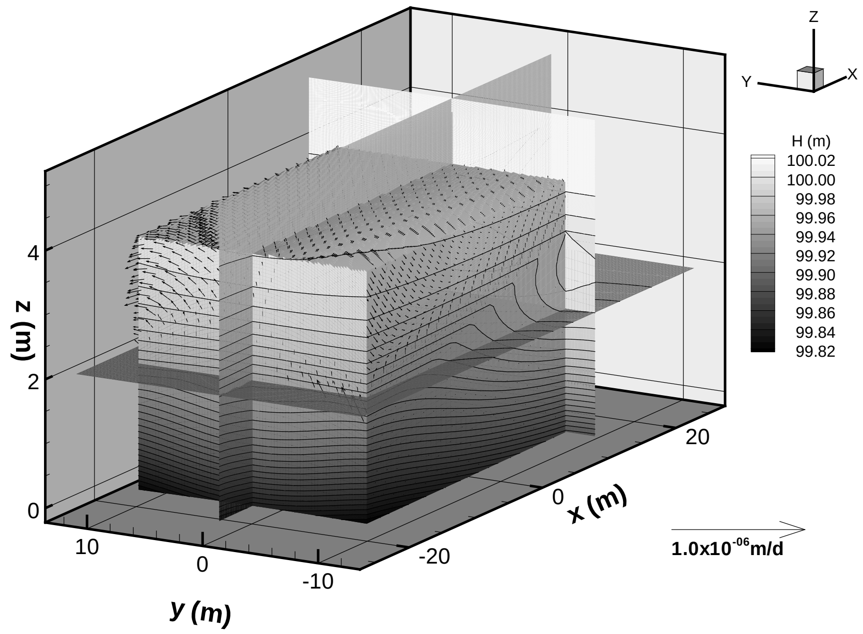

Figure 15: Head distribution for the 3D benchmark model, computed with sno on a non-orthogonal grid, after $10^8\,s$. Additionally the flow field is shown by arrows.

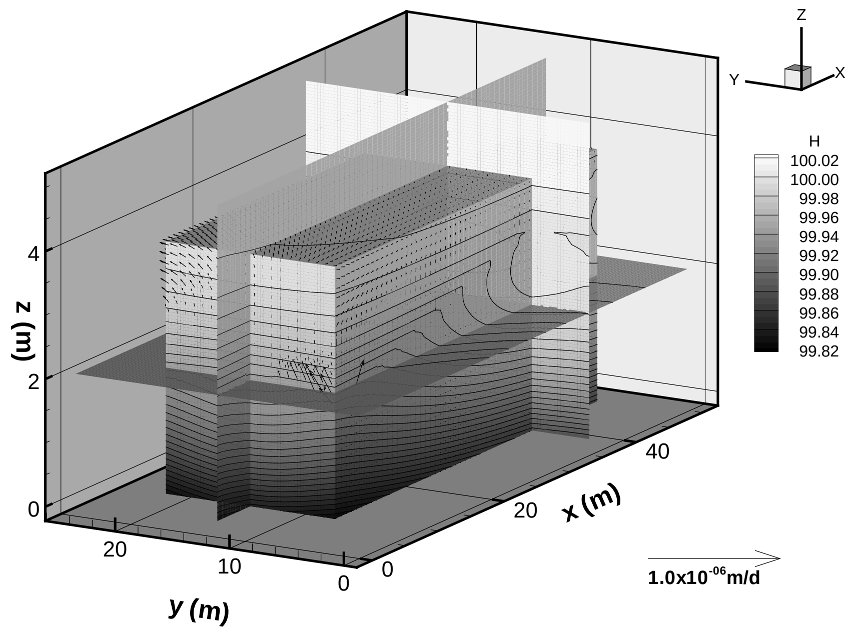

Figure 16: Head distribution for the 3D benchmark model, computed with SHEMAT on an orthogonal grid, after $10^8\,s$. Additionally the flow field is shown by arrows.

2.4 Conclusions - coordinate transformation method

A coordinate transformation method permitting the use of 3D-non-orthogonal grids, was implemented into an existing code using the finite volume method. The code is applicable to a variety of single-phase flow and heat transport problems. As non-orthogonal structured grids allow a better spatial representation of the modeling domain - often with a smaller number of nodes - the new code may be helpful and can increase the accuracy of results and predictions deduced from them. Additionally, it is possible - often without increasing the number of nodes - to refine areas with higher groundwater velocities for instance along fault zones (*Yang et al.*, 2004). However, as the code is restricted to structured hexahedral grids, it is not possible to apply adaptive mesh refinements as in some finite element codes (see e.g. *Signorelli et al.*, 2007). The coordinate transformation method applied here is straightforward and increases the flexibility of finite difference and finite volume modeling for complex geometries considerably. For geothermal basin analysis it is an advantage to model the basin geometry as accurately as possible. Non-orthogonal 3D body-fitting grids are a clear advantage here.

Sufficiently accurate results were obtained from analytical and benchmark problems. In contrast to the computational error which is discussed in this paper, *Fletcher* (2000b) gives some information with regard to the mathematical errors associated with the use of generalized coordinates. In general, appropriate mesh quality criteria are important when non-orthogonal grids are used. Numerical errors may occur in case of highly skewed grids. This is due mainly to the dominance of the explicitly solved cross-derivatives.

A restriction for the approach presented here is that buoyancy driven models can only be computed correctly if the vertical grid lines are parallel to the gravity vector. Although most hydrogeologic subsurface models fulfil this requirement, more flexible grids may be necessary in some rare cases. Circumventing this shortcoming will be work for the future. As discussed earlier in section 2.2.1 two solutions are possible: a different numerical application of the Darcy equation or a least-squares method.

A simple graphical user interface is available which uses *GOCAD*® (*Mallet*, 2002) and *Tecplot*® or *VTK*® for pre- and post-processing respectively. It is coded in *Java*® and will therefore run on most computer systems.

Some functions of the original SHEMAT are not yet implemented or still untested.[2] The inclusion of these routines is only a technical matter. The mathematics remains the

[2]Missing functions are: free water-surface, unsaturated zone, chemical reactions, solute transport and frozen soil

same, also on non-orthogonal grids.

Additional routines could be included in the code presented here. Currently, the original 7-point stencil solver is still used for the computations with the disadvantage of solving the additional non-orthogonal terms with an explicit approach. For a more general application of this code the implementation of a 19-point stencil BiCGStab solver (see e.g. *Saad*, 1996) is desirable. With non-orthogonal grids, the number of required grid nodes decreases, in general. However, an additional adaptive mesh refinement restricted to regions were it is required would be an additional advantage. A simple upwinding scheme and a time-step weighting scheme are already included. In the field of geothermal modeling, fracture flow is often important. Therefore, the possibility to include discrete fractures, represented as 2D-elements would be favorable. Currently, only boundary conditions of Neumann (flow) and Dirichlet (potential) type are included. Future releases should include the additional option to apply mixed boundary-conditions of the Cauchy type. As interaction of surface and subsurface water is of increasing importance in applied hydrological modeling (*Mölders and Rühaak*, 2002), the inclusion of an overland-flow, lakes, and river-dynamics module is desirable. Additionally, an existing inverse version of SHEMAT (*Rath et al.*, 2006) may be modified in the same way in the future.

An especially interesting approach would be the extension of the coordinate-transformation method onto unstructured tetrahedron grids.

3 Detection and quantification of thermal anomalies in a sedimentary basin - a case study

Little work has been published on the hydrothermal regime of the western part of the Molasse Basin in South Germany, except for the studies of *Vollmayr* (1985) and *Bertleff and Watzel* (2002). There are some unpublished reports, though, which consider flow models of smaller areas or selected units. Previously, *Rath and Clauser* (2005) reported the first hydrothermal 3D-model for the entire area. The work presented here is focused on some of the problems identified in this study. In particular, no fully coupled flow model is computed, due to the lack of the required data. Instead, a purely conductive model is computed which is considered more reliable.

This conductive model provides more reliable information than a coupled flow and heat-transport model as it is based solely on the thermal properties and on the basin geometry, which are the best available records. However, the result can be discussed only in a qualitative manner as the advective processes are not included and must be deduced from the differences between data and results of conductive models.

Questions regarding the history of the basin and tectonic aspects are not discussed in this study. Some work on the evolution of the Molasse Basin has been performed by *Lemcke and Tunn* (1956) and *Lemcke* (1976, 1984). However, some critical parts of these studies were later questioned by *Bertleff and Watzel* (2002).

The following method was applied in this study to detect areas disturbed by groundwater flow using temperature measurements: In a first step, the conductive thermal regime is simulated. For this purpose it was necessary to

1. build a structural subsurface model of the study area;
2. collect thermal properties of the local rocks;
3. compute a numerical conductive heat transport model;
4. compare the numerical results with the measured temperatures corrected for paleoclimate.

In a second step, advective heat transport is studied, using information about the flow regime and by applying a two-dimensional Péclet and Rayleigh number analysis. The final third step is the fully coupled simulation of a simplified type model for explaining the detected major thermal anomalies. This analysis and the results are presented and discussed in the following.

3.1 The structural subsurface model

The model area is part of a sedimentary basin containing mostly Tertiary clastic sediments from the Alpine orogenesis, and Mesozoic clastic and carbonate sediments overlying the crystalline basement. The basin has a wedge structure with a moderate dip towards SSE.

A subsurface model (Fig. 17) was generated using the *GOCAD*® software (*Mallet*, 2002). Neither seismic nor gravity data were available for this area. Therefore, the model is solely based on geological information obtained from a drilling data base. Unfortunately, petrographic information is rare, making it necessary to work with stratigraphy and to assume that it correlates adequately well with the lithological thermal properties. However, this postulated general correlation between petrophysical and stratigraphic data is a commonly accepted idealization (see e.g. *Person et al.*, 1996).

The stratigraphic information from the original data base was simplified into 15 basic units based extended data base queries (see Tab. 5), which resulted in 1150 depth values for the base of units. Due to an inconsistent data distribution the layer depth had to be used and not the layer thickness as often only a single depth value exists without the associated values for the upper or lower units. It is therefore not possible to work with the layer thickness without omitting a large number of the single values.

Two units were ignored: Cretaceous rocks occur only in patches in a small part of the extreme southeastern corner of the model area, and their classification is also often questionable. Regarding the Lower Marine Molasse (UMM), Fig. 1 shows that its distribution starts in the southeastern corner of the model area. However, the data base only contains a few values for the extreme southeastern corner of the model area. This is insufficient to generate a layer. Therefore, this small UMM region was included in the Lower Freshwater Molasse (USM) because of its similar physical properties.

I tried to validate the model by including 13 interpreted geological sections, most of them from *Bertleff and Watzel* (2002) and some unpublished results of the work presented in *Koschel* (1989). However, apart from a general confirmation of the model this did not improve the quality of the model.

Vertical fault displacements were not integrated as discrete elements, because too little information is available on their geometry and the displacement for an integration into the 3D-model.

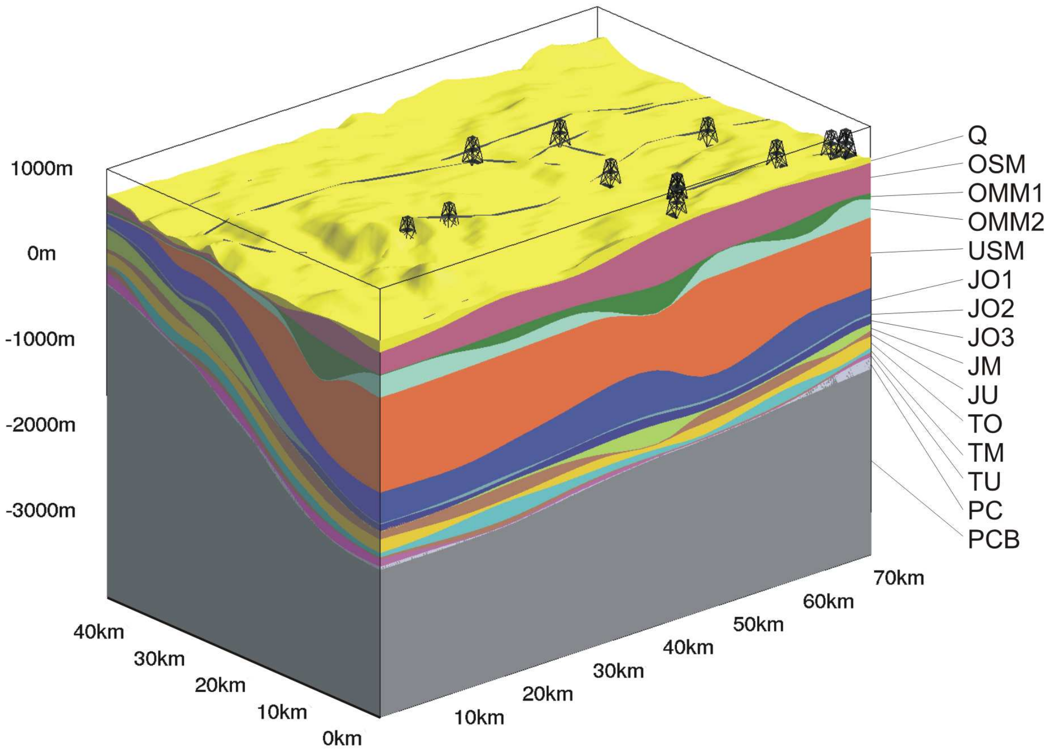

Figure 17: The structural $GOCAD^{®}$ model for the conductive heat transport simulations (corresponding to the rotated black rectangle in Fig. 1). The model area is $70\,km \times 45\,km$. The horizontal grid size is 500 m (140 $\times$ 90 cells), the vertical grid size is variable (43 cells). The derricks mark the locations with continuous temperature logs. The key for the stratigraphy is explained in Tab. 5.

3.2 Temperature data

A temperature data base for Germany has been maintained and updated since 1977 at the Leibniz Institute for Applied Geosciences (GGA Institute) in Hannover (*Pribnow and Schellschmidt*, 2000). This study used 3790 temperature values of which 3420 are re-sampled from 13 undisturbed continuous temperature logs. The remaining 370 values are bottom hole temperature (BHT) measurements and drill stem tests (DST). The BHT data have a much larger spatial (especially lateral) distribution than the other temperature data (see Fig. 1). However, the quality of BHT measurements is low because they are recorded right after drilling when the thermal field is in disequilibrium. The data were corrected using different approaches resulting in different data quality. Nevertheless, because of the residual error, the accuracy is estimated to be $3\,K$ for corrected BHT and $0.01\,K$ for continuous logs (*Bächler et al.*, 2003). Current research is looking into improving the methods for correcting BHT data (see for example *Förster et al.*, 1997; *Förster and Merriam*, 1999a; *Förster*, 2001; *Waples and Ramly*, 2001; *Andaverde et al.*, 2005; *Zschocke*, 2005).

In Tab. 3, the different corrections which were applied to the data and the associated error weighting values are shown. The weighting is based on expert knowledge and extensive testing. Tab. 4 shows the distribution of the different quality classes in the model area. For the 3D-interpolation of the temperatures an interpolation was used which takes into account the weighting factors in Tab. 3 (*Rühaak*, 2006).

Table 3: Temperature data weighting classes.

No.	Weighting	Description
1	1.0	measurement from undisturbed logs
2	0.2	measurement from disturbed logs
3	0.7	BHT measurement with at least 3 temperature measurements T=T(t) at one depth; corrected with a cylinder source approach
4	0.63	BHT measurement with at least 3 temperature measurements T=T(t) at one depth; corrected by using the Horner plot method
5	0.63	BHT measurement with at least 2 temperature measurements T=T(t) at one depth; corrected with a explosion line-source approach
6	0.35	BHT measurement with one temperature measurement, known radius and time since circulation (TSC)
7	0.35	BHT measurement with one temperature measurement, known TSC or known radius
8	0.14	BHT measurement with one temperature measurement, unknown radius and unknown TSC
9	0.7	measurement from DST

Table 4: Frequency of the different classes of temperature weights, see Tab. 3.

Weight	1	0.7	0.63	0.35	0.2	0.14
Count	3420	14	72	40	50	194

3.2.1 Quality weighted interpolation

The inverse-distance weighting method (IDW) is used widely by earth scientists (*Ware et al.*, 1991). A great advantage of IDW is its simplicity: in the simplest case the grid is just a function of the inverse distance of the surrounding scattered data-points. This makes IDW easy to expand for special purposes (e.g. *Bartier and Keller*, 1996, *Tomczak*, 1998). The IDW algorithm for interpolation of 3D scattered data can be written as (*Shepard*, 1968):

$$v_{x,y,z} = \frac{\sum_{i=1}^{n} \left(\frac{v_i}{h^b}\right)}{\sum_{i=1}^{n} \left(\frac{1}{h^b}\right)} \tag{36}$$

with

$$h = \sqrt{\delta^2 + \sigma^2} \tag{37}$$

and

$$\delta = \sqrt{\Delta x^2 + \Delta y^2 + \Delta z^2} \tag{38}$$

where v_i is the value of the original function,

$v_{x,y,z}$ is the interpolated function value on the x, y, z - grid.

δ represents the effective distance between the nodes and v_i, and Δx, Δy, Δz are the grid distances to v_i.

Eq. 36 includes three weighting parameters:

- b is the weighting or power parameter (it is also possible to use b in a manner that a point on a grid node gets a b of 1 and points off the grid a b of zero);
- $0 \leq \sigma \leq 1$ is the smoothing parameter.

The univariate IDW method assumes that the surface between any two points is smooth but not necessarily differentiable (*Ware et al.*, 1991). One of the characteristics of the IDW is the generation of "bull's-eyes" surrounding the position of observation within the gridded area. By assigning a smoothing parameter this effect may be reduced on the by smoothing the interpolated grid.

In some cases, not all measured data of a set have the same quality: some data are better than others. Very often the degree of accuracy is known only approximately. Despite the availability of expensive geostatistical methods to interpolate data with respect to their quality it is common practice to interpolate these data together. The approach proposed here is to assign different weights to the data based on their quality. For inclusion of this weight into the interpolation algorithm, Eq. 36 can be extended to (*Rühaak*, 2006):

$$v_{x,y,z} = \frac{\sum_{i=1}^{n} \left(\frac{\varphi_i \cdot v_i}{h^b} \right)}{\sum_{i=1}^{n} \left(\frac{\varphi_i}{h^b} \right)} \tag{39}$$

Where $0 \leq \varphi_i \leq \kappa$, here κ may be a large number, is a weighting parameter, it is included for data with different qualities. The ratio between the different φ values defines the weight. If a datum has a weight of $\varphi = 0$ it is omitted.

This method is of special importance if the different quality classes are not clearly separated which may lead to serious misinterpretations. Using the procedure proposed here, the impact of low quality data is negligible where good data are available. On the other hand, it is still possible to interpolate regions where no high-quality data exist.

Unfortunately, no established statistical method is available for calculating such weights. However, for visualization purposes, it is possible to assign estimated quality-weights based, for instance, on known measurement errors. For assigning these weights some expert knowledge is necessary.

Although in most cases the number of different qualities is small, the developed program is also capable of using continuous weights.

The weights should consider the scaling type of the data (e.g. linear or logarithmic) and the amount of acceptable error. The latter defines the zero weight for data with a larger error.

For instance, if a data set has some values with a measurement error of 2 % and others of 10 %, the simplest approach is to assign a weight of 1.0 to the more accurate measurements and a significantly smaller arbitrary weight to the others. This procedure should be tested and analyzed visually. Based on general assumptions the weight should be varied until the result is sufficiently accurate.

To explore the data, it is helpful to interpolate the different quality classes separately. This can be done by assigning a zero weight to all but one data class, repeating this for all classes. This can be carried out easily in any spreadsheet software tool. Every interpolation should be analyzed with care and compared visually to the others. This method can help additionally to identify the impact of the less accurate data within the joint interpolation. For further details see *Rühaak* (2006).

3.2.2 Correction for paleoclimate

Among others, *Kukkonen and Clauser* (1994) showed that temporal changes in surface temperature cannot usually be ignored in temperature data interpretations in basin analysis. In this area, in particular, glaciation during the Pleistocene induces a considerable curvature in the temperature profiles. Therefore, the transient effect of paleoclimate which could be mistaken as an advective signal is taken into account by subtracting its present signal from the measured data using the approach and code of *Hartmann and Rath* (2005).

3.3 Conductive heat transport

In terms of a conceptual model (see for instance *Anderson and Woessner*, 1992), the approach is to assume that three main factors have an impact on the subsurface temperature: (1) heat conduction, (2) heat advection, (3) a paleoclimate signature.

Conductive and paleoclimatic components have been calculated and it is assumed that the advective part is identical to the calculated residual between computed and measured temperatures. This approach is, of course, limited by the natural variation of the relevant physical properties - in this case thermal conductivity. Compared to e.g. permeability, thermal conductivity of rocks and sediments varies relatively little between approximately $1.5\,Wm^{-1}K^{-1} - 3.5\,Wm^{-1}K^{-1}$ (see e.g. *Clauser*, 2006). Moreover, the conductive heat distribution is always smooth and continuous. Therefore, the results remain valid despite the inevitable errors in selecting appropriate values of thermal conductivity.

The grid necessary for the finite volume simulation was generated directly from the structural subsurface model by *GOCAD*® using SGrid volumes (hexahedral curvilinear structured grids).

The heat conduction equation in Cartesian coordinates follows from the conservation of energy (e.g. *Clauser*, 2003):

$$\rho_g c_g \cdot \frac{\partial T}{\partial t} = \nabla(\lambda \nabla T) + H. \tag{40}$$

Which is a simplified form of Eq. 7.

In steady-state solutions, the time derivative becomes zero and the equation simplifies to:

$$\nabla(\lambda\nabla T) + H = 0. \tag{41}$$

Several codes are available for the numerical solution (see e.g. *Anderson*, 2005). Here the software *sno* (*Rühaak et al.*, 2008) is used, which is described in the first part of this thesis and which is a modified version of SHEMAT (*Clauser*, 2003). Unlike the original software, *sno* uses non-orthogonal, structured, stratigraphic, hexahedral grids.

3.3.1 Model parameters

The model's horizontal size is $70\,km \times 45\,km$, in the vertical it extends from -5000 m below sea level up to the actual topographic surface. In both horizontal directions the model is discretized into an equidistant grid with a 500 m increment. In vertical direction the grid is non-equidistant and follows the geometry of the strata.

The thermal parameters derive from different sources: For the Tertiary units there are some measurements from core analysis (*Rath and Clauser*, 2005). Further data are derived from property reconstructions based on borehole logs (*Hartmann et al.*, 2005). In addition, some data were taken from the literature (*Cermák and Rybach*, 1982; *Häfner et al.*, 1992; *Clauser*, 2006; *Kutasov*, 1999; *Haenel et al.*, 1988; *Leu et al.*, 1999). The Malm (Upper Jurassic) data derive from an internal report (*Schulz and Jobmann*, 1989).

The rock matrix thermal conductivity is considered to be isotropic, and the temperature dependence is taken into account using an analytical equation in *Zoth and Hänel* (1988).

Specific heat flow for the total model area is estimated at $94\,mWm^{-2}$ based on temperatures corrected for paleoclimate. Such a high value is typical of younger basins (*Beardsmore and Cull*, 2001). Because the average temperature gradient in the area is $0.043\,K$, Fourier's law:

$$q = -\lambda \cdot \nabla T, \tag{42}$$

yields a mean thermal conductivity of $\sim 2.2\,Wm^{-1}K^{-1}$ (ignoring internal heat sources), which is reasonable for the rocks in question.

The mean surface temperature (top boundary condition) was determined from a linear extrapolation of the continuous log temperatures to the surface and a lateral interpolation.

These estimated values of the thermal properties were used in a coarse inversion model computed with the code presented by *Rath et al.* (2006). The resulting parameter estimates

Table 5: The thermal model properties. λ always at $20°C$. The heat-production H is estimated based on measurements and values in *Ondrak et al.* (1998).

No.	Key	Stratigraphic Unit	ϕ (-)	λ ($W\,m^{-1}K^{-1}$)	ρc ($MJ\,m^{-3}\,K^{-1}$)	H ($W\,m^{-3}$)
1	Q	Quaternary	0.25	2.0	1.98	$1.0 \cdot 10^{-10}$
2	OSM	Tertiary: Upper Freshwater-Molasse (sandstone)	0.15	3.0	2.72	$1.2 \cdot 10^{-6}$
3	OMM1	Tertiary: Upper Marine Molasse (Baltringer Horizon, sandstone)	0.25	3.1	3.15	$1.2 \cdot 10^{-6}$
4	OMM2	Tertiary: Upper Marine Molasse (remaining units, sandstone)	0.15	3.1	3.15	$1.2 \cdot 10^{-6}$
5	USM	Tertiary: Lower Freshwater Molasse	0.18	3.0	2.90	$1.4 \cdot 10^{-6}$
6	JO1	Upper Jurassic (Malm ζ, ϵ, δ, karstified limestone)	0.02	3.0	2.20	$1.4 \cdot 10^{-6}$
7	JO2	Upper Jurassic (Malm γ, limestone)	0.02	3.0	2.20	$1.4 \cdot 10^{-6}$
8	JO3	Upper Jurassic (Malm β, α, limestone)	0.02	3.0	2.20	$1.4 \cdot 10^{-6}$
9	JM	Middle Jurassic (Dogger, sandstone)	0.02	2.6	2.17	$1.4 \cdot 10^{-6}$
10	JU	Lower Jurassic (Lias, claystone)	0.20	2.3	1.59	$1.4 \cdot 10^{-6}$
11	TO	Upper Triassic (Keuper)	0.03	2.3	2.38	$3.0 \cdot 10^{-7}$
12	TM	Middle Triassic (Muschelkalk)	0.02	2.3	2.38	$3.0 \cdot 10^{-7}$
13	TU	Lower Triassic (Buntsandstein)	0.03	2.3	2.38	$1.0 \cdot 10^{-6}$
14	PC	Permo-Carboniferous	0.01	2.9	2.26	$1.5 \cdot 10^{-6}$
15	PCB	Palaeozoicum – Precambrian / Crystalline	0.01	3.5	2.50	$1.5 \cdot 10^{-6}$

were used for a forward model with a higher resolution and subsequently modified to obtain a better fit regarding calculated residual logs. The final properties are listed in Tab. 5. While some of the units have identical thermal parameter values, they are nonetheless separated due to their different hydraulic properties.

3.3.2 Results

After computing the quasi steady-state model, differences between the measured continuous logs and the model result were calculated and displayed for analytical purposes (Fig. 18 and 19). The model clearly fails to achieve a good fit. However, an approximately equal number of residual differences is positive and negative. This was achieved mainly by adjusting the basal specific heat flow. Most of the logs show a maximum difference of $\pm 2\,K$. In contrast the logs from geothermal exploration wells, in particular (Bad-Buchau, Saulgau, Fronhofen, Illmensee), show a significantly large positive difference, while Oberschwarzach and Gaisbeuren show a negative difference. At Gaisbeuren and Bad-Waldsee-1a, a negative residuum occurs within the Baltringer Horizon/Upper-OMM, and at Bad-Waldsee-Gb2, also a negative residuum occurs in the upper part of the Malm. Some logs also have a positive signature exactly at the depth of the karstified part of the Malm (clearly at

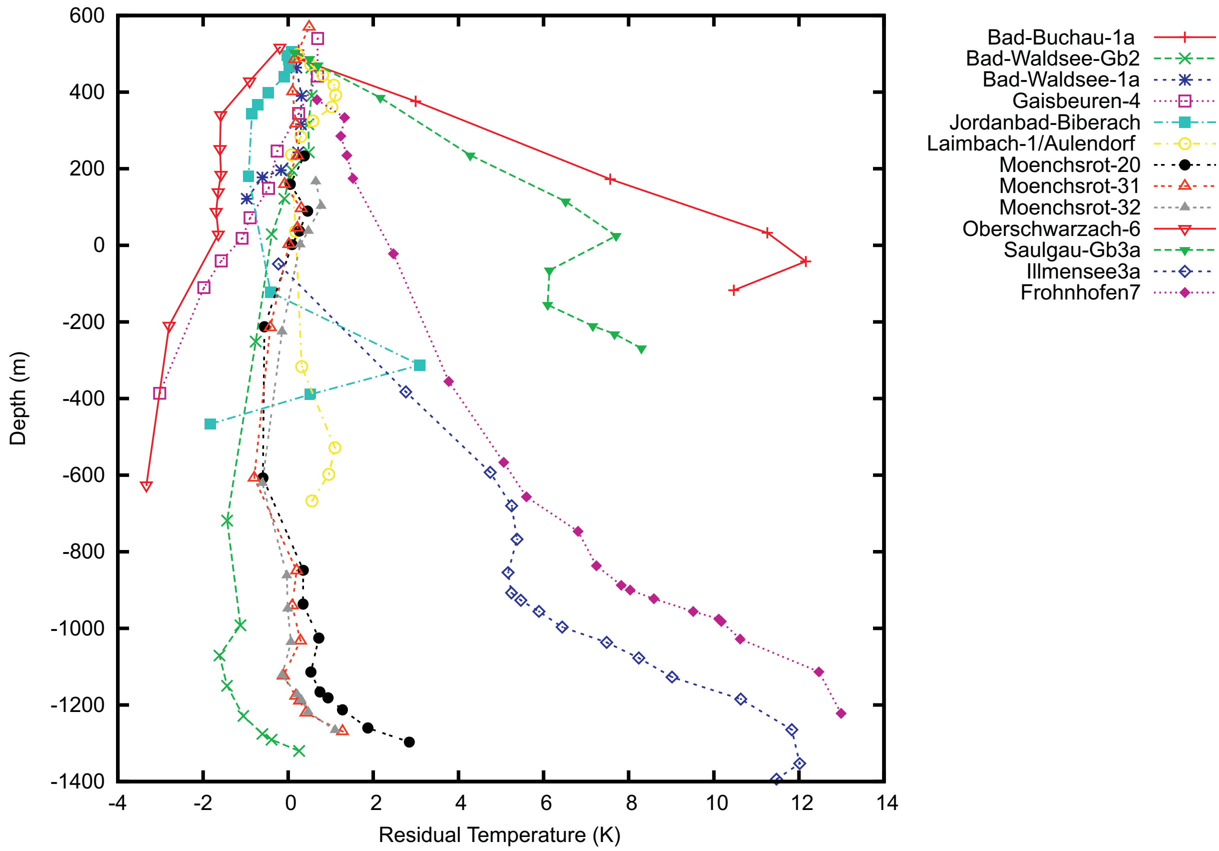

Figure 18: Residual logs, showing the difference between modeled and measured temperatures (position of logs: see Fig. 1)

Jordanbad-Biberach, Saulgau-Gb3a). It is obvious that advective processes have an impact here, therefore a perfect fit by a purely conductive model is not possible.

Subsequently, the residual temperatures (measured minus modeled data) were interpolated in three dimension using the code of *Rühaak* (2006). Fig. 20 shows the interpolated result for depths of 300 m, 200 m, 100 m and 0 m below sea level. There is an obvious correlation between the calculated temperature residuals and the major regional faults and also with the area where the Malm intersects the cross section. Due to the poor quality of some of the temperature measurements only areas with undisturbed logs or a large number of measurements will be discussed.

The histograms in Fig. 21 show that residual temperatures calculated by including BHT have a large scatter. This has two different reasons: (1) the low quality of BHT – the slightly bimodal distribution is probably due to the different corrections which have been applied to the original data (see Tab. 3), (2) even more important, BHT have a much larger

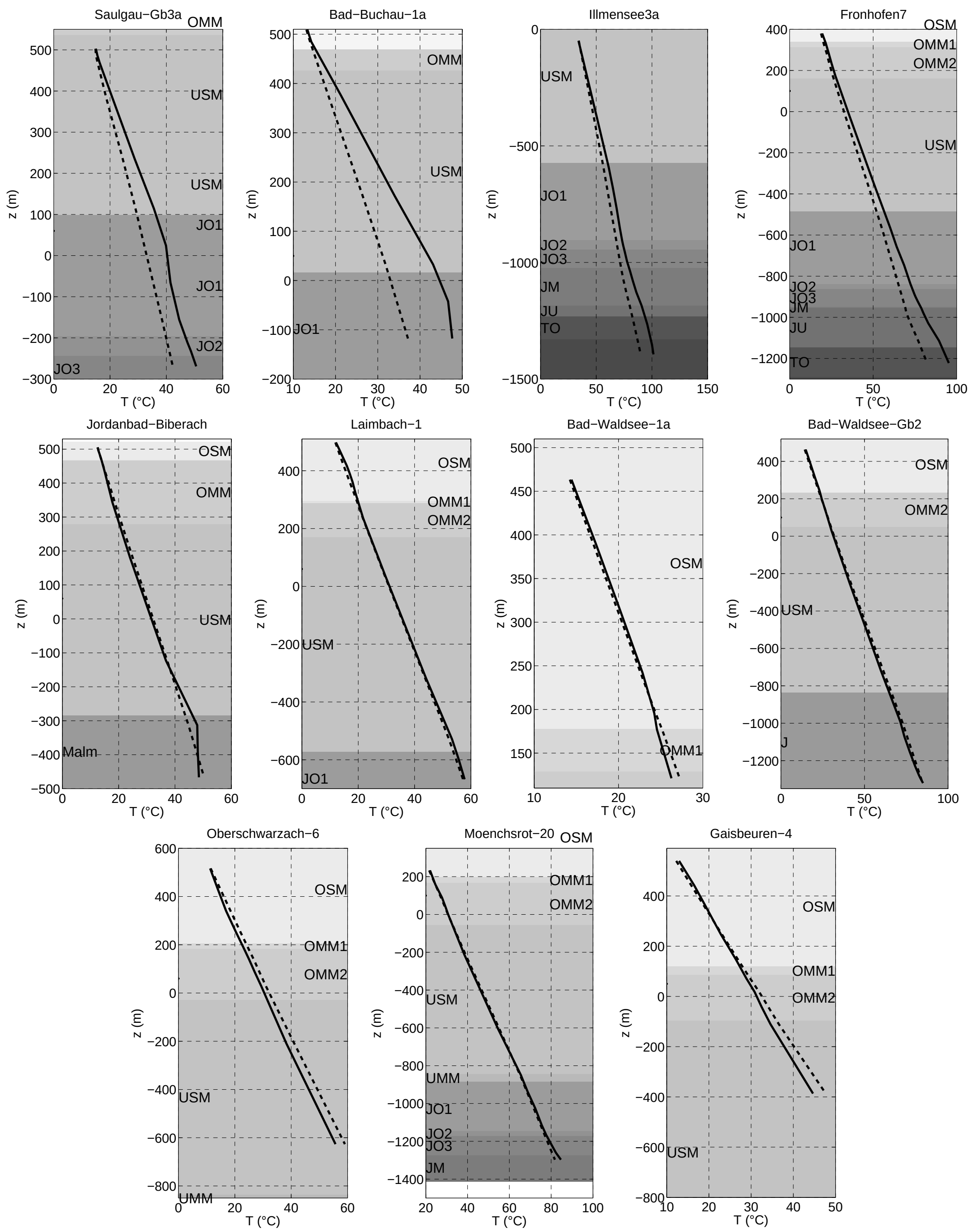

Figure 19: Comparison of the measured (straight line) and modeled (dashed line) log temperatures. The stratigraphy is also shown (compare Tab. 5). The position of the logs is shown in Fig. 1.

spatial, especially lateral distribution than all other temperature data. Fig. 21 also shows that unlike the residual logs (Fig. 21, left), which are slightly left-skewed, the distribution of the BHT (Fig. 21, right) is more symmetrical. This indicates a temperature regime which is more or less balanced in this area.

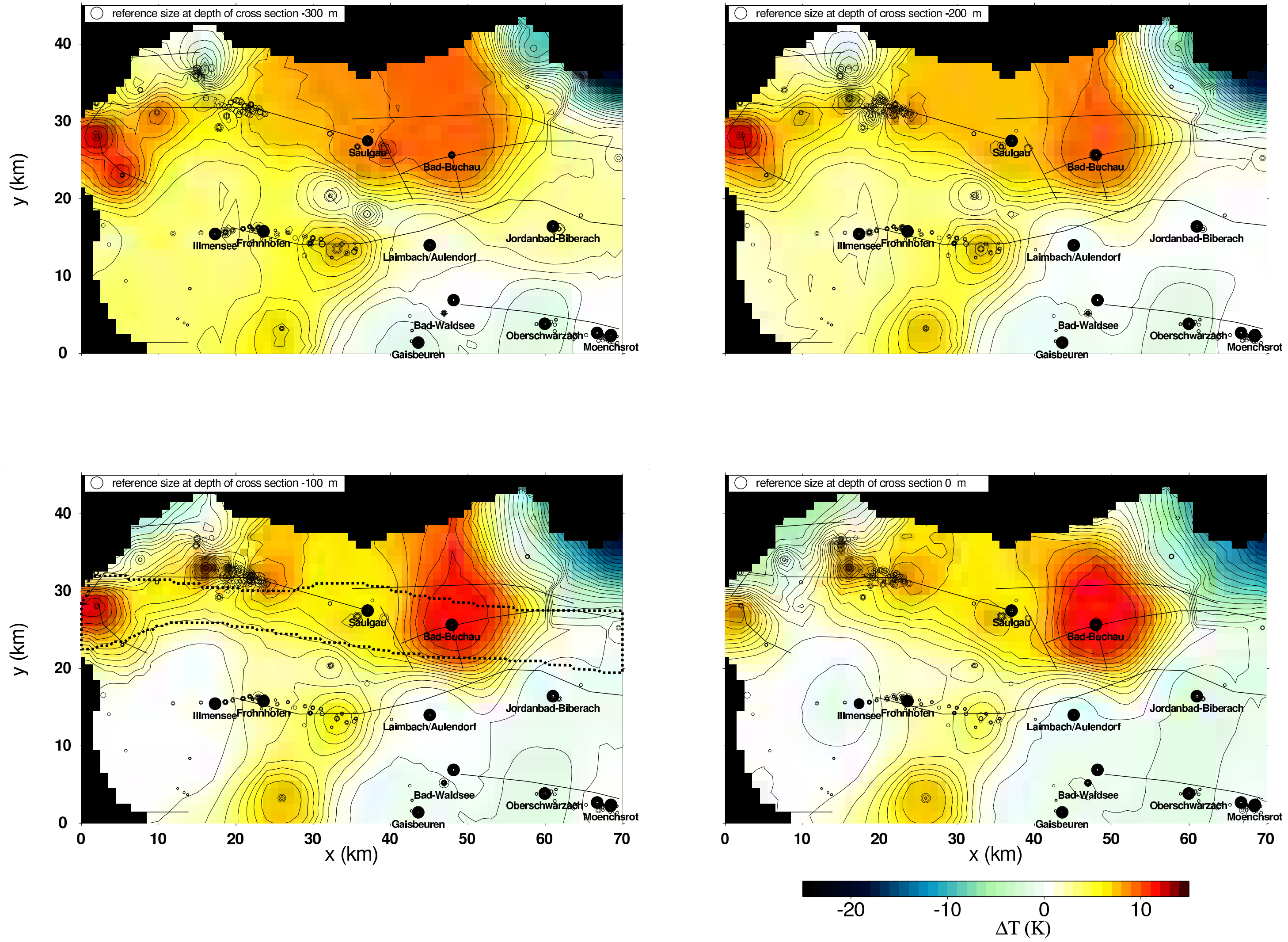

Figure 20: Residual temperature (measured minus simulated). The locations are corresponding to Fig. 17. From top left to bottom right cross sections at 300 m, 200 m, 100 m and 0 m below sea level (SL), which corresponds to about 900 m to 600 m below surface. Black circles show locations with temperature data, with circle size proportional to the vertical distance from this layer. The major faults shown (black lines) are derived from different sources. In the plot for 100 m below SL (lower left), the intersection of the Malm aquifer with the cross section is also marked with a dashed black line.

Fig. 22 shows the strata-bound residual temperatures within the Baltringer Horizon (Upper Marine Molasse - OMM1) and the top of the Upper Jurassic (JO1). Pure interpolation artifacts are mainly visible within OMM1, but no significant temperature anomalies. In contrast, significant temperature anomalies are visible in JO1, generally close to faults (especially at Saulgau, Bad-Buchau, and between Frohnhofen and Laimbach).

It would have been possible to obtain a better fit, especially regarding the continuous logs: for instance, a horizontal variation of the basal specific heat flow would improve the fit substantially. However, since the "true" specific heat flow is unknown, as is its horizontal variation, this would not yield any improvement of the overall result.

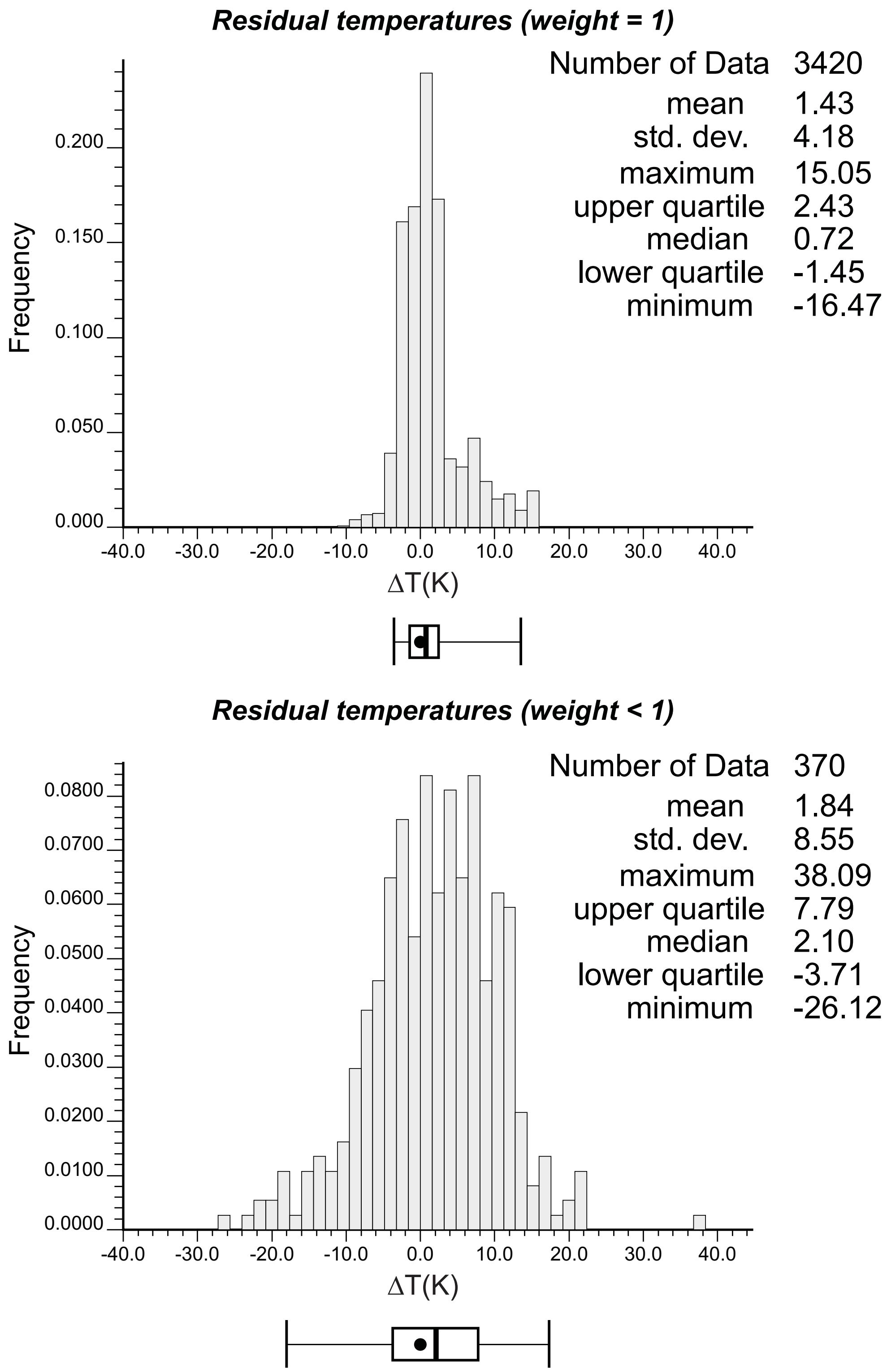

Figure 21: Histogram and box plot of residual temperatures: undisturbed logs only (top), BHT only (bottom). The box plot shows outside whiskers at the 95 % probability interval, inside box at the 50 % probability interval, vertical solid line at the median, and black dot at the reference value of zero (*Deutsch and Journel*, 1998).

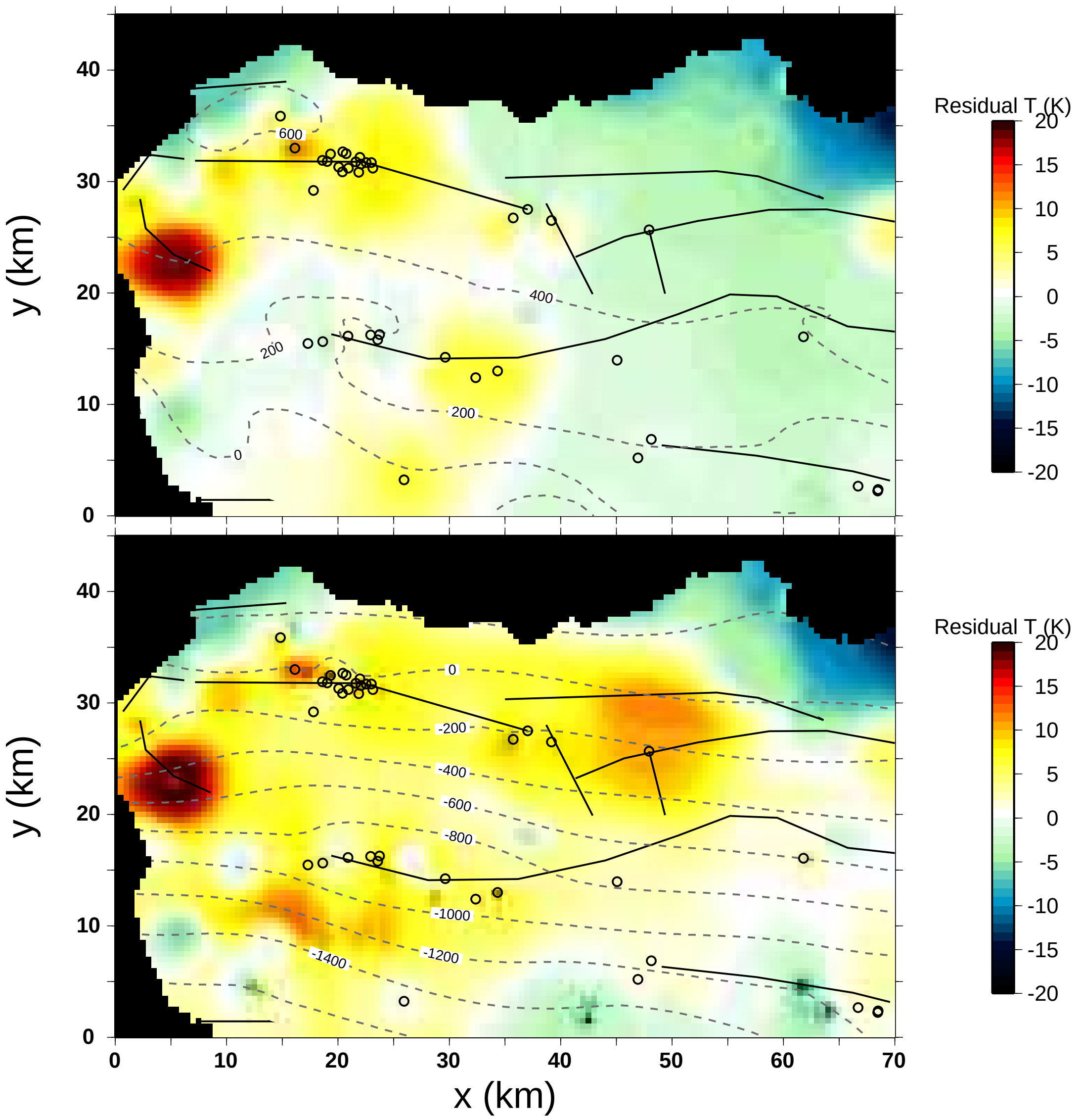

Figure 22: Strata-bound residual temperature (measured minus simulated). Top Baltringer Horizon (Upper Marine Molasse - OMM1), bottom Upper Jurassic (JO1). The major faults are shown (positions derived from different sources). Data locations within a horizontal radius of 1000 m and a vertical radius of 100 m are indicated by black circles. The depth below sea level is shown as dashed gray lines. The location is corresponding to Fig. 17.

3.4 Advective heat transport

The results of the conductive model demonstrate that there is significant heat transport associated with groundwater movement in some localities and at some depths in the model area. The following discusses different mechanisms for this advective heat transport, ruling out less probable explanations.

3.4.1 Flow regime

Some studies analyzed the flow regime in the Molasse Basin, for instance *Bertleff and Watzel* (1998) and *Bertleff and Watzel* (2002). The most relevant deeper regional aquifers in the model area are the Baltringer Horizon which is a sandstone at the top of the Tertiary OMM unit, and the Malm units ζ, ϵ and δ, which are karstified Upper Jurassic limestones. Due to tectonically induced vertical pressure head differences, the Malm aquifer probably has a large vertical leakage component (*Bertleff and Watzel*, 1998). The Malm aquifer is only relevant in the northern part of the basin (Swabian facies), because it is far less permeable in the southern part (Helvetic facies). This boundary is also shown in Fig. 1 (marked as 'Border Helv.'). The presumed groundwater head is shown in Fig. 23. Other potential aquifers in this area are the upper section of the Middle Triassic (Upper Muschelkalk), and possibly the Middle Jurassic (Dogger).

Regarding the advective heat transport component it is obvious that within the Malm aquifer mainly colder groundwater would infiltrate the deeper regions of the basin. For the Baltringer Horizon the situation is nearly identical.

It is possible to quantify vertical flow rates from geothermal data (see *Stallman*, 1963; *Bredehoeft and Papadopulos*, 1965; *Domenico and Palciauskas*, 1973; *Clauser*, 1999). However, the major component of groundwater movement is horizontal. Work attempting to quantify this horizontal component (e.g. *Zschocke et al.*, 2005) is only applicable at borehole constellations which occur only rarely and in a small part of the southeastern corner of the study area, within the Lower Marine Molasse (Baustein beds). Therefore, general quantitative information cannot be obtained based on thermal data alone.

3.4.2 Thermal convection

Free convection can arise spontaneously from density differences due to, e.g. thermal gradients in a basin. When cool fluids overlie warmer fluids, the system will convect freely given sufficient permeability and aquifer thickness (*Bethke*, 1989). The occurrence

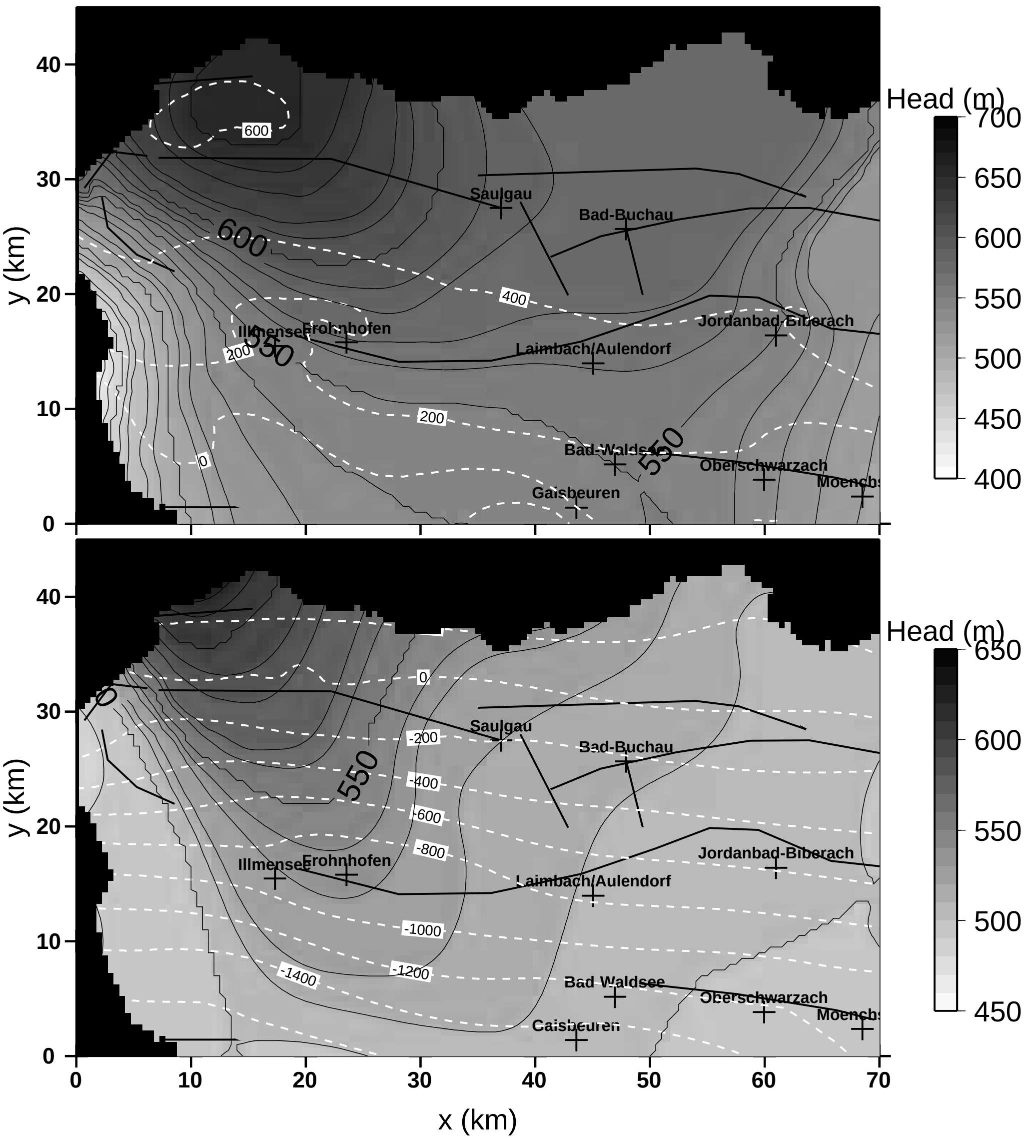

Figure 23: Presumed groundwater head in the model area (contour line interval is 10 m), based on *Bertleff et al.* (1988, 1993); *Bertleff and Watzel* (1998, 2002). The locations are corresponding to Fig. 17. Top: base of the Baltringer Horizon; Bottom: base of the Malm ζ, ϵ, δ. The depth below surface is shown as a white dashed line, faults as black lines, and the locations of continuous temperature logs as crosses.

of thermally driven free convection can be quantified by the dimensionless Rayleigh number (Ra). For a homogenous layer with a constant temperature difference between the upper and lower boundary it is defined by (e.g. *Powers and O'Neill*, 1986):

$$Ra = \frac{\rho_f g \alpha_f k L \Delta T}{\mu_f a}, \tag{43}$$

where $\alpha_f\,(K^{-1})$ is the thermal expansion coefficient of the fluid, $L\,(m)$ the vertical scale length and $\Delta T\,(K)$ the temperature difference between bottom and top. Thermal diffusivity a is defined as:

$$a = \frac{\lambda}{(\rho c)_f}. \tag{44}$$

Although Ra gives a first estimate for the relationship between advective and conductive heat transport, it is limited to an idealized configuration which determines the impact of the different parameters (*Bear and Bachmat*, 1991). The critical value for the onset of free convection in an ideal homogenous and horizontal layer is $4\pi^2$. However, no critical value - specifying the transition into a convective regime - can be determined for inclined layers (e.g. *Davis et al.*, 1985; *Phillips*, 1991). Eq. 43 shows that the occurrence and magnitude of free convection depends primarily on permeability, temperature difference, and geometry. The permeability distribution in deep aquifers, in particular, is generally unknown. Small heterogeneities - for instance due to clay layers - may influence the flow regime strongly. Within the area discussed here, three types of thermal convection are possible:

(1) strata-bound convection within highly permeable sub-horizontal sedimentary layers (e.g. *Pestov*, 2000); (2) convection within vertical structures like fault zones and fracture zones (e.g. *Bächler et al.*, 2003; *López and Smith*, 1995, 1996); (3) convection influenced both by strata-bound and vertical structures - interacting due to channeling and hydraulic short-circuits.

If forced convection occurs the flow is driven by an external potential gradient. In the study area, topographically-driven flow induced from higher parts of the Alps could be one option. Hot water could be driven from deep to shallow parts - along fault zones or strata-bound (e.g. *Person et al.*, 1996) - within the inclined layers. *Raffensperger and Vlassopoulos* (1999), among others, describe an example of the coexistence of both processes. However, isotope analysis clearly indicates that there is no groundwater exchange between the southern (Pliocene) and northern (Pleistocene) part of the Malm aquifer (*Bertleff and Watzel*, 1998). It is also presumed that the groundwater in the deeper parts is saline and stagnant (*Huber*, 1999, 2002), especially because the hydraulic conductivity is small in the southern (Helvetian) area, and there is no evidence for open karst systems.

To estimate the impact of heat transport due to forced convection, the dimensionless Péclet number (Pe^{2D}) was calculated for the two main aquifers (following *Bachu*, 1999, 1988):

$$Pe^{2D} = \frac{(\rho c)_f v L}{\lambda} \cdot \frac{\nabla_h T}{\nabla_v T}. \tag{45}$$

$v\,(m\,s^{-1})$ is the Darcy velocity and $L\,(m)$ is the typical vertical transport distance (set equal to the thickness of the aquifer). The subscripts h and v indicate the horizontal and vertical component of the temperature gradient $\nabla T\,(K\,m^{-1})$. The transition between predominantly diffusive and predominantly advective heat transport occurs between $0.1 < Pe \leq 1.0$.

Based on the isopotential (head) maps (Fig. 23), the 2D-Péclet number of the total area was calculated for the Baltringer Horizon (OMM1) and the Malm (JO1). The permeability of OMM1 is estimated at $k = 1.6 \cdot 10^{-12}\,m^2$ based on laboratory measurements. The porosity is estimated at $\phi = 0.25$. The free porosity of the JO1 aquifer is estimated at $\phi = 0.01 - 0.03$ (*Bertleff and Watzel*, 2002; *Rath and Clauser*, 2005). The literature data are very variable, in general. Especially as the Malm limestones are partially karstified. The permeability distribution is divided into a northern area close to the basin edge with high transmissivities of $T = 3.8 \cdot 10^{-3}\,m^2s^{-1} - 5.4 \cdot 10^{-3}\,m^2s^{-1}$, and a southern area in the basin center with considerably lower transmissivities of $T = 1.2 \cdot 10^{-4}\,m^2s^{-1} - 6.4 \cdot 10^{-4}\,m^2s^{-1}$ (*Bertleff and Watzel*, 2002). Based on the calculated pressure and temperature regime and an aquifer thickness of 60 m, the resulting maximum average permeability is $k = 4.4 \cdot 10^{-12}\,m^2$.

In addition to the head, the other two important parameters are depth to base and thickness. Both are inferred from the structural model. However, with regard to the Malm ζ, ϵ, δ aquifer, only the top is karstified. The net thickness of the actual Malm aquifer is between $20\,m - 60\,m$ (*Bertleff et al.*, 1993). Therefore, a constant thickness of $60\,m$ is used for the calculations.

The temperature gradient (Fig. 24) was calculated using a 3D-interpolation of the measured temperatures. Using this temperature, ρ and c were calculated as functions of pressure and temperature using a code based on *Wagner and Overhoff* (2006). Because the real mean permeability of the total area is unknown, the calculations are based on the maximum values discussed above in order to estimate the expected maximum effect. Bulk thermal conductivity was assigned according to Tab. 5.

The calculated 2D-Péclet number in both aquifers is generally smaller than 0.1, mostly $Pe^{2D} \ll 0.01$. This shows that no significant heat distribution can be expected from strata-bound groundwater flow.

Similarly, the local Rayleigh number (Eq. 43) was calculated. For this purpose the thermal expansion coefficient α and the dynamic viscosity μ of the water were also calculated as functions of pressure and temperature, in contrast to e.g. *Pestov* (2000) who used values for the fluid properties at reference temperature and pressure. Because of the large variability of many physical properties with pressure and temperature, fluid and rock properties should be evaluated at in situ conditions. For instance, in case of the JO1, at an approximately depth of $1000\,m$ below the surface the temperature is $\approx 30\,K$ higher than at reference conditions, therefore - assuming a hydrostatic regime - dynamic viscosity is 1.8 times smaller than at reference conditions, fluid thermal conductivity is about 8% higher, the thermal expansion coefficient is less than half, the density decreases by $5.85\,kg\,m^{-3}$ (about 0.6%). While rock thermal conductivity of $2.5\,W\,m^{-1}\,K^{-1}$ decreases by about 5%. In the case studied here the calculated JO1 Rayleigh number would be two times smaller if values at reference condition would be used.

Based on the limited information on structure and permeability, Ra only exceeds the critical value of $Ra_c \sim 40$ in the Baltringer Horizon in very small parts in the south of the study area. The area in the Malm aquifer exceeding the critical value is larger (see Fig. 25) and the Ra values are also much higher in some parts (up to 130).

The presence of free convection depends on a number of factors (e.g. anisotropy or lateral permeability variation). Based on the rare structural information on the karstified dolomite in the study area (e.g. *Bertleff and Watzel*, 1998), it is not possible to come to a final conclusion. Furthermore, other types such as vertical convection cells are not discussed. For instance, *Kiraly* (2002) and *Kovács* (2003) demonstrate the complexity of karstified aquifers. Flow simulations, in particular, are still challenging.

3.5 An alternative explanation for the major anomalies

An alternative scenario which may explain the thermal anomalies is a vertical, fault channeled upflow of hot water. No other model constellation can generate significant anomalies at the correct locations. This leads to the hypothesis that the thermal anomalies detected around Saulgau and Bad-Buchau are a combined effect of flow within the highly permeable Malm aquifer intersecting a highly permeable vertical fault zone. The cold groundwater

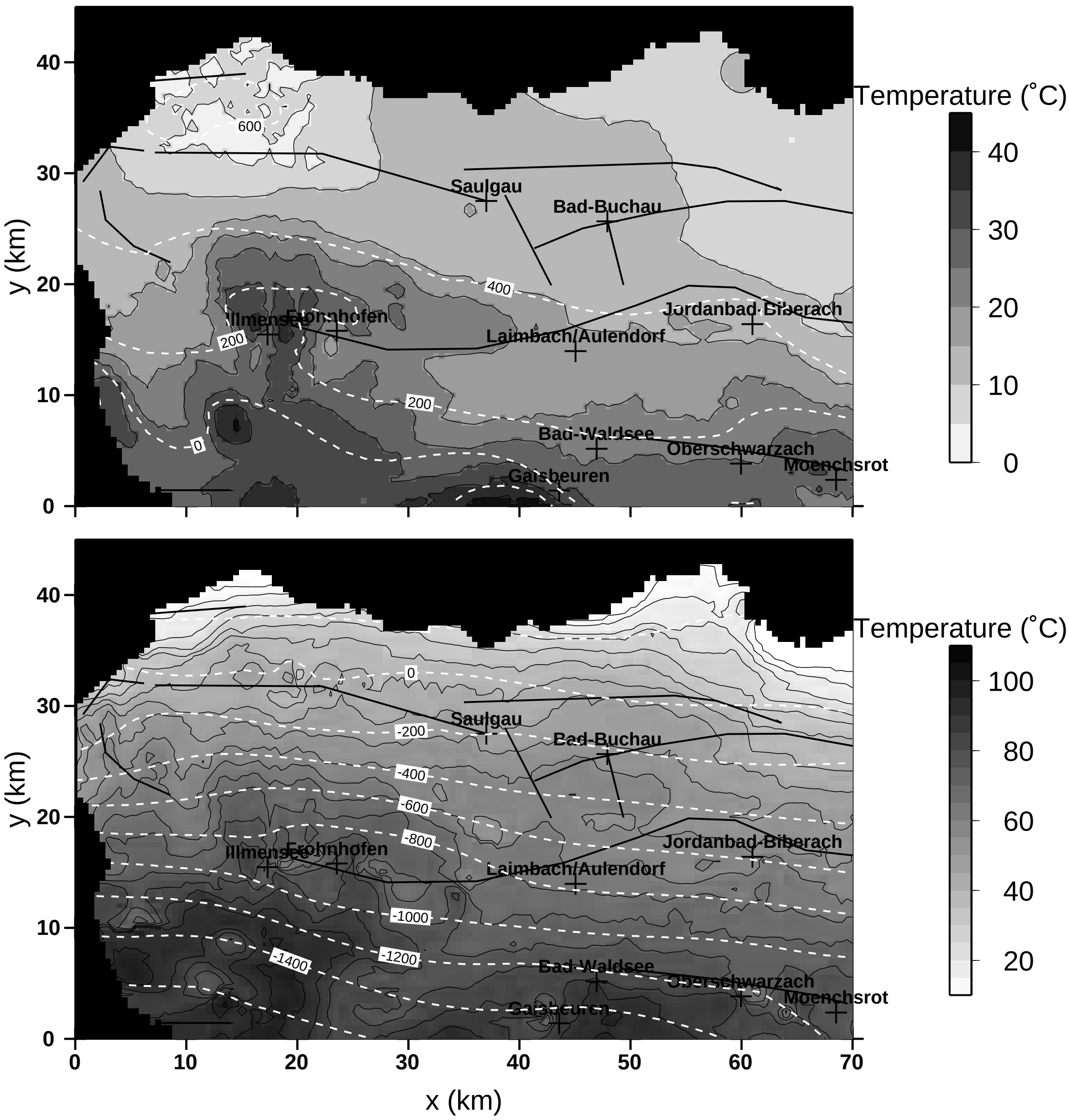

Figure 24: Temperature at the base of the Baltringer Horizon (top) and of the Upper Jurassic Malm-δ (bottom). The depth below sea level is shown as dashed white lines. The location is corresponding to Fig. 17.

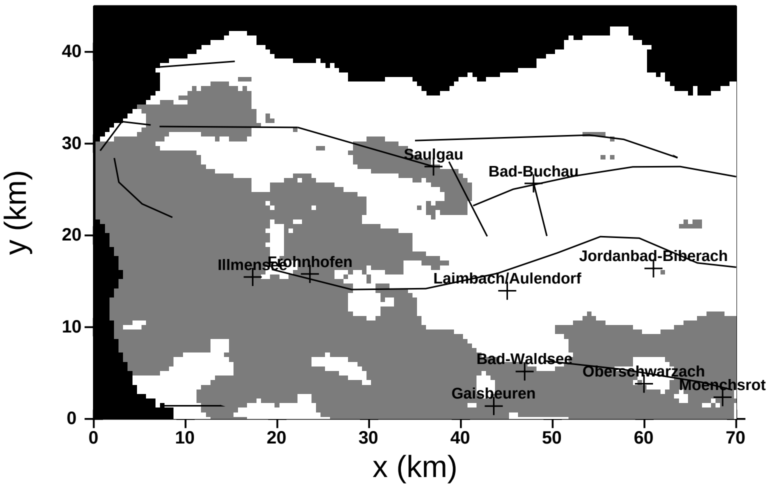

Figure 25: Rayleigh number in the Upper Jurassic Malm ζ, ϵ, δ: white area $Ra < 40$, gray shading $Ra \geq 40$. The location is corresponding to Fig. 17.

in the Malm aquifer flows to the East parallel to the northern basin margin at a relatively high Darcy velocity of about $2\,m\,a^{-1}$ (*Bertleff et al.*, 1993; *Bertleff and Watzel*, 1998). Free convection could occur within the fault zone inducing convection cells which transport hot groundwater ($> 10\,K$ above ambient) into shallower regions. Permeable, continuous fault zones may strongly influence both basin-scale fluid flow and the subsurface thermal regime (*Smith et al.*, 1990). Even fractures with apertures as narrow as a few millimeters permit significant hot water flows to the surface from depths of more than one kilometer (*Lowell*, 1975). A review by *Fairley et al.* (2003) concludes that, despite its importance, fluid flow in faults is still poorly understood.

Faults have been shown to act as barriers to subsurface fluid flow, or as conduits, or a combination of both (*Fairley and Hinds*, 2004). *Murphy* (1979) discussed the occurrence and temperature distribution of convection within vertical faults. An overview of the interaction between faults and groundwater movement is given by *Bense and Person* (2006) and *Smith et al.* (1990). *Simms and Garven* (2004) studied the impact of fault zones on basin-scale convection systems, whereas e.g. *Eichhubl and Boles* (2000) and *Bächler et al.* (2003) studied the impact of groundwater flow focused by faults. *Bense and Kooi* (2004) studied the effect of faults in unconsolidated sediments on groundwater flow and the subsurface temperature distribution. All these studies are generally in line with my hypothesis.

One of the main thermal anomalies is located at the Saulgau fault zone, which is associated with an active earthquake region. Earlier, the fault had been classified as a normal fault, contradicting the NE striking sinistral strike-slip character inferred from earthquake seismology (*Stange and Brüstle*, 2003).

The WSW–ENE striking faults (Fig. 1) were mostly created before the Tertiary, while the N–S faults originate from the Quaternary (*Freudenberger and Schwerd*, 1996).

A genetic connection between this fault zone and the observed thermal anomaly has not been demonstrated so far.

The exact location and structure of the fault zones in the model area is largely unknown, because they have not been active recently, and are therefore covered by Quaternary sediments. It is generally unknown whether the faults within the model area are hydraulically conductive. This seems unlikely though, based on the information on tectonics and stress directions (see Fig. 26): The approximately N–S directed tectonic main stress directions should result in a compressive, reverse fault, and hence a low-permeability fault. However, this information characterizes the lower crust. In contrast, due to isostasy and related to the recent tectonic movements, a N-S directed stress minimum in shallow parts might also be possible (for details see e.g. *Zweigel*, 1998). One important evidence of this hypothesis is the fact that numerous springs are located on WSW–ENE striking faults (see Fig. 1).

Another information is related to the fact that much temperature data derive from oil exploration wells which were deliberately targeted at the fault zones looking for fault displacement oil or gas traps. The temperatures are therefore biased by a cluster effect. Nonetheless, temperature measurements outside fault zones clearly confirm the importance of the fault zones for the regional temperature distribution.

3.5.1 A type model

A numerical type model was set up reflecting the main factors in order to test the possibility that the thermal anomalies are caused by advective heat transport due to a combined flow in the Malm aquifer and the fault zones.

The model dimensions are $10\,km \times 2.4\,km \times 4.6\,km$. The grid size is 20 m in x-direction (500 nodes); in y-direction the grid is non-equidistant with a size of: 1000 m - 105 m - 50 m - 25 m - 15 m - 10 m - 15 m - 25 m - 50 m -105 m - 1000 m (11 nodes). In z-direction the grid size is 25 m (184 nodes). The model has 4 different layers, with hydraulic and thermal parameters shown in Tab. 6.

In a simplified manner, Layer 1 represents the tertiary units, Layer 2 the Malm aquifer, Layer 3 all Mesozoic and Palaeozoic units below the Malm aquifer and above the crystalline basement which is represented by Layer 4. The depth of these layers is roughly the same as

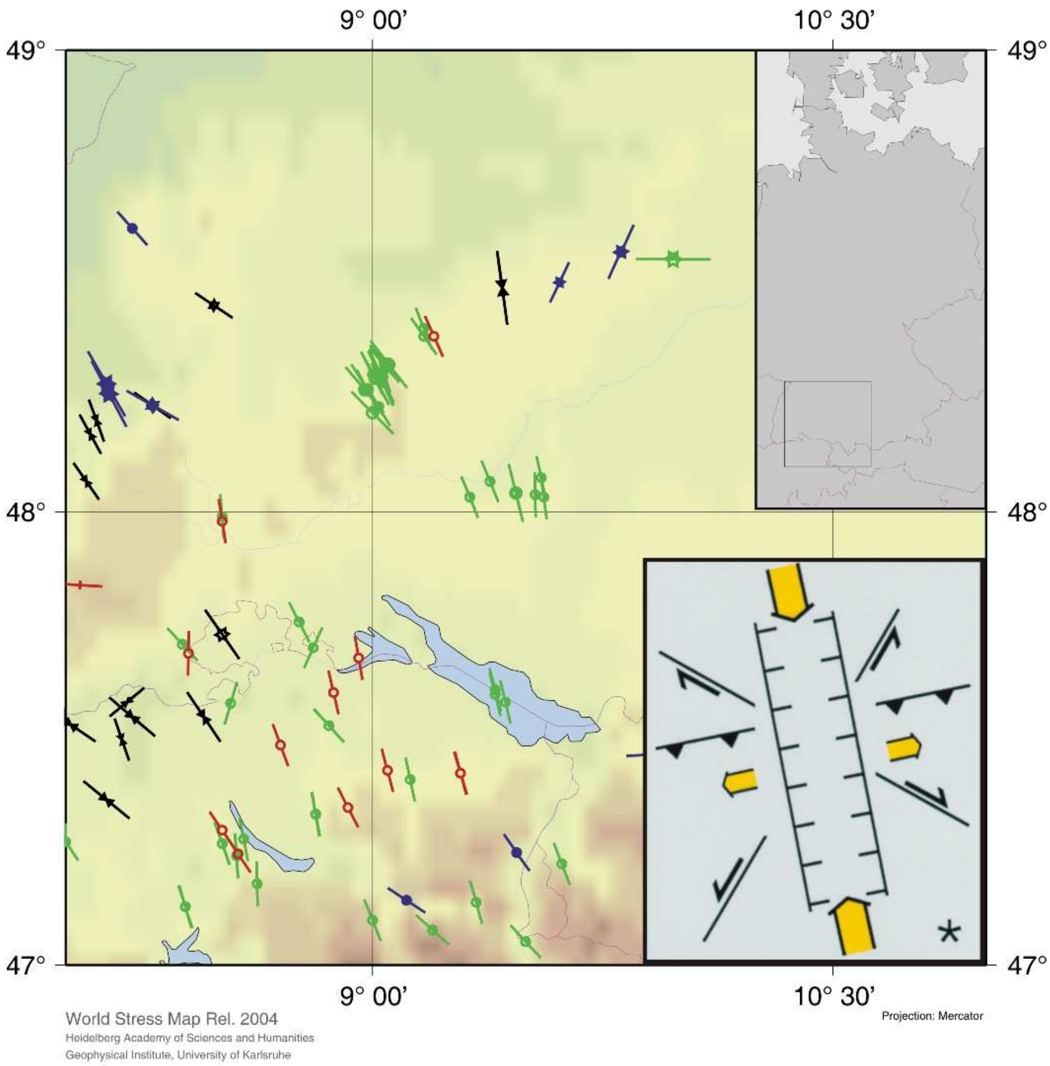

Figure 26: Tectonics of the Molasse Basin. Left: Main regional tectonic directions of the Alpine region (*Reinecker et al.*, 2005). Right: Schematic diagram of the main tectonic stress directions of the region, yielding a combination of thrust, normal and strike-slip faults (*Anonymous*, 2002).

Table 6: Hydraulic and thermal parameters of the type model.

Layer (-)	ϕ (-)	k (m^2)	ρc ($MJ\,m^{-3}\,K^{-1}$)	λ ($W\,m^{-1}\,K^{-1}$)
1	0.200	10^{-16}	3.2	2.87
2	0.025	10^{-12}	2.2	3.00
3	0.100	10^{-18}	2.3	2.90
4	0.100	10^{-22}	2.5	3.50

is found near Saulgau and Bad-Buchau. As the model area is quite small, it is permissible to assume a horizontal position of the relevant layers, as the dip, in general, is small (see Fig. 17). As mentioned before, the actual hydraulic properties of the units are more or less unknown. They are therefore chosen at typical values for a basin (see e.g. *Nunn et al.*, 1999).

The fault zone is positioned in the center of the model and with a thickness of 10 m, a permeability $k = 1.5 \cdot 10^{-12}\,m^2$, porosity $\phi = 0.4$, volumetric specific heat $\rho c = 2.5\,(MJ\,m^{-3}\,K^{-1})$, thermal conductivity $\lambda = 1.0\,(W\,m^{-1}\,K^{-1})$. Permeability decreases slightly with depth within all units and the fault zone following *Allen and Allen* (1990).

The fault zone is finite: the first 500 m at the western and the last 500 m at the eastern border are dedicated to the surrounding units (see Fig. 27).

To induce groundwater flow in an easterly direction (see Fig. 23) a pressure boundary condition is specified for the left and right boundary, resulting in a head gradient of $5 \cdot 10^{-3}$. The thermal boundary conditions at the top and the bottom are fixed temperatures of $10\,°C$ and $148\,°C$ respectively.

Simulations are performed in transient mode. The time steps are increased exponentially, e.g.: first period ends at $10^2\,s$, with a time step size of $10^1\,s$, the second period with $10^3\,s$, time step is $10^2\,s$, and so on. This kind of time stepping proved to yield stable results, while progressing relatively fast. The final result is obtained after $10^{15}\,s$ (about 32 Ma). The total time is roughly on the order of the development of the real flow system, from mid Tertiary till today.

For the computation of this orthogonal model the original SHEMAT was used. A result of this calculation is shown in Fig. 28: The positive thermal anomaly's maximum is approximately $14\,K$. This is on the order of the observed anomalies. The type model indicates that the anomaly is associated with the end of the fault and the interplay with the relatively fast groundwater flow in the Malm aquifer. A model with a fault zone of only 1 m thickness yields the same flow field, however, with a substantially smaller residual temperature due to the ten times smaller volume flow rate.

If the groundwater velocity is small – realized by reducing the head gradient to one tenth of the previous value – an entirely different flow field arises (Fig. 29). Due to the occurrence of multiple convection cells, the maximum residual temperatures are lower and at entirely different positions.

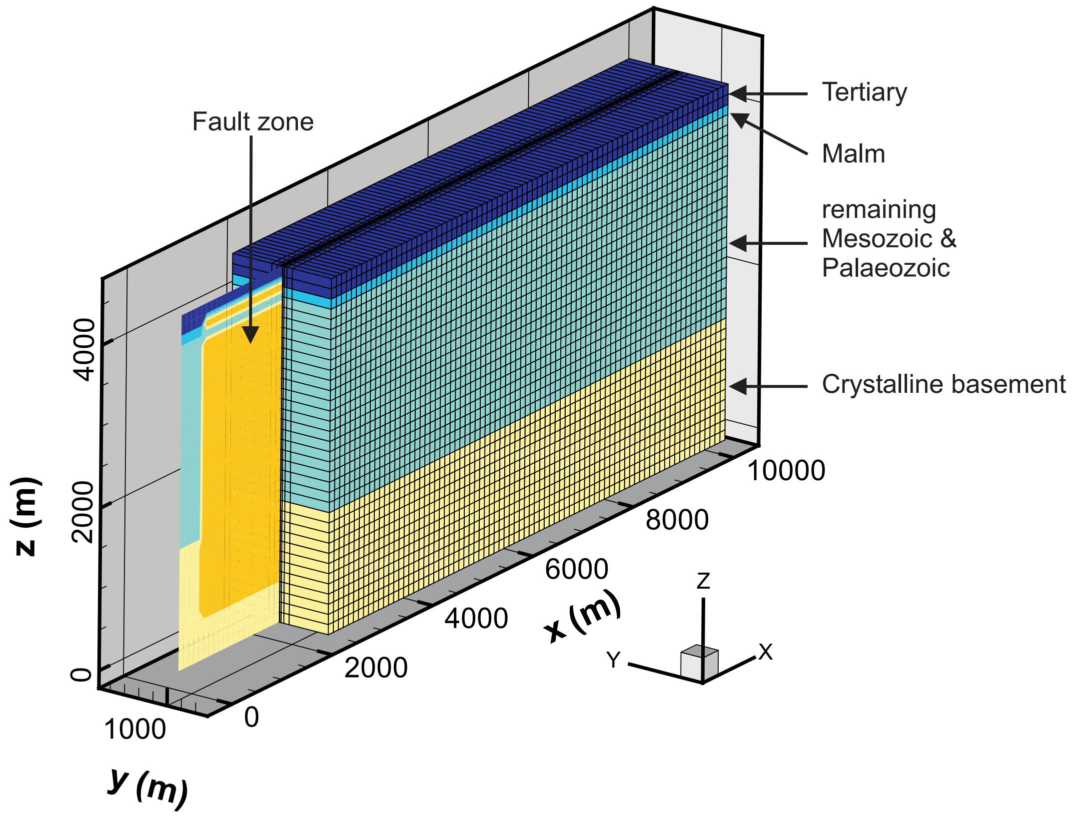

Figure 27: The type model grid with the different property zones. In the center (yellow) the fault zone is visible.

First tests of this type model have been computed using an older version of the FE software Rockflow (*Thorenz*, 2001; *Diersch and Kolditz*, 2002). The result obtained with this code was in general agreement with the one discussed here.

3.5.2 Discussion

The type models indicate that the observed thermal anomalies can be explained by the interaction of a relatively fast groundwater flow in the karst aquifer with free convection within the fault zones. In contrast to pure convection in faults, no system of multiple cells

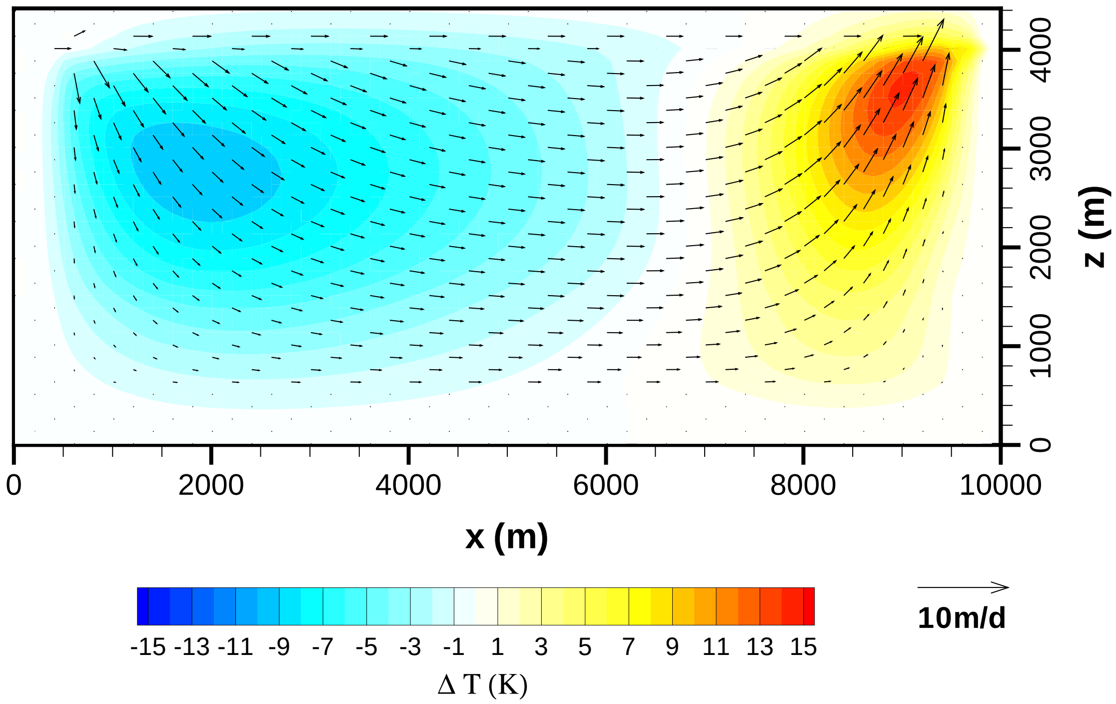

Figure 28: Temperature and flow field in a vertical cross section along the fault zone (see Fig. 27) after about 32 Ma. The temperature residuals are calculated relative to a purely conductive model. The vector arrows show the direction and magnitude of the Darcy velocity. The thermal anomaly is a result of superposition and interaction of the groundwater flow in the fault and the colder karst aquifer.

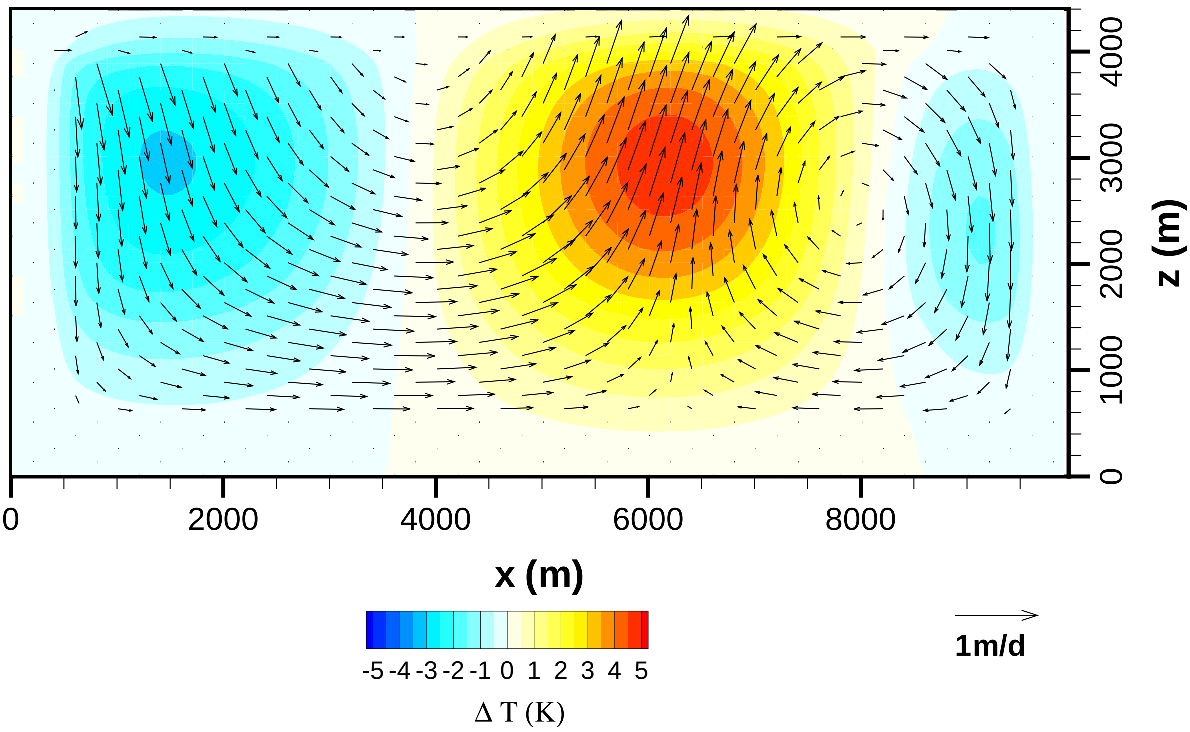

Figure 29: Temperature and flow field in a vertical cross section along the fault zone (see Fig. 27) after about 32 Ma. The temperature residuals are calculated relative to a purely conductive model. The vector arrows show the direction and magnitude of the Darcy velocity. However, in this case the permeability within the Malm aquifer (compare Fig. 27) is 10^4 times smaller than in Fig. 28.

develops due to the interplay with regional groundwater flow. Instead, there is only one large convection system which is superposed by the regional flow (Fig. 28). This combined flow system ends abruptly with a strong upflow at the end of the fault. This is exactly where the model produces the strongest positive thermal anomalies. This is in line with the field data which show the major positive thermal anomalies at positions where the prominent E–W faults intersect with N–S faults (simplified in Fig. 30). It is likely that the E–W striking faults are interrupted at these locations, as the N–S striking ones are more recent. Based on data no intersection is known at Pfullendorf. However, based on temperature data it seems likely that here a N–S oriented fault exists as well. The absence of negative thermal anomalies in real data is probably due to the focussed large regional flow volume coinciding with the small discharge region of the fault.

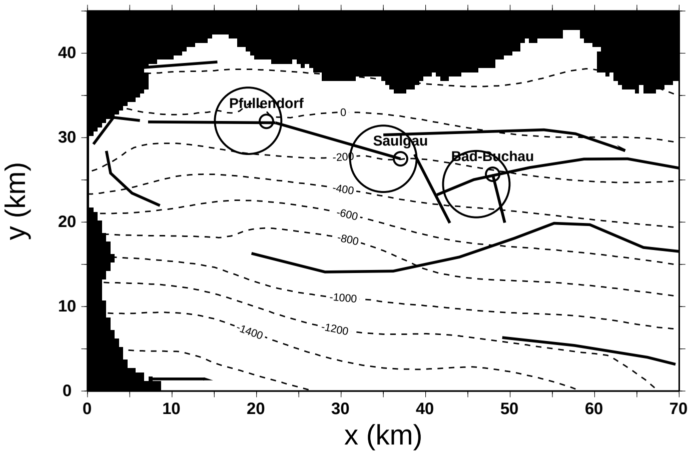

Figure 30: Sketch showing the vicinity of thermal anomalies (circles) and the points of intersection between N-S and E-W faults. The depth below sea level of the Malm aquifer is shown as dashed black lines.

All of the software applied describes the flow in the fault as laminar Darcy flow. The assumptions required for the Darcy approach are still valid, because this is a macroscopic fault zone rather than a system of discrete fractures. Furthermore, the necessary assumption of laminar flow is justifiable for the presented study: At the micro-scale, a system of interconnected pores is replaced by an equivalent continuum described by its hydraulic conductivity. At this scale and above, Darcy's law holds. Furthermore, an approach to model a fracture by an arrangement of parallel, conductive plates with a permeability according to the cubic law (*Snow*, 1965) cannot be applied because there is no information on fracture aperture or width.

3.6 Conclusions – modeling of the thermal regime in the western Molasse Basin

The flow regime of the western Molasse Basin has been studied with an emphasis on deep aquifers. Because of the sparseness of the hydraulic data, it is not possible to compute a fully coupled flow model. However, the comparatively large number of temperature measurements and additional thermal conductivity measurements supports calculating a purely conductive model. This quasi steady-state model displays major thermal anomalies. Although only qualitative information is available on advectively disturbed areas, it is possible to deduce the underlying processes by using additional information such as on the groundwater head.

The results of this study present for the first time an explanation for the main positive thermal anomalies within the western part of the Molasse Basin which are mostly located close to fault zones. It was shown by *Smith et al.* (1990) that models of fluid flow and heat transfer within faults must be placed in a regional hydrogeologic context. Analysis of the regional Rayleigh number showed that free thermal convection is possible within the Malm aquifer, but unlikely in this case due to the structure of this karstified dolomite. Analysis of the regional 2D-Péclet number showed that advective heat transport is not dominant within the two main aquifers. Considering all available information, it was possible to preclude all theoretical explanations for the main thermal anomalies along the faults with the exception of free convection within the faults, superposed by the regional flow regime flowing parallel to the faults. A numerical type model supports this theory by showing that the strongest positive thermal anomalies occur where fault zones end abruptly. This can also be assumed for the locations of the observed anomalies.

This result is particularly important for geothermal exploration because it shows a constellation which may support high temperatures at significantly shallower depths than normal. The conceptual approach of this study is promising for detecting subsurface regions heated above normal by groundwater driven heat advection. In general, the lack of data precludes the quantitative analysis of large and deep parts of this basin region. Therefore, this qualitative approach is a valuable tool. The result of this study may also assist the exploration of hydrothermal deposits.

Many special investigations may be performed within this part of the basin, for instance, thermal history; the relationship between tectonic processes and thermal fields; specific heat flow variation; fully coupled groundwater model; and more. Unfortunately, meaningful analysis is currently prevented by the present lack of data.

4 Discussion and outlook

This thesis demonstrates the potential of temperature data for conclusions with respect to the flow regime. Regarding the extremely sparse availability of relevant parameters for deep aquifers this is particularly valuable as temperature data are the only ones with a sufficiently good spatial distribution. However, as discussed, the quality of temperature data is often low depending on the type of measurements. In this thesis, a new method of quality weighting is applied which honors the different qualities during spatial interpolation which, for example, are necessary for a visual interpretation. Further research to improve the quality of BHT data would be an advantage. Even more important is the availability of continuous undisturbed logs - like the ones carried out by the GGA Institute (Hannover, Germany). Within the study area, there are only 13 logs with a sufficient depth. The measurement of more logs could improve the validity of this study. Locations of special importance are Pfullendorf, and midway between Pfullendorf and Saulgau (where no data exist at all). More data gaps can be easily identified in Fig. 1. Their filling in is highly desirable.

Additionally, the development of a new finite volume method is presented, based on a coordinate transformation capable of handling non-orthogonal grids. Non-orthogonal grids can be of great value for numerical basin modeling. However, in case of the purely conductive model presented here the additional geometric accuracy is not necessary although it makes the generation of the grid easier. If enough data exist for a coupled flow and heat transport model such a grid is much more important to obtain a valid result.

Inverse modeling can be of great value and has also been applied for initial studies in this thesis. However, inverse models are still not able to estimate the necessary parameters automatically. A serious problem with the code of *Rath et al.* (2006) (and probably with all others of this kind) is the tremendous amount of computational resources required. The computation on a sufficiently fine grid needs easily more than 10 Gigabyte of random access memory (RAM) and accordingly several days of calculation time on a present high-performance computer. Further on, the inverse solution of 'ill posed problems' (*Tarantola and Valette*, 1982), is always connected with ambiguity: different parameter combinations may yield the same solution. The best way to minimize these ambiguities is to include additional data.

Another field of increasing importance is the application of regionalization methods, especially geostatistical simulations (e.g *Patriarche et al.*, 2005). However, as stated already, in this case study hydraulic data are too sparse to apply such methods. This method could have been applied to thermal conductivity data here, but was not necessary due to the smooth and continuous distribution of conductive heat flow.

Numerical instabilities are still a serious problem for fully coupled heat transport calculations. Although high-performance computers exist today with the possibility to calculate extremely dense grids, the effort is big. Further on, notwithstanding the performance, in 3D a ten times finer grid still means an approximately 1000 times longer execution time. Considering a stability criterion like the Courant criterion (see e.g. *Clauser*, 2003) the computation of a transient large-scale model with an aquifer permeability of, say, $10^{10}\,m^2$ is nearly impossible due to the necessary small time steps. Of course, some approaches to overcome this shortcoming already exist, for instance the application of dimensionless numbers (e.g. *Bear and Bachmat*, 1991). However, a more general solution would be desirable.

Regarding the coordinate transformation method, a number of tasks are discussed for the future in Chapter 2.4. The most important point seems to be the development of an appropriate grid generator. This is also still a serious problem for FEM codes applied to arbitrary complex geometries which are typical for subsurface models. However, a promising method is the generation of grids directly from a *GOCAD®* geometrical subsurface models as presented here.

Acknowledgments

First of all, I would like to thank C. Clauser for supervision. I am also very grateful to H.-J. Kümpel for being my second supervisor.

This work was mainly carried out during different projects at the Leibniz Institute for Applied Geosciences (GGA) in Hannover. While completing it I have become a member of the Groundwater Modeling Center of DHI-WASY GmbH.

The work presented here was performed partially during a project funded by the German Federal Environmental Ministry as part of the activities of its AkEnd Working Group (http://www.akend.de) through Bundesamt für Strahlenschutz (BfS, Federal Agency for Radiation Protection) under contract 9X0009-8390 to RWTH Aachen University and 9X0009-8390-2 to Geophysica Beratungsgesellschaft mbH, Stolberg.

I thank the Geological Survey of Baden-Wurttemberg (LGRB, Freiburg) for providing information, data, and core material.

The Wirtschaftsverband Erdöl- und Erdgasgewinnung (WEG) kindly allowed to use material from their archives, which were supplied by the Erdölgeologischer Austausch (ATS) hosted at the Geological Survey of Lower Saxony (LBEG, Hannover).

Thermal conductivity measurements were made at the Applied Geophysics Department, RWTH Aachen University by A. Hartmann, F. Höhne and D. Breuer, and at the Leibnitz Institute for Applied Geosciences by H. Deetjen and R. Schellschmidt.

The paleoclimate software and the heat production estimates made by Andreas Hartmann were especially valuable for this work.

I thank Volker Rath for generously supporting the dissertation with his scientific expertise. Andreas Wolf helped me while developing the *sno* code.

For a very good scientific cooperation I thank the following GGA colleagues: Stefan Weßling, Jan Igel, Andrei Zschocke, Rüdiger Schellschmidt, Reinhard Jung, Winfried Kessels, Thomas Günther, Rüdiger Schulz, and all other colleagues from the $S5$ $'Baracke'$.

I want to thank Nicole Mölders who gave me the chance to start with my scientific work at the Institute for Meteorology at the University Leipzig. It helped at lot to have such friendly colleagues as Martin & Martin.

Further on I am thankful for manifold support to the following people: Manije, Timo, Michael & Barbara, Tanja & Giovanni, and, of course, my parents.

References

Allen, P. A., and J. R. Allen (1990), *Basin Analysis. Principles and Applications*, Blackwell Scientific, Oxford.

Andaverde, J., S. P. Verma, and E. Santoyo (2005), Uncertainty estimates of static formation temperatures in boreholes and evaluation of regression models, *Geophysical Journal International*, *160*(3), 1112–1122, doi:10.1111/j.1365-246X.2005.02543.x.

Anderson, J. D. (1995), *Computational Fluid Dynamics – The basics with applications*, McGraw-Hill, New York.

Anderson, M. P. (2005), Heat as a ground water tracer, *Ground Water*, *43*(6), 951–968, doi:10.1111/j.1745-6584.2005.00052.x.

Anderson, M. P., and W. W. Woessner (1992), *Applied Groundwater Modeling - Simulation of Flow and Advective Transport*, 1–381 pp., Academic Press, London.

Anonymous (2002), Projekt Opalinuston: Synthese der geowissenschaftlichen Untersuchungsergebnisse. Entsorgungsnachweis für abgebrannte Brennelemente, verglaste hochaktive sowie langlebige mittelaktive Abfälle, *Nagra Technischer Bericht (NTB) 02-03*, National Cooperative for the Disposal of Radioactive Waste - NAGRA, Wettingen, Switzerland.

Bächler, D., T. Kohl, and L. Rybach (2003), Impact of graben-parallel faults on hydrothermal convection – Rhine Graben case study, *Phys. Chem. Earth*, *28(9-11)*, 431–441, doi: 10.1016/S1474-7065(03)00063-9.

Bachu, S. (1988), Analysis of heat transfer processes and geothermal pattern in the Alberta Basin, Canada, *Journal of Geophysical Research*, *93*(B7), 7767–7781.

Bachu, S. (1999), Regional-scale geothermal and hydrodynamic regimes in the Alberta basin: a synthesis, in *Geothermics in Basin Analysis*, edited by A. Förster and D. Merriam, pp. 81–98, Kluwer, New York.

Bartier, P. M., and P. Keller (1996), Multivariate interpolation to incorporate thematic surface data using inverse distance weighting (idw), *Computers and Geosciences*, *22*(7), 795–799.

Bayer, U., M. Scheck, and M. Koehler (1997), Modeling of the 3D thermal field in the northeast German basin, *Geologische Rundschau*, *86*, 241–251, doi:10.1007/s005310050137.

Bayer, U., M. Scheck, W. Rabbel, C. M. Crawczyk, H.-J. Götze, M. Stiller, T. Beilecke, A.-M. Marotte, L. Barrio-Alvers, and J. Kuder (1999), An integrated study of the NE German basin, *Tectonophysics*, *313*, 145–169, doi:10.1016/S0040-1951(99)00249-8.

Bear, J., and Y. Bachmat (1991), Deletion of nondominant effects in modeling transport in porous media, in *Transport Phenomena in Porous Media, NATO Adv.St.Inst. Ser. E: Applied Science - No. 202*, edited by J. Bear and M. Y. Corapcioglu, pp. 3–62, Martinus Nijhoff, Dordrecht.

Beardsmore, G. R., and J. P. Cull (2001), *Crustal Heat Flow*, Cambridge University Press.

Bekele, E., M. Person, and B. Rostron (2000), Anomalous pressure generation within the Alberta Basin: Implications for oil charge to the Viking Formation, *Journal of Geochemical Exploration*, *69–70*, 601–605, doi:10.1016/S0375-6742(00)00064-9.

Bense, V. F., and H. Kooi (2004), Temporal and spatial variations of shallow subsurface temperature as a record of lateral variations in groundwater flow, *Journal of Geophysical Research*, *109, B04103*, doi:10.1029/2003JB002782.

Bense, V. F., and M. A. Person (2006), Faults as conduit-barrier systems to fluid flow in siliciclastic sedimentary aquifers, *Water Resources Research*, *42, W05421*, doi:10.1029/2005WR004480.

Bertleff, B., and R. Watzel (1998), Deep aquifer systems in the Southwest German Molasse Basin. An extensive hydrogeological analysis as the basis for future quantity and quality management, in *Proceedings of the International Symposium on mineral and thermal Groundwater, Miercurea Ciuc*, edited by I. Popa, pp. 11–19, Bucarest, Romania.

Bertleff, B., and R. Watzel (2002), Tiefe Aquifersystem im südwestdeutschen Molassebecken. Eine umfassende hydrogeologische Analyse als Grundlage eines zukünftigen Quantitäts- und Qualitätsmanagements, in *Abh. geol. Landesamt Baden-Württemberg*, vol. 15, pp. 75–90, Geol. Landesamt, Baden-Württemberg, Freiburg im Breisgau.

Bertleff, B., H. Joachim, G. Koziorowski, J. Leiber, W. Ohmert, R. Prestel, I. Stober, G. Strayle, E. Villinger, and J. Werner (1988), Ergebnisse der Hydrogeothermiebohrungen in Baden-Württemberg, in *Abh. geol. Landesamt Baden-Württemberg*, vol. 30, pp. 27–116, Geol. Landesamt, Baden-Württemberg, Freiberg im Breisgau.

Bertleff, B., D. Ellwanger, C. Szenkler, L. Eichinger, P. Trimborn, and N. Wolfendale (1993), Interpretation of hydrochemical and hydroisotopical measurements on paleaogroundwaters in Oberschwaben, south German alpine foreland, with focus on quaternary geology, in *Proceedings of an international symposium on applications of isotope techniques in studying past and current environmental changes in the hydrosphere and the atmosphere. Organized by the International Atomic Energy Agency, 19–23 April 1993*, vol. IAEA-SM-329/63, pp. 337–357, Vienna.

Bethke, C., X. Zhao, and T. Torgersen (1999), Groundwater flow and the ^4He distribution in the Great Artesian Basin of Australia, *Journal of Geophysical Research*, *104*(B6), 12,999–13,012, doi:10.1029/1999JB900085.

Bethke, C. M. (1986), Hydrologic constraints on the genesis of the upper Mississippi Valley mineral district from Illinois Basin brines, *Economic Geology*, *81*, 223–249.

Bethke, C. M. (1989), Modeling subsurface flow in sedimentary basins, *Geologische Rundschau*, *78*(1), 129–154.

Bourne, D. E., and P. C. Kendall (1973), *Vektoranalysis*, Teubner Studienbücher Physik.

Bowyer, A., and J. Woodwark (1983), *A programmers's geometry*, Butterworths, London England.

Bredehoeft, J. D., and I. S. Papadopulos (1965), Rates of vertical groundwater movement estimated from the earth's thermal profile, *Water Resources Research*, *1*(2), 325–328.

Cermák, V., and L. Rybach (1982), Thermal conductivity and and specific heat of minerals and rocks, in *Landolt-Börnstein: Numerical Data and Functional Relationships in Science and Technology*, vol. V/1a, edited by G. Angenheister, pp. 305–343, Springer, Berlin.

Clauser, C. (1999), *Thermal signatures of heat transfer processes in the Earth's crust*, 111 pp., Springer, Berlin–Heidelberg.

Clauser, C. (Ed.) (2003), *SHEMAT and Processing SHEMAT – Numerical Simulation of Reactive Flow in Hot Aquifers*, IX, 332 pp., Springer, Heidelberg–Berlin.

Clauser, C. (2006), Geothermal energy, in *K. Heinloth (ed), Landolt-Börnstein, Group VIII: Advanced Materials and Technologies, Vol. 3: Energy Technologies, Subvol. C: Renewable Energies*, pp. 493–604, Springer, Heidelberg-Berlin.

Clauser, C., and H. Villinger (1990), Analysis of conductive and convective heat transfer in a sedimentary basin, demonstrated for the Rheingraben, *Geophysical Journal International*, *100*(3), 393–414.

Cull, J. P., and D. Conley (1983), Geothermal gradients and heat flow in australian sedimentary basins, *Bureau of Mineral Resources, Journal of Australian Geology and Geophysics*, (8), 329–337.

Davis, S. H., S. Rosenblat, J. R. Wood, and T. A. Hewett (1985), Convective fluid flow and diagenetic patterns in domed sheets, *American Journal of Science*, *285*, 207–223.

Demirdžić, I. A. (1982), A finite volume method for computation of fluid flow in complex geometries, Ph.d. Thesis, University of London, Imperial College.

Deutsch, C. V., and A. G. Journel (1998), *GSLIB: Geostatistical Software Library and Users's Guide, 2nd Edition*, 369 pp., Oxford University Press, Oxford.

Diersch, H.-J. (1994), *Interactive, graphics-based finite-element simulation system – FEFLOW – for modelling groundwater flow and contaminant transport processes, Report*, WASY Gesellschaft für wasserwirtschaftliche Planung und Systemforschung mbH, Berlin.

Diersch, H.-J. (2005), *FEFLOW - Physical basis of modelling, Reference Manual*, WASY Gesellschaft für wasserwirtschaftliche Planung und Systemforschung mbH, Berlin.

Diersch, H. J.-G., and O. Kolditz (2002), Variable-density flow and transport in porous media: Approaches and challenges, *Advances in Water Resouces*, *25*, 899–944.

Domenico, P. A., and V. V. Palciauskas (1973), Theoretical analysis of forced convective heat transfer in regional ground-water flow, *Geological Society of America Bulletin*, *84*, 3803–3814.

Edwards, M. G. (2000), M-matrix flux splitting for general full tensor discretization operators on structured and unstructured grids, *J. Comput. Phys.*, *160*, 1–28, doi: 10.1006/jcph.2000.6418.

Eichhubl, P., and J. R. Boles (2000), Focused fluid flow along faults in the Monterey Formation, coastal California, *Geological Society of America Bulletin*, *112(11)*, 1667–1679, doi:10.1130/00110.1130/0016-7606(2000)112⟨1667:FFFAFI⟩2.0.CO;2.

Fairley, J. P., and J. J. Hinds (2004), Field observation of fluid circulation patterns in a normal fault system, *Geophysical Research Letters*, *31*, doi:10.1029/2004GL020812.

Fairley, J. P., J. Heffner, and J. J. Hinds (2003), Geostatistical evaluation of permeability in an active fault zone, *Geophysical Research Letters*, *30*(18), doi:10.1029/2003GL018064.

Ferziger, J. H., and M. Perić (2002), *Computational Methods for Fluid Dynamics. 3rd rev. ed.*, Springer, Berlin.

Fletcher, C. (2000a), *Computational Techniques for Fluid Dynamics: Volume 1: Fundamental and General Techniques, 2nd Edition – 4th Printing*, Springer, Berlin.

Fletcher, C. (2000b), *Computational Techniques for Fluid Dynamics: Volume 2: Specific Techniques for Different Flow Categories, 2nd Edition – 4th Printing*, Springer, Berlin.

Förster, A. (2001), Analysis of borehole temperature data in the Northeast German Basin: continuous logs versus bottom-hole temperatures, *Petroleum Geoscience*, *7*, 241–254.

Förster, A., and D. F. Merriam (1999a), *Problems and potential of industrial temperature data from a cratonic basin environment. In: Geothermics in Basin analysis*, pp. 35–60, Kluwer, New York.

Förster, A., and D. F. Merriam (Eds.) (1999b), *Geothermics in Basin analysis*, 1–241 pp., Kluwer, New York.

Förster, A., D. F. Merriam, and J. C. Davis (1997), Spatial analysis of temperature (BHT/DST) data and consequences for heat-flow determination in sedimentary basin, *Geologische Rundschau*, *86*(2), 252–261, doi:10.1007/s005310050138.

Freudenberger, W., and K. Schwerd (1996), Erläuterungen zur Geologischen Karte von Bayern 1 : 500 000, 4. neubearbeitete Auflage, *Tech. Rep.*, Bayerisches Geologisches Landesamt, München.

Frolkovic, P. (1996), Finite volume discretizations of density driven flows in porous media, in *Finite Volumes for Complex Applications*, edited by F. Benkhaldoun and R. Vilsmeier, pp. 433–440, Hermes, Paris.

Garven, G., S. Ge, M. A. Person, and D. A. Sverjensky (1993), Genesis of stratabound ore deposits in the midcontinent basins of North America: 1. the role of regional groundwater flow, *American Journal of Science*, *293*, 497–568.

George, P. (1996), Automatic mesh generation and finite element computation, in *Handbook of numerical analysis, Finite Element Methods (Part 2), Numerical Methods for Solids (Part 2)*, vol. IV., edited by P. Ciarlet and J. Lions, pp. 69–190, Elsevier Science B.V., Amsterdam, Lausanne, New York.

Gosnold, W. D. (1999), Basin-scale groundwater flow and advective heat flow: an example from the northern great plains, in *Geothermics in Basin analysis*, edited by A. Förster and D. F. Merriam, pp. 99–116, Kluwer, New York.

Haenel, R., L. Rybach, and L. Stegena (Eds.) (1988), *Handbook of terrestrial heat-flow density determination*, Kluwer, Dordrecht, Holland.

Häfner, F., D. Sames, and H. D. Voigt (1992), *Wärme- und Stofftransport, Mathematische Methoden*, Springer, Berlin–Heidelberg.

Hartmann, A., and V. Rath (2005), Uncertainties and shortcomings of ground surface temperature histories derived from inversion of temperature logs, *J. Geophysics and Engineering*, *2*, 299–311, doi:10.1088/1742-2132/2/4/S02.

Hartmann, A., V. Rath, and C. Clauser (2005), Thermal conductivity from core and well log data, *Int. J. Rock Mechanics and Mining Sciences*, *42*, 1042–1055, doi:10.1016/j.ijrmms.2005.05.015.

Huber, B. (1999), Das Thermalwasservorkommen im niederbayrisch-oberösterreichischen Molassebecken, *Report*, Bayrisches Landesamt für Wasserwirtschaft, München.

Huber, B. (2002), Das Grundwassermodell Malmkarst im niederbayerisch-oberöstereichischen Molassebecken, in *Leitfaden Hydrogeologische Modelle*, vol. 24, Fachsektion Hydrogeologie in der Deutschen Geologischen Gesellschaft (FH-DGG), Hannover.

Jacquotte, O.-P. (1998), Grid optimization methods for quality improvement and adaption, in *Handbook of Grid Generation*, edited by J. Thompson, B. Soni, and N. Weatherill, pp. 33–1–33–33, CRC Press, Boca Raton, Florida, USA.

Jin, X. (2001), Rechenverfahren zur Diskretisierung von Strömungen in komplexer Geometrie mittels körperangepaßter Gitter, Promotionsschrift, Fakultät für Maschinenbau, Universität Karlsruhe (TH).

Kiraly, L. (2002), Karstification and groundwater flow, in *Evolution of karst: from prekarst to cessation, Postojna-Ljubljana, Zalozba ZRC. Also available at: www.speleogenesis.net*, edited by F. Gabrovŝek, pp. 155–190.

Klingbeil, E. (1966), *Tensorrechnung für Ingenieure*, B-I-Hochschultaschenbücher 197/197a.

Kolditz, O., R. Ratke, H.-J. Diersch, and W. Zielke (1998), Coupled groundwater flow and transport: 1. Verification of variable density flow and transport models, *Advances in Water Resources*, *21*, 27–46, doi:10.1016/S0309-1708(96)00034-6.

Koschel, G. (1989), Abschlußbericht zum Forschungsvorhaben 03 E 6240 A/B, Hydrogeothermische Energiebilanz und Grundwasserhaushalt des Malmkarstes im süddeutschen Molassebecken, Schlussbericht, *Tech. Rep.*, Landesamt für Geologie Rohstoffe und Bergbau, Baden-Württemberg, Freiburg and Bayerisches Landesamt für Wasserwirtschaft, München, unpublished.

Kovács, A. (2003), Geometry and hydraulic parameters of karst aquifers: A hydrodynamic modeling approach., Ph.D. thesis, University of Neuchâtel, Switzerland.

Kukkonen, I. T., and C. Clauser (1994), Simulation of heat transfer at the Kola deep-hole site: implications for advection, heat refraction and paleoclimatic effects, *Geophysical Journal International*, *116*, 409–420, doi:10.1111/j.1365-246X.1994.tb01806.x.

Kutasov, I. M. (1999), *Applied Geothermics for Petroleum Engineers*, 347 pp pp., Elsevier, Amsterdam.

Lee, S., and B. K. Soni (1998), Governing equations of fluid mechanics in physical curvilinear coordinate system, *Electronic Journal of Differential Equations*, *Conference*(01), 149–157.

Lemcke, K. (1976), Übertiefe Grundwässer im süddeutschen Alpenvorland, *Bull. Ver. Schweizer Petrol.-Geol. u. Ing.*, *42*(103), 9–18.

Lemcke, K. (1984), Geologische Vorgänge in den Alpen ab Obereozän im Spiegel vor allem der deutschen Molasse, *Geologische Rundschau*, *73*(1), 371–397, doi:10.1007/BF01820376.

Lemcke, K., and W. Tunn (1956), Tiefenwasser in der süddeutschen Molasse und ihrer verkarsteten Malmunterlage, *Bull. Ver. Schweizer Petrol.-Geol. u. Ing.*, *23*(64), 35–56.

Leu, W., B. Keller, A. Matter, U. Schärli, and L. Rybach (1999), Geothermische Eigenschaften Schweizer Molassebecken (Tiefenbereich bis 500 m), enet-nr. 9723719, *Tech. Rep.*, Bundesamt für Energie, Bern.

López, D. L., and L. Smith (1995), Fluid flow in fault zones: Analysis of the interplay of convective circulation and topographically driven groundwater flow, *Water Resources Research*, *31*(6), 1489–1503.

López, D. L., and L. Smith (1996), Fluid flow in fault zones: Influence of hydraulic anisotropy and heterogeneity on the fluid flow and heat transfer regime, *Water Resources Research*, *32*(10), 3227–3235.

Loudyi, D., R. Falconer, and B. Lin (2007), Mathematical development and verification of a non-orthogonal finite volume model for groundwater flow applications, *Advances in Water Resources*, *30*(1), 29 – 42, doi:10.1016/j.advwatres.2006.02.010.

Lowell, R. P. (1975), Circulation in fractures, hot springs, and convective heat transport on mid-ocean ridge crests, *Geophysical Journal International*, *40*(3), 351–365, doi:10.1111/j.1365-246X.1975.tb04137.x.

Majorowicz, J. A., and A. M. Jessop (1981), Regional heat flow patterns in the western Canadian sedimentary basin, *Tectonophysics*, *74*(3–4), 209–238, doi:10.1016/0040-1951(81)90191-8.

Majorowicz, J. A., G. Garven, A. Jessop, and C. Jessop (1999), Present heat flow along a profile across the western Canada sedimetary basin, in *Geothermics in Basin analysis*, edited by A. Förster and D. Merriam, pp. 61–80, Kluwer, New York.

Mallet, J. (2002), *Geomodeling*, Oxford University Press, New York.

McConnell, A. J. (1957), *Applications of Tensor Analysis*, Dover Publications, Inc., New York.

Mölders, N., and W. Rühaak (2002), On the impact of explicitly predicted runoff on the simulated atmospheric response to small-scale land-use changes - an integrative modeling approach, *Atmospheric Research*, *63*(1-2), 3–38, doi:10.1016/S0169-8095(02)00002-9.

Murphy, H. D. (1979), Convective instabilities in vertical fractures and faults, *Journal of Geophysical Research*, *84*(B11), 6121–6130.

Narasimhan, T. N., and P. A. Witherspoon (1976), An integrated finite difference method for analyzing fluid flow in porous media, *Water Resources Research*, *12, 1*, 57–64.

Nunn, J., L. Guichang, and L. Zhang (1999), Thermal insulation by low thermal conductivity shales: implications for basin-scale fluid flow and heat transport, in *Geothermics in Basin analysis*, edited by A. Förster and D. Merriam, pp. 117–130, Kluwer, New York.

Ondrak, R., F. Wenderoth, M. Scheck, and U. Bayer (1998), Integrated geothermal modeling on different scales in the Northeast German Basin, *Geologische Rundschau*, *87*(1), 32–42, doi:10.1007/s005310050187.

Patankar, S. (1980), *Numerical Heat Transfer and Fluid Flow*, Hemisphere Publishing, New York, Philadelphia, London.

Patriarche, D., M. C. Castro, and P. Goovaerts (2005), Estimating regional hydraulic conductivity fields - a comparative study of geostatistical methods, *Mathematical Geology*, *37*(6), 587–613, doi:10.1007/s11004-005-7308-5.

Perić, M. (1985), A finite volume method for the prediction of three-dimensional fluid flow in complex ducts, Ph.D. Thesis, University of London, Imperial College.

Person, M., and G. Garven (1992), Hydrologic constraints on petroleum generation within continental rift basins: theory and application to the rhine graben, *AAPG Bulletin*, *76(4)*, 468–488.

Person, M., J. P. Raffensperger, S. Ge, and G. Garven (1996), Basin-scale hydrogeologic modeling, *Reviews of Geophysics*, *34*, 61–87.

Pestov, I. (2000), Thermal convection in the Great Artesian Basin, Australia, *Water Resources Management*, *14*(5), 391–403, doi:10.1023/A:1011103219851.

Phillips, O. M. (1991), *Flow and Reaction in Permeable Rocks*, Cambridge University Press.

Pitt, G. M. (1986), Geothermal gradients, geothermal histories and the timing of thermal naturation in the eromanga-cooper basins, in *Contributions to the Geology and Hydrocarbon Potential of the Eromanga Basin, Special Publication*, edited by D. Gravestock, P. Moore, and G. Pitt, 12, pp. 323–351, Geological Society of Australia, Sydney.

Polak, E. J., and C. L. Horsfall (1979), Geothermal gradients in the Great Artesian Basin, *Bulletin of the Australian Society of Exploration Geophysicists*, *10*(2), 144–148, doi: 10.1071/EG979144.

Powers, D. J., and K. O'Neill (1986), Natural convection in sloping porous layers, in *Finite Elements in Water Resources*, vol. Finite Elements in Water Resources: Proceedings of the VI International Conference on Finite Elements in Water Resources, Lisboa, Portugal, June 1986, edited by A. Sá da Costa, A. Melo Baptista, W. Gray, C. Brebbia, and G. Pinder, pp. 697–710, Springer, Heidelberg.

Pribnow, D., and R. Schellschmidt (2000), Thermal tracking of upper crustal fluid flow in the Rhine Graben, *Geophysical Research Letters*, *27*(13), 1957–1960.

Raffensperger, J. P., and D. Vlassopoulos (1999), The potential for free and mixed convection in sedimentary basins, *Hydrogeology Journal*, *7*(6), 506–520, doi:10.1007/s100400050224.

Rath, V., and C. Clauser (Eds.) (2005), *Erkennen und Quantifizieren von Strömung: Eine geothermische Rasteranalyse zur Klassifizierung des tiefen Untergrundes in Deutschland hinsichtlich seiner Eignung zur Endlagerung radioaktiver Stoffe - Fortsetzung, Endbericht zum Auftrag 9X0009-8497-2 des Bundesamtes für Strahlenschutz (BfS), 209 pp.*, Geophysica Beratungsgesellschaft mbH, Stolberg.

Rath, V., A. Wolf, and H. M. Bücker (2006), Joint three-dimensional inversion of coupled groundwater flow and heat transfer based on automatic differentiation: Sensitivity calculation, verification, and synthetic examples, *Geophys. J. Int.*, *167*(1), 453 – 466, doi:10.1111/j.1365-246X.2006.03074.x.

Reinecker, J., O. Heidbach, M. Tingay, B. Sperner, and B. Müller (2005), The release 2005 of the world stress map (www.world-stress-map.org), *Tech. Rep.*, Geophysical Institute, Karlsruhe University, Germany.

Rühaak, W. (2006), A Java application for quality weighted 3-d interpolation, *Computers and Geosciences*, *32*(1), 43–51, doi:10.1016/j.cageo.2005.04.005.

Rühaak, W., V. Rath, A. Wolf, and C. Clauser (2008), 3d-finite-volume groundwater and heat-transport modeling with non-orthogonal grids, using a coordinate transformation method, *Advances in Water Resources*, *31*(3), 513–524, doi:10.1016/j.advwatres.2007.11.002.

Saad, Y. (1996), *Iterative Methods for Sparse Linear Systems*, PWS, Boston.

Schmidt Mumm, A., and M. Wolfgramm (2004), Fluid systems and mineralization in the north German and Polish basin, *Geofluids*, *4*(4), 315–328, doi:10.1111/j.1468-8123.2004.00090.x.

Schönung, B. E. (1990), *Numerische Strömungsmechanik – Inkompressible Strömungen mit komplexen Berandungen*, Springer, Berlin.

Schulz, R., and M. Jobmann (1989), Hydrogeothermische Energiebilanz und Grundwasserhaushalt des Malmkarstes im Süddeutschen Molassebecken, *Abschlußbericht*, GGA Hannover.

Shepard, D. (1968), A two-dimensional interpolation function for irregularly spaced data, in *Proceedings 23rd National Conference Association for Computing Machinery (ACM)*, pp. 517–523, New York.

Signorelli, S., S. Bassetti, D. Pahud, and T. Kohl (2007), Numerical evaluation of thermal response tests, *Geothermics*, *36*(2), 141–166, doi:10.1016/j.geothermics.2006.10.006.

Simms, M. A., and G. Garven (2004), Thermal convection in faulted extensional sedimentary basins: theoretical results from finite-element modeling, *Geofluids*, *4*(2), 109–130, doi:10.1111/j.1468-8115.2004.00069.x.

Simpson, M., and T. Clement (2003), Comparison of finite difference and finite element solutions to the variably saturated flow equation, *Journal of Hydrology*, *270*(1-2), 49–64, doi:10.1016/S0022-1694(02)00294-9.

Smith, L., C. Forster, and J. Evans (1990), Interaction of fault zones, fluid flow, and heat transfer at the basin scale, in hydrogeology of low permeability environments, in *Special Symposium at the 28th International Geological Congress, Washington, D.C., U.S.A., July 9-19, 1989, Hydrogeology*, vol. 2, edited by S. P. Neuman and I. Neretnieks, pp. 41–67, Verlag Heinz Heise, Hanover, Germany.

Snow, D. (1965), A parallel plate model of fractured permeable media, Ph.D. thesis, University of California, Berkeley, USA.

Stallman, R. W. (1963), Computation of ground-water velocity from temperature data, *USGS Water Supply Papers, Washington, DC, USA*, *1544-H*, 36–46.

Stange, S., and W. Brüstle (2003), Die Erdbebenserie von Bad Saulgau, 2001, in *Jahresberichte und Mitteilungen des Oberrheinischen Geologischen Vereins, N.F.*, vol. 85, pp. 441–460, Schweizerbart, Stuttgart.

Tarantola, A., and B. Valette (1982), Inverse problems = quest for information, *Journal of Geophysics*, *50*, 159–170.

Thompson, J., and N. Weatherill (1998), Fundamental concepts and approaches, in *Handbook of Grid Generation*, edited by J. Thompson, B. Soni, and N. Weatherill, pp. 1–11–1–30, CRC Press, Boca Raton, Florida, USA.

Thompson, J., Z. Warsi, and C. Mastin (1985), *Numerical Grid Generation*, North-Holland, New York.

Thorenz, C. (2001), Model adaptive simulation of multiphase and density driven flow in fractured and porous media, Dissertation, Institut für Strömungsmechanik und elektron. Rechnen im Bauwesen, University Hannover.

Tomczak, M. (1998), Spatial interpolation and its uncertainty using automated anisotropic inverse distance weighting (idw) - cross-validation/jackknife approach, *Journal of Geographic Information and Decision Analysis*, *2*(2), 18–33.

Tóth, J. (1962), A theory of groundwater motion in small drainage basins in central Alberta, *Journal of Geophysical Research*, *68*, 4795–4812.

Vasseur, G., F. Brigaud, and L. Demongodin (1995), Thermal conductivity estimation in sedimentary basins, *Tectonophysics*, *244*(1-3), 167–174, doi:10.1016/0040-1951(94)00225-X.

Vinokur, M. (1989), An analysis of finite-difference and finite-volume formulations of conservation laws, *Journal of Computational Physics*, *81*(1), 1–52, doi:10.1016/0021-9991(89)90063-6.

Vollmayr, T. (1985), Temperature in the subsurface of the Swiss and German alpine foreland, *Journal of Geodynamics*, *4*, 305–319.

Voss, C., and W. Souza (1987), Variable density flow and solute transport simulation of regional aguifers containing a narrow freshwater saltwater transition zone, *Water Resources Research*, *23*(10), 1851–1866.

Vosteen, H.-D., V. Rath, A. Schmidt-Mumm, and C. Clauser (2004), The thermal regime of the Northeastern-German Basin from 2-D inversion, *Tectonophysics*, *386*(1–2), 81–95, doi:10.1016/j.tecto.2004.05.004.

Wagner, W., and U. Overhoff (2006), *Extended IAPWS-IF97 Steam Tables.*, Springer, Berlin.

Wagner, W., and A. Pruß (2002), The IAPWS formulation 1995 for the thermodynamic properties of ordinary water substance for general and scientific use, *Journal of Physical and Chemical Reference Data*, *31*, 387 – 535, doi:10.1063/1.1461829.

Waples, D. W., and M. Ramly (2001), A statistical method for correcting log-derived temperatures, *Petroleum Geoscience*, *7*, 231–240.

Ware, C., W. Knight, and D. Wells (1991), Memory intensive algorithms for multibeam bathymetry data, *Computers and Geosciences*, *17*(7), 985–993, doi:10.1016/0098-3004(91)90093-S.

Wesseling, P. (2001), *Principles of computational fluid dynamics*, Springer, Berlin.

Yang, J., R. R. Large, and S. W. Bull (2004), Factors controlling free thermal convection in faults in sedimentary basins: implications for the formation of zinc-lead mineral deposits, *Geofluids*, *4*(3), 237–247, doi:10.1111/j.1468-8123.2004.00084.x.

Yeh, G.-T. (1999), *Computational Subsurface Hydrology: Fluid Flows*, Kluwer, Boston.

Zoth, T. A., and R. Hänel (1988), Appendix, in *Handbook of Terrestrial Heat Flow Determinations*, edited by R. Hänel, L. Rybach, and L. Stegena, pp. 449–466, Kluwer.

Zschocke, A. (2005), Correction of non-equilibrated temperature logs and implications for geothermal investigations, *J. Geophysics and Engineering*, *2*, 364–371, doi:10.1088/1742-2132/2/4/S10.

Zschocke, A., V. Rath, C. Grissemann, and C. Clauser (2005), Estimating darcy flow velocities from correlated anomalies in temperature logs, *J. Geophysics and Engineering*, *2*, 332–342, doi:10.1088/1742-2132/2/4/S06.

Zweigel, J. (1998), *Eustatic versus tectonic control on foreland basin fill. Sequence stratigraphy, subsidence analysis, stratigraphic modelling, and reservoir modelling applied to the German Molasse basin*, 140 pp., Schweizerbart, Stuttgart.

A Appendix

A.1 Coordinate transformation

The following introduction into the tensor calculus is based on the thesis of *Perić* (1985) and *Jin* (2001). However, the theory is well known and has been introduced in different textbooks before, e.g. *McConnell* (1957), *Klingbeil* (1966), and *Bourne and Kendall* (1973).

Fig. 31 shows a general, non-orthogonal coordinate system (x_1, x_2, x_3) and the reference cartesian coordinate system (y_1, y_1, y_3). $\mathbf{i_i}$ with $i = 1, 2, 3$ denoting the unit vectors of the cartesian coordinate system.

$\mathbf{e}_i$ corresponds to the covariant base vector in the general coordinate system which is tangential to its coordinate line x_i.

The term covariant is related to a transformation that describes new basis vectors in terms of an old basis. Indices identifying these basis vectors are placed as lower indices.

$$\mathbf{e}_i = \sum_{j=1}^{3} \frac{\partial y_j}{\partial x_i} \mathbf{i}_j \tag{46}$$

The contravariant base vector $\mathbf{e^i}$ (inverse to the covariant one and with upper indices) is normal to the coordinate surface of constant x_i, and is defined as:

$$\mathbf{e}^i = \sum_{j=1}^{3} \frac{\partial x_i}{\partial y_j} \mathbf{i}^j \tag{47}$$

In cartesian coordinates is $\mathbf{e}_i = \mathbf{e}^i(\mathbf{i}_m = \mathbf{i}^m)$, therefore, no difference is made between covariant and contravariant values.

From Eq. 46 and 47 yields the following relation between $\mathbf{e}_i$ and $\mathbf{e}^j$:

$$\begin{aligned} \mathbf{e}_i \cdot \mathbf{e}^j \quad &= \quad \delta_i^j \\ \delta_i^j = 1 \quad &, \quad i = j \\ \delta_i^j = 0 \quad &, \quad i \neq j \end{aligned} \tag{48}$$

Here δ denotes the Kronecker delta.

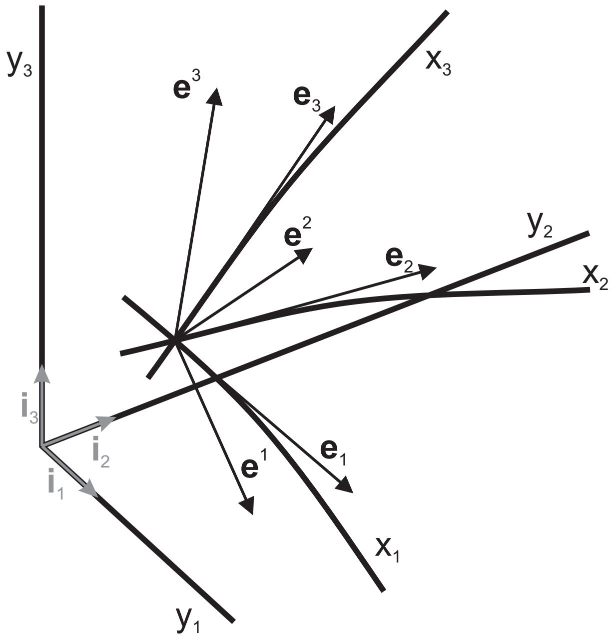

Figure 31: General coordinate system (x_1, x_2, x_3), reference cartesian frame (y_1, y_2, y_3), their base vectors $\mathbf{e}_i$, $\mathbf{e}^i$, and cartesian unit vectors $\mathbf{i}_i$, respectively (modified from *Perić*, 1985; *Jin*, 2001).

The curvilinear coordinates x_i can be stated as function of the cartesian coordinates y_j:

$$\begin{bmatrix} x_1 \\ x_2 \\ x_3 \end{bmatrix} = \begin{bmatrix} x_1(y_1, y_2, y_3) \\ x_2(y_1, y_2, y_3) \\ x_3(y_1, y_2, y_3) \end{bmatrix} \tag{49}$$

The Jacobi matrix for this transformation has been defined in Eq. 9. To guarantee that the transformation is not singular the determinant of the Jacobian (Eq.10) should be neither 0 nor ∞.

The reciprocal transformation of Eq. 49 yields:

$$\begin{bmatrix} y_1 \\ y_2 \\ y_3 \end{bmatrix} = \begin{bmatrix} y_1(x_1, x_2, x_3) \\ y_2(x_1, x_2, x_3) \\ y_3(x_1, x_2, x_3) \end{bmatrix} \tag{50}$$

which gives the following transformed Jacobian:

$$\bar{\mathbf{J}} = \begin{bmatrix} \frac{\partial y_1}{\partial x_1} & \frac{\partial y_1}{\partial x_2} & \frac{\partial y_1}{\partial x_3} \\ \frac{\partial y_2}{\partial x_1} & \frac{\partial y_2}{\partial x_2} & \frac{\partial y_2}{\partial x_3} \\ \frac{\partial y_3}{\partial x_1} & \frac{\partial y_3}{\partial x_2} & \frac{\partial y_3}{\partial x_3} \end{bmatrix}. \tag{51}$$

Here the determinant

$$\bar{J} = \begin{vmatrix} \frac{\partial y_1}{\partial x_1} & \frac{\partial y_1}{\partial x_2} & \frac{\partial y_1}{\partial x_3} \\ \frac{\partial y_2}{\partial x_1} & \frac{\partial y_2}{\partial x_2} & \frac{\partial y_2}{\partial x_3} \\ \frac{\partial y_3}{\partial x_1} & \frac{\partial y_3}{\partial x_2} & \frac{\partial y_3}{\partial x_3} \end{vmatrix}. \tag{52}$$

again must not be either 0 nor ∞.

The relation between both Jacobian is:

$$\mathbf{J} = \bar{\mathbf{J}}^{-1}. \tag{53}$$

An arbitrary cartesian vector $\mathbf{v} = v_m \mathbf{i}_m$ can be decomposed into its covariant and contravariant base vectors:

$$\mathbf{v} = v^i \mathbf{e}_i = v_i \mathbf{e}^i, \tag{54}$$

where v^i and v_i are the contravariant and covariant components of $\mathbf{v}$, respectively.

The scalar product of two vectors can be stated as:

$$\mathbf{v} \cdot \mathbf{v} = g_{ij} v^i v^j = g^{ij} v_i v_j \tag{55}$$

with

$$g_{ij} = \mathbf{e}_i \cdot \mathbf{e}_j, g^{ij} = \mathbf{e}^i \cdot \mathbf{e}^j. \tag{56}$$

The symmetric matrices $\mathbf{g} = \{\mathbf{g}_{ij}\}$ and $\bar{\mathbf{g}} = \{\mathbf{g}^{ij}\}$ are the magnitude and reciprocal magnitudes of the base tensor, respectively.

A more comprehensive explanation about the properties of tensors and detailed conversions are given for instance in *Demirdžić* (1982) and *Thompson and Weatherill* (1998).

A.2 Numerical procedure

The complete definition of Eq. 22 is:

$$
\begin{array}{llll}
\text{East:} & (\Delta y_1)_1 = y_1^E - y_1^P & \text{West:} & (\Delta y_1)_1 = y_1^P - y_1^W \\
 & (\Delta y_1)_2 = y_1^{ne} - y_1^{se} & & (\Delta y_1)_2 = y_1^{nw} - y_1^{sw} \\
 & (\Delta y_1)_3 = y_1^{te} - y_1^{be} & & (\Delta y_1)_3 = y_1^{tw} - y_1^{bw} \\
 & (\Delta y_2)_1 = y_2^E - y_2^P & & (\Delta y_2)_1 = y_2^P - y_2^W \\
 & (\Delta y_2)_2 = y_2^{ne} - y_2^{se} & & (\Delta y_2)_2 = y_2^{nw} - y_2^{sw} \\
 & (\Delta y_2)_3 = y_2^{te} - y_2^{be} & & (\Delta y_2)_3 = y_2^{tw} - y_2^{bw} \\
 & (\Delta y_3)_1 = y_3^E - y_3^P & & (\Delta y_3)_1 = y_3^P - y_3^W \\
 & (\Delta y_3)_2 = y_3^{ne} - y_3^{se} & & (\Delta y_3)_2 = y_3^{nw} - y_3^{sw} \\
 & (\Delta y_3)_3 = y_3^{te} - y_3^{be} & & (\Delta y_3)_3 = y_3^{tw} - y_3^{bw} \\
\text{North:} & (\Delta y_1)_1 = y_1^{ne} - y_1^{nw} & \text{South:} & (\Delta y_1)_1 = y_1^{se} - y_1^{sw} \\
 & (\Delta y_1)_2 = y_1^N - y_1^P & & (\Delta y_1)_2 = y_1^P - y_1^S \\
 & (\Delta y_1)_3 = y_1^{tn} - y_1^{bn} & & (\Delta y_1)_3 = y_1^{ts} - y_1^{bs} \\
 & (\Delta y_2)_1 = y_2^{ne} - y_2^{nw} & & (\Delta y_2)_1 = y_2^{se} - y_2^{sw} \\
 & (\Delta y_2)_2 = y_2^N - y_2^P & & (\Delta y_2)_2 = y_2^P - y_2^S \\
 & (\Delta y_2)_3 = y_2^{tn} - y_2^{bn} & & (\Delta y_2)_3 = y_2^{ts} - y_2^{bs} \\
 & (\Delta y_3)_1 = y_3^{ne} - y_3^{nw} & & (\Delta y_3)_1 = y_3^{se} - y_3^{sw} \\
 & (\Delta y_3)_2 = y_3^N - y_3^P & & (\Delta y_3)_2 = y_3^P - y_3^S \\
 & (\Delta y_3)_3 = y_3^{tn} - y_3^{bn} & & (\Delta y_3)_3 = y_3^{ts} - y_3^{bs} \\
\text{Top:} & (\Delta y_1)_1 = y_1^{te} - y_1^{tw} & \text{Buttom:} & (\Delta y_1)_1 = y_1^{be} - y_1^{bw} \\
 & (\Delta y_1)_2 = y_1^{tn} - y_1^{ts} & & (\Delta y_1)_2 = y_1^{bn} - y_1^{bs} \\
 & (\Delta y_1)_3 = y_1^T - y_1^P & & (\Delta y_1)_3 = y_1^P - y_1^B \\
 & (\Delta y_2)_1 = y_2^{te} - y_2^{tw} & & (\Delta y_2)_1 = y_2^{be} - y_2^{bw} \\
 & (\Delta y_2)_2 = y_2^{tn} - y_2^{ts} & & (\Delta y_2)_2 = y_2^{bn} - y_2^{bs} \\
 & (\Delta y_2)_3 = y_2^T - y_2^P & & (\Delta y_2)_3 = y_2^P - y_2^B \\
 & (\Delta y_3)_1 = y_3^{te} - y_3^{tw} & & (\Delta y_3)_1 = y_3^{be} - y_3^{bw} \\
 & (\Delta y_3)_2 = y_3^{tn} - y_3^{ts} & & (\Delta y_3)_2 = y_3^{bn} - y_3^{bs} \\
 & (\Delta y_3)_3 = y_3^T - y_3^P & & (\Delta y_3)_3 = y_3^P - y_3^B
\end{array}
$$

Within the cartesian system always lower values are subtracted from higher ones ($E-P$, $N-P$, $T-P$ but $P-W$, $P-S$, $P-B$). Due to the non-orthogonality it is none the less possible that negative values for Δy occur.

If the diffusion term is discretized locally with a central differencing scheme (see Eq. 19), inner derivatives occur for this second derivative. For the scalar value h these three curvilinear derivatives coordinate directions are approximated by:

$$\left(\frac{\partial h}{\partial x_1}\right)^e \approx \frac{h_E - h_P}{\delta x_1^e}, \left(\frac{\partial h}{\partial x_2}\right)^e \approx \frac{h_{ne} - h_{se}}{\delta x_2^e}, \left(\frac{\partial h}{\partial x_3}\right)^e \approx \frac{h_{te} - h_{be}}{\delta x_3^e}. \tag{57}$$

Values with the subscript P denote values of the central control volume, whereas e.g. the subscript e denotes values of an volume which is shifted for half of the mesh size at the surface e in the coordinate direction x_j. For the normal derivative at the surface e with respect to x_1 a linear connection is assumed. For the cross derivatives on the surface x_2 and x_3 values like h_{ne} occur, which have to be calculated using a linear interpolation of the neighboring mesh nodes (see section 2.2.2).

Finally, the complete formulation for the geometric coefficients D_k^j calculated based on b_j^i is:

$$\begin{aligned}
D_1^1 &= b_1^1 b_1^1 + b_2^1 b_2^1 + b_3^1 b_3^1 \\
D_1^2 &= b_1^2 b_1^1 + b_2^2 b_2^1 + b_3^2 b_3^1 \\
D_1^3 &= b_1^3 b_1^1 + b_2^3 b_2^1 + b_3^3 b_3^1 \\
D_2^1 &= D_1^2 \\
D_2^2 &= b_1^2 b_1^2 + b_2^2 b_2^2 + b_3^2 b_3^2 \\
D_2^3 &= b_1^3 b_1^2 + b_2^3 b_2^2 + b_3^3 b_3^2 \\
D_3^1 &= D_1^3 \\
D_3^2 &= D_2^3 \\
D_3^3 &= b_1^3 b_1^3 + b_2^3 b_2^3 + b_3^3 b_3^3
\end{aligned} \tag{58}$$

Curriculum Vitae

Persönliche Angaben

Name	Wolfram Rühaak
Geburtsdatum	28.06.1967
Geburtsort	Berleburg

Wissenschaftlicher Werdegang

Abitur am Ulrichsgymnasium Norden/Ostfriesland am 26.05.1987.

Abschluss als Diplom-Geologe an der Technischen Universität Braunschweig am 14.07.1999.

Vom 01.10.1999 bis 31.10.2000: Wissenschaftlicher Mitarbeiter am Institut für Meteorologie der Universität Leipzig.
Aufgabe: hydrometeorologische Modellentwicklung.

Vom 01.11.2000 bis 31.10.2004: Wissenschaftlicher Angestellter am GGA-Institut, Sektion Geothermik und Grundwasserhydraulik.
Projekt: 'Geothermische Rasteranalyse'.

Vom 20.07.2005 bis 14.06.2007: Wissenschaftlicher Angestellter am GGA-Institut, Sektion Informationssysteme und Geomodelle.
Aufgabe: Geomodellierung.

Seit dem 01.09.2007: Wissenschaftlicher Mitarbeiter im Groundwater Modelling Centre der DHI-WASY GmbH in Berlin.

Berlin, 22. Februar 2009